

Non-ergodic delocalized states for efficient population transfer within a narrow band of the energy landscape

Vadim N. Smelyanskiy,¹ Kostyantyn Kechedzhi,^{2,3} Sergio Boixo,¹

Sergei V. Isakov,⁴ Hartmut Neven,¹ and Boris Altshuler⁵

¹*Google, Venice, CA 90291, USA*

²*QuAIL, NASA Ames Research Center, Moffett Field, California 94035, USA*

³*University Space Research Association, 615 National Ave, Mountain View, CA 94043*

⁴*Google, 8002 Zurich, Switzerland*

⁵*Physics Department, Columbia University, 538 West 120th Street, New York, New York 10027, USA*

(Dated: February 19, 2023)

Quantum tunneling has been proposed as an efficient mechanism of quantum search and optimization. However, classical simulations using Quantum Monte Carlo (QMC) can efficiently simulate tunneling transitions away from local minima if the tunneling is dominated by a single path. We analyze the computational role of coherent multi-qubit tunneling that gives rise to bands of delocalized quantum states providing a coherent pathway for population transfer (PT) between computational states with similar energies. In this regime, PT cannot be efficiently simulated by QMC. Given an energy function $\mathcal{E}(z)$ of a binary optimization problem and an initial bit-string z_i with atypically low energy, our goal is to find other bit-strings at energies within the narrow window $\Delta\mathcal{E}_{\text{cl}}$ around $\mathcal{E}(z_i)$. We study PT resulting from quantum evolution under a constant transverse field B_{\perp} of an n -spin system that encodes $\mathcal{E}(z)$. We focus on a simple yet nontrivial model: M randomly chosen "marked" bit-strings ($2^n \gg M$) are assigned energies $\mathcal{E}(z) \in [-n - W/2, n + W/2]$, while the rest of the states are assigned energy 0. The PT starts at a marked state and ends up in a superposition of $\sim \Omega$ marked states inside the window $\Delta\mathcal{E}_{\text{cl}}$. The best known classical algorithm for finding another marked state has a runtime $O(2^n/\Omega)$. We find that the scaling of a typical PT runtime with n and Ω is the same as that in the multi-target Grover's quantum search algorithm, except for a factor that is equal to $\exp(nB_{\perp}^{-2}/2)$ for $n \gg B_{\perp}^2 \gg 1$. Unlike the Hamiltonians used in analog quantum unstructured search algorithms known so far, the model we consider is non-integrable and the transverse field delocalizes the marked states. As a result, our PT protocol is not exponentially sensitive in n to the weight of the driver Hamiltonian and may be initialized with a computational basis state. We develop the microscopic theory of PT by constructing an $M \times M$ down-folded dense Hamiltonian \mathcal{H} acting in the space of marked states. It belongs to the class of preferred basis Levy matrices (PBLM) with the dispersion of the diagonal elements determined by W and a heavy tailed distribution of off-diagonal matrix elements. Under certain conditions, the band of the marked states splits into minibands of non-ergodic delocalized states whose width obeys a heavy-tailed distribution directly related to that of PT runtimes. We obtain an explicit form of this distribution by finding an analytical solution of nonlinear cavity equations for the random matrix ensemble of down-folded Hamiltonians \mathcal{H} . It corresponds to an alpha-stable Levy law with tail index 1. We argue that our approach can be applied to study the PT protocol in other transverse field spin glass models, with a potential quantum advantage over classical algorithms.

CONTENTS

		results	19
I. Introduction and Summary of Results	2	VIII. Solution of cavity equations in non-ergodic delocalized phase	20
II. Downfolding into the subspace of the marked states and nonlinear eigenproblem	5	IX. Complexity of the Population Transfer protocol	23
III. Coupling coefficients in the downfolded Hamiltonian	6	X. Comparison with the analogue Grover search	24
IV. Downfolded Hamiltonian near the center of the Impurity Band	9	XI. Numerical Simulations	27
V. Statistical ensemble of the Impurity Band Hamiltonians	12	XII. Outlook	30
VI. Born approximation for the transition rates	15	XIII. Conclusion	32
VII. Cavity method: summary of the previous		Acknowledgments	33
		References	33

A. Matrix elements of the downfolded Hamiltonian and the normalization condition for its eigenvectors	35
B. Details of the WKB analysis of the coupling coefficients	36
C. Linearization of the down-folded Hamiltonian near the center of the Impurity Band	38
D. PDF of the squared off-diagonal matrix elements of impurity band Hamiltonian	40
E. Characteristic function of the PDF of the squared off-diagonal matrix elements of impurity band Hamiltonian	42
F. Generalized Central Limit Theorem for the sum of M random variables w_m that obey the distribution $g_\infty(w)$	43
G. Justification of replacing sum with integral in Eq.(82).	44
H. PDF of the random variable $h = \frac{\eta}{(z-\epsilon)^2 + \eta^2}$	44
I. PDF of the imaginary part of self-energy in self-consistent Born approximation	45
J. Numerical simulations	48

I. INTRODUCTION AND SUMMARY OF RESULTS

The idea to use quantum computers for the solution of search and discrete optimization problems has been actively pursued for decades, mostly notably in connection to Grover's algorithm [1], quantum annealing idea to use quantum computers for the solution of search and discrete optimization problems has been actively pursued for decades, most notably in connection to Grover's algorithm [1], quantum annealing [2–10], and more recently, quantum approximate optimization [11]. Quantum tunneling of collective spin excitations was proposed and studied experimentally as a mechanism for moving between states in the energy landscape that can lead to shorter transition time scales compared to classical Simulated Annealing approaches under certain conditions [4]. Experimental evidence of the faster time scales was later corroborated numerically using an imaginary-time Quantum Monte Carlo (QMC) algorithm [12]. However, in Ref. [13] it was demonstrated that the quantum advantage found in [12] was due to the discretization in the QMC implementation rather than being a genuine quantum effect. Furthermore, recent studies [14, 15] have shown that in QMC, the tunneling corresponds to the Kramers escape through the free-energy barrier in an extended spin system that includes spin replicas in an

imaginary time direction. As a result, the incoherent quantum tunneling rate does not have a scaling advantage over such a QMC simulation.

Previous studies focused on the case where the quantum dynamics corresponded to sequential incoherent quantum tunneling processes connecting individual minima, where each step is dominated by a single tunneling path. In this paper we focus on understanding the computational role of coherent multiqubit tunneling in situations where large number of tunneling paths can interfere constructively, giving rise to the onset of many-body delocalization in Fock space.

In a binary optimization problem, the goal is to find the minimum of a classical energy function, $\mathcal{E}(z)$, defined over the set of 2^n configurations of n bits (bit-strings) $z = (z^1, z^2, \dots, z^n)$ where $z^k = \{0, 1\}$. In quantum algorithms $\mathcal{E}(z)$ is typically encoded in an n -qubit Hamiltonian

$$H_{cl} = \sum_z \mathcal{E}(z) |z\rangle\langle z| \quad (1)$$

diagonal in the basis of states $|z\rangle$ called the computational basis.

Hard optimization problems have their counterparts in spin glass models of statistical physics [16, 17]. The energy function of a hard optimization problem is characterized by a large number of spurious local minima. Low-energy minima can be separated by a large Hamming distance (number of bit flips transforming one to another). Such landscape gives rise to an interesting computational primitive: given an initial bit-string z_j with atypically low energy, we wish to produce other bit-strings with energies in a narrow range $\Delta\mathcal{E}_{cl}$ around the initial one. In general, this can be a difficult search problem if the number of bit-strings of interest is exponentially small compared to 2^n .

Inspired by the Hamiltonian-based approaches to quantum search [18] and optimization [2–4] we propose the following quantum population transfer (PT) protocol: first preparing the system in a computational state $|z_j\rangle$ with classical energy $\mathcal{E}(z_j)$, we then evolve it under the Hamiltonian

$$H = H_{cl} + H_D, \quad H_D = -B_\perp \sum_{k=0}^n \sigma_x^k, \quad (2)$$

without fine-tuning the evolution time nor the strength of the time-independent transverse field B_\perp . At the final moment we projectively measure in the computational basis and check if the outcome z is a “solution”, i.e., $z \neq z_j$ and the energy $\mathcal{E}(z)$ is inside the window $\Delta\mathcal{E}_{cl}$. The second term in the Hamiltonian (2) proportional to B_\perp is responsible for the PT. It is usually referred to as a “driver Hamiltonian” in the Quantum Annealing literature [3].

We note that the output of PT z can be used as an input of a classical optimization heuristic such as simulated annealing or parallel tempering in a “hybrid” optimiza-

tion algorithm [19] where quantum and classical steps can be used sequentially to gain the complementary advantages of both [20].

For random optimization problems diagonal matrix elements $\mathcal{E}(z)$ of the Hamiltonian (1) correspond to a problem instance sampled from a particular statistical ensemble. Since off-diagonal matrix elements ($-B_\perp$) connect states separated by one bit-flip, Eq. (2) describes the Hamiltonian of the tight-binding model with diagonal disorder on the Boolean hypercube [21]. It is a generalization of the Anderson model initially introduced in the context of transport in finite dimensional lattices [22]. In this model (2), as well as in the original Anderson model, there exist bands of localized and extended states separated in energy by a so-called “mobility edge”. Originally, extensions of Anderson model appeared in a variety of many-body problems in condensed matter physics [23, 24] giving rise to the concept of many-body localization (MBL). It was demonstrated in Ref. [21] that MBL is responsible for the failure of Quantum Annealing to find a solution of the constraint satisfaction problem (although, the detailed analysis of this effect is still needed [7, 25]). In some models of quantum spin glasses the existence of the two types of eigenstates and the mobility edge were studied in Refs. [5, 26, 27].

For spin glass models (2) with B_\perp below the quantum spin glass transition, the probability density function (PDF) of the eigenvalues E_β of H is localized around the mean classical energy, with an exponentially decaying tail reaching towards the low energy states. We choose the interval of energies $\Delta\mathcal{E}_{cl}$ to be at the tail of the distribution, of E_β but sufficiently far from the ground state so that the typical spacing of eigenvalues is exponentially small in n . Under these conditions classical states inside the energy window $\Delta\mathcal{E}_{cl}$ are located near deep local minima of the classical energy landscape $\mathcal{E}(z)$. Hamming distances between the minima scale with n and the number of them is exponentially small compared to 2^n yet still exponentially large in n .

In this paper we apply the PT protocol with Hamiltonian (2) to a simple yet nontrivial model of $\mathcal{E}(z)$ with the properties mentioned above

$$H_{cl} = \sum_{j=1}^M \mathcal{E}(z_j) |z_j\rangle \langle z_j|. \quad (3)$$

Here $M \gg 1$ marked states $|z_j\rangle$ (n -bit-strings z_j) are chosen uniformly at random from all bit-strings of length n , with energies $\mathcal{E}(z_j)$ independently distributed around $-n$ within a narrow band of width $W \ll B_\perp$. All other states z have energies $\mathcal{E}(z) = 0$ and are separated by a large gap $\simeq n$ from the very narrow band of marked states (see Fig. 1). This model is inspired by the impurity band model in doped semiconductors [28]. It also corresponds to a classical unstructured search problem with multiple marked states.

We obtain an explicit analytical form for the statistical properties of the PT dynamics in the above model by deriving an effective down-folded Hamiltonian in the

energy strip associated with the PT and using the cavity method for random matrices [29–34].

In model (3), the most efficient classical algorithm is purely random search with running time $\sim 2^n$. We find that the typical runtime of the PT algorithm t_{PT} displays the following scaling dependence on n

$$t_{PT} \propto \left(\frac{2^n}{\Omega \log \Omega} \right)^{1/2} e^{n/(2B_\perp)}. \quad (4)$$

Here $\Omega \gg 1$ is the number of computational basis states within the target window of energies that contribute with comparable probabilities to the quantum state at the end of PT. The expression applies in the range of transverse fields $n^{1/2} \gg B_\perp - 1 = \mathcal{O}(1)$ (for arbitrary B_\perp see Eq. (31)).

The dependence of t_{PT} on Ω is the same as in the multi-target Grover quantum algorithm that searches for Ω marked states starting from the fully-symmetric state $|S\rangle = 2^{-n/2} \sum_z |z\rangle$. In the Hamiltonian version of this algorithm [18], one uses the projector to $|S\rangle$ as a driver, $H_D = w |S\rangle \langle S|$. This algorithm is proven to be optimal for problems without structure. We emphasize that according to Eq. (4) the exponential scaling of t_{PT} with n differs from that in the Grover algorithm by a term $\sim B_\perp^{-2}$ that can be made arbitrary small at sufficiently large transverse fields.

At the same time the PT algorithm has new and potentially advantageous features compared to the Grover algorithm. The PT Hamiltonian H (2) is non-integrable and its eigenstates are delocalized in the marked state subspace. In contrast, the Grover Hamiltonian is integrable and all of its eigenstates but one are localized. Therefore the quantum evolution resulting from the Grover Hamiltonian cannot form a massive superposition of $\Omega \gg 1$ solutions if it starts from a computational basis state. The algorithm must always start from the state $|S\rangle$. Moreover, Grover’s algorithm performance is exponentially sensitive to fine-tuning of the weight of the driver w on the scale $\delta w \sim 2^{-n/2} \sqrt{\Omega}$. In contrast, the scaling of the runtime of PT (4) with n is robust to the choice of B_\perp that can take on a broad range of values for $B_\perp \gg 1$.

For a randomly chosen marked state the average Hamming distance to another marked state is $n/2$. If M is exponentially large in n the typical distance d_{\min} to the nearest marked state is much smaller than $n/2$ but remains extensive $d_{\min} = \mathcal{O}(n)$. As such, each marked state $|z_j\rangle$ is a deep local minimum of $\mathcal{E}(z)$. The transverse field B_\perp gives rise to multiqubit tunneling between the states. The tunneling amplitudes from a given minimum to its neighbors located at a Hamming distance d decrease exponentially with d while the number of neighbors increases exponentially with d for $d = \mathcal{O}(n)$. As a result, an eigenstate $|\psi_\beta\rangle$ of H associated with the impurity band can become delocalized over a large subset of marked states \mathcal{S}_β with size $1 \ll |\mathcal{S}_\beta| \propto M^\alpha$ and $0 < \alpha \leq 1$. For $\alpha = 0$ the eigenstate $|\psi_\beta\rangle$ is localized, for

$\alpha = 1$ the eigenstate is delocalized in the entire space of marked states. For $0 < \alpha < 1$ the eigenstate can be considered "non-ergodic" and its support set \mathcal{S}_β is sparse in the space of the marked states.

We express the transition probability from $|z_j\rangle$ to $|z\rangle$,

$$P(t, z|z_j) = \left| \sum_\beta \langle z|\psi_\beta\rangle \langle \psi_\beta|z_j\rangle e^{-iE_\beta t} \right|^2, \quad (5)$$

in terms of the eigenstates and corresponding eigenvalues of H , where $H|\psi_\beta\rangle = E_\beta|\psi_\beta\rangle$. In the delocalized phase, for a given state $|z_j\rangle$ there exists a large set of eigenstates $|\psi_\beta\rangle$ that have peaks at $|z_j\rangle$. These eigenstates possess important properties [35–37]: they have largely overlapping supports $\cap_\beta \mathcal{S}_\beta \approx \mathcal{S}(z_j)$, and they are close in energy thus forming a narrow mini-band. The mini-band width Γ may be interpreted as the inverse scrambling time and determines the width of the plateau in the Fourier-transform of the typical transition probability $\tilde{P}(\omega, z|z_j)$ [35].¹ In other words, the significant PT of $P(t, z|z_j)$ from the initial marked state $|z_j\rangle \in \mathcal{S}$ into the other states of the same miniband \mathcal{S} occurs over the time $t_{PT} \sim 1/\Gamma$. The window $\Delta\mathcal{E}_{cl}$ is related to the miniband width Γ .

Understanding the properties of non-ergodic delocalized states is crucial for describing the dynamics of quantum spin glasses driven by many-body coherent tunneling processes. Developing its microscopic theory is a challenging problem. This paper studies the transport problem in an "impurity band" (IB) model (3) by making use of the down-folded Hamiltonian in the marked state subspace derived in Secs. II, IV. While the original Hamiltonian (2) is sparse in the basis of states $|z\rangle$ (it couples only states separated by Hamming distance 1), the down-folded Hamiltonian \mathcal{H} (40) is a dense $M \times M$ matrix.

The transverse field leads to a uniform shift $\sim B_\perp^2$ of the marked state energies as shown in Sec. IV, (33)-(34). Diagonal elements of \mathcal{H}_{ii} are given by the marked state energies counted off from the center of the shifted impurity band. Their PDF is assumed to be exponentially bounded with some width W .

Each pair of marked states is coupled via multi-qubit tunneling. The off-diagonal matrix elements $\mathcal{H}_{ij} = V(d_{ij}) \cos \phi(d_{ij})$ are completely determined by the Hamming distance d_{ij} between the marked states z_i and z_j . The amplitude $V(d)$ decays steeply with d , inversely proportional to a square root of $\binom{n}{d}$ (see Eq. (41)). The phase ϕ shown in Fig. 5 monotonically increases by $\mathcal{O}(1)$ when d is changed by 1. In the analysis of spectral properties of \mathcal{H}_{ij} the quantity $\cos \phi(d_{ij})$ can be replaced by a random sign.

The typical distance between marked states is $n/2$ and the corresponding typical matrix element is $V_{typ} \sim$

$n^2 2^{-n/2} e^{-n/(4B_\perp^2)}$. The typical distance from a marked state to its nearest neighbor is extensive $d_{min} = \mathcal{O}(n)$ and the corresponding matrix element is exponentially small in n . However it is exponentially larger than its typical value V_{typ} . This fact corresponds to a strong hierarchy of the off-diagonal matrix elements of \mathcal{H}_{ij} which is a signature of their heavy-tailed probability density function [30, 34]. Such matrices are called Levi matrices.

The PDF of the rescaled squared amplitudes $w_{ij} = V^2(d_{ij})/V_{typ}^2$ derived in Sec. V B is

$$\text{PDF}(w) = \frac{1}{w^2 \sqrt{\pi \log w}}, \quad w \in [1, \infty). \quad (6)$$

The particular form of scaling is the direct consequence of the fact that our problem has no "structure": the tunneling matrix elements depend only on Hamming distance and marked states are chosen at random.

The key difference of the ensemble of matrices \mathcal{H}_{ij} from Levi matrices studied in the literature [30–32, 34] is that the dispersion, W , of the diagonal matrix elements is much larger than the typical magnitude of the off-diagonal elements V_{typ} . Therefore \mathcal{H}_{ij} can be called preferred basis Levi matrices (PBLM).

We note that the existence of heavy tails in the PDF of the off-diagonal matrix elements of the down-folded Hamiltonian \mathcal{H} is due to the infinite dimension of the Hilbert space of the original problem (2) for $n \rightarrow \infty$. This happens because the exponential decay of the matrix elements with the Hamming distance d is compensated by the exponential growth of the number of states at the distance d from a given state. We believe that the PBLM structure is a generic feature of the effective Hamiltonians for PT at the tail of the density of states in quantum spin glass problems.

Unlike the standard Levi ensemble, the eigenstates of PBLM allow for the existence of non-ergodic delocalized states when the width W is much bigger than the largest off-diagonal matrix element in a typical row of \mathcal{H}_{ij} and much smaller than the the largest off-diagonal element in a matrix

$$V_{typ} M^{1/2} \ll W \ll V_{typ} M. \quad (7)$$

For smaller dispersion $W \lesssim V_{typ} M^{1/2}$ the matrix eigenstates are ergodic while for $W \gtrsim V_{typ} M$ the eigenstates are localized. Such phase diagram resembles the one in the Rosenzweig-Porter (RP) model [33, 35]. The difference of RP from PBLM is that the statistics of the off-diagonal matrix elements in the RP ensemble are Gaussian [38] rather than polynomial (6). In this paper we will focus on exploring PT transfer within the non-ergodic delocalized phase, which is more likely to generalize to other models. We note that the localized phase does not support population transfer.

Because of the PBLM structure of the Hamiltonian \mathcal{H} one can expect that the runtime of the PT protocol t_{PT} will have a heavy-tailed PDF whose form is of practical

¹The same plateau width characterizes the frequency dependence of the eigenfunction overlap correlation coefficient $K(\omega) = M \sum_{j=1}^M \sum_{\beta, \beta'} |\langle j|\psi_\beta\rangle|^2 |\langle j|\psi_{\beta'}\rangle|^2 \delta(\omega - E_\beta + E_{\beta'})$ [35].

interest. It is closely related to the PDF of the miniband widths $\Gamma \sim 1/t_{\text{PT}}$. We obtained the $\text{PDF}(\Gamma)$ by making use of the cavity method for random symmetric matrices [29, 30, 32, 39].

In previous work the cavity equations were solved only in their linearized form, i.e., near the localization transition. We were able to solve fully nonlinear cavity equations in the delocalized non-ergodic phase. We obtained the boundaries of the phase in terms of the ratio of W/V_{typ} and also the form of $\mathcal{P}(\Gamma)$ inside the phase. It is given by the alpha-stable Levi distribution [30, 40] with the tail index 1, most probable value $\Gamma_{\text{typ}} = V_{\text{typ}}(\pi\Omega \log \Omega/4)^{1/2}$, and characteristic dispersion $\pi\Gamma_{\text{typ}}/(4\log \Omega)$ where Ω is the typical number of states in the miniband. This number $\Omega = (\pi MV_{\text{typ}}/W)^2$ is a square function of the ratio of the typical tunneling matrix element V_{typ} to the level separation W/M . In a non-ergodic delocalized phase $M \gg \Omega \gg 1$ and the typical PT time $t_{\text{PT}} \sim 1/\Gamma_{\text{typ}}$ obeys the condition

$$(M \log M)^{-1/2} \ll t_{\text{PT}} V_{\text{typ}} \sim (\Omega \log \Omega)^{-1/2} \ll 1. \quad (8)$$

We build on the observations made in the IB model and provide qualitative arguments that PT will have a quadratic speed up over QMC in some quantum search problems where tunneling is a computational bottleneck.

In Sec. II we develop a down-folding procedure to reduce the original problem to the nonlinear eigenproblem in the marked state subspace. In Sec. III we calculate the off-diagonal (tunneling) matrix elements of the downfolded Hamiltonian and studied their dependence on n and Hamming distance using an approach similar to the Wentzel-Kramers-Brillouin (WKB) theory. In Sec. IV we develop an expansion of the nonlinear eigenproblem near the center of the IB. We obtain the uniform shift of the band due to the transverse field and the explicit form of the effective Hamiltonian \mathcal{H} for the PT problem. We also investigate the vicinities of resonant values of B_{\perp} when the levels of the driver “cross” the impurity band and establish the condition for when the resonant effects can be neglected. In Sec. V we study the statistical properties of the ensemble of Hamiltonians \mathcal{H} , and obtain in explicit form the heavy-tailed distribution of the off-diagonal matrix elements. In Sec. VI we study the PT within the Born approximation calculating the distribution of the decay rates of a marked state into the miniband. In Sec. VII we provide an overview of the cavity method for dense random matrices. We also estimate the number of states in the miniband and discuss the implications for the PT runtime. In Sec. VIII we solve the cavity equations and obtain the distributions of the real and imaginary parts of self-energy. In Sec. IX we discuss the complexity of PT. In Sec. X we provide a comparison between PT and Grover’s algorithm with multiple target states, assuming systematic errors in the driver Hamiltonian weight and systematic phase errors in the quantum oracle, leading to a distribution of target state energies $\mathcal{E}(z_j)$ similar to that in IB model (3). We also compare

PT and Grover’s algorithm when the latter is initialized in one of the target states. Sec. XI discusses numerical results, Sec. XII is a qualitative discussion of application of our method to other problems beyond the IB model and we conclude our exposition in Sec. XIII.

II. DOWNFOLDING INTO THE SUBSPACE OF THE MARKED STATES AND NONLINEAR EIGENPROBLEM

The driver Hamiltonian H_D in Eq (2) connects bit-strings that are separated by a Hamming distance $d=1$. We note that, on one hand, marked states are separated by large Hamming distances d_{ij} with typical value $d = n/2$. Therefore a pair of marked states $|i\rangle$ and $|j\rangle$ is coupled by elementary spin-flip processes corresponding to high orders $(H_D)^k$ of the driver Hamiltonian with $k \geq d_{ij}$. On the other hand, the resolvent of the driver Hamiltonian

$$G(E) = \frac{1}{E - H_D}. \quad (9)$$

connects directly every pair of marked states. Furthermore, because H_D is invariant under permutations of bits, the matrix elements $G_{ij}(E) = \langle z_i | G(E) | z_j \rangle$ depend only on the Hamming distance d_{ij} between the corresponding states. They are exponentially small in n for extensive $d_{ij} = \mathcal{O}(n)$. Therefore, one might expect that under certain conditions the quantum evolution stays approximately confined to the marked state subspace and can be naturally described by the downfolded Hamiltonian whose $M \times M$ matrix representation is dense in the basis of marked states.

We use the identity

$$G(E)H_{\text{cl}}|\psi\rangle = |\psi\rangle, \quad (10)$$

where E and $|\psi\rangle$ is an eigenvalue and the corresponding eigenvector of H . We introduce a new vector

$$|\mathcal{A}\rangle = \sqrt{H_{\text{cl}}}|\psi\rangle \quad (11)$$

that has no support in the subspace orthogonal to that of marked states. Then, multiplying both parts of equation (10) by $\sqrt{H_{\text{cl}}}$, we obtain after simple transformations

$$(H_{\text{cl}} + \Lambda)|\mathcal{A}\rangle = E|\mathcal{A}\rangle, \quad (12)$$

where

$$\Lambda = \sqrt{H_{\text{cl}}}H_D G(E)\sqrt{H_{\text{cl}}}. \quad (13)$$

The operator Λ plays the role of a “driver Hamiltonian” in the downfolded picture, and it couples states in the marked subspace.

Equation (12) can be written in matrix form (see Ap-

pendix, Sec. A for details)

$$\sum_{j=1}^M \mathcal{H}_{ij}(E) \mathcal{A}_j = E \mathcal{A}_i, \quad (14)$$

where $\mathcal{A}_i = \langle \mathcal{A} | z_i \rangle$ and \mathcal{H}_{ij} is a dense symmetric $M \times M$ matrix

$$\mathcal{H}_{ij}(E) = \delta_{ij} \mathcal{E}(z_i) + \sqrt{\mathcal{E}(z_i) \mathcal{E}(z_j)} c_{ij}(E). \quad (15)$$

Here δ_{ij} is the Kronecker delta and

$$c_{ij}(E) = c(E, |z_i - z_j|) = \langle z_i | H_D \frac{1}{H_D - E} | z_j \rangle, \quad (16)$$

is a coupling coefficient that depends only on a Hamming distance $|z_i - z_j|$ between the bit-strings z_i and z_j .

We note that (14) has the form of a nonlinear eigenproblem. A solution of (14) for the M -dimensional vector $|\mathcal{A}\rangle$ with nonzero norm requires

$$\det[\mathcal{H}(E) - IE] = 0, \quad (17)$$

where I is the identity matrix. Because the downfolded Hamiltonian $\mathcal{H}(E)$ explicitly depends on the energy E , different roots E_β of the equation (17) correspond to different Hamiltonian matrices $\mathcal{H}_{ij}(E_\beta)$. This can be understood from the fact that the original $2^n \times 2^n$ Hamiltonian (2) couples the M dimensional marked state subspace to the rest of the Hilbert space. Therefore, the projections of the eigenvectors $|\psi_\beta\rangle$ of H onto the subspace are, in general, neither normalized nor orthogonal. The same is true for the corresponding vectors $|\mathcal{A}_\beta\rangle = \sqrt{H_{\text{cl}}} |\psi_\beta\rangle$. The normalization condition for the projections has the form (see Appendix A for details)

$$\sum_{j,i=1}^M \frac{1}{Q_{ji}(E_\beta)} \psi_\beta(z_j) \psi_\beta(z_i) = 1. \quad (18)$$

where

$$\frac{1}{Q_{ji}(E)} = \sqrt{\mathcal{E}(z_i) \mathcal{E}(z_j)} \frac{d}{dE} \left(\frac{\mathcal{H}_{ij}(E)}{E} \right). \quad (19)$$

This condition along with Eqs. (14)-(17) completely defines the eigenvector projections onto the marked state subspace and the corresponding eigenvalues.

We observe that there are exactly M roots E_β of (17) that originate from M classical energies of the marked states $\mathcal{E}(z_j)$ at $B_\perp = 0$. These eigenvalues and the corresponding eigenstates will be the sole focus of our study. Here we just mention briefly that the rest of the states originate in the limit $H_{\text{cl}} \rightarrow 0$ from the eigenstates of the driver Hamiltonian whose energy levels $-B_\perp(n - 2m)$ (shown in Fig. 1) correspond to the total spin- x projections $n - 2m \in [-n, n]$. The levels $-B_\perp(n - 2m)$ have degeneracy $\binom{n}{m}$, which is partially lifted due to the coupling to the impurity band with M states. The splitting of the

driver energy levels $-B_\perp(n - 2m)$ increases as a function of transverse field in the vicinity of “resonances” with the levels of the impurity band where $B_\perp(n - 2m) \approx -n$ for integer values of m . At resonance, the eigenstates of the driver with total spin- x projection $n - 2m$ are strongly hybridized with the marked states $|z_j\rangle$. As will be discussed below, the width of the resonances remains exponentially small in n for $B_\perp = \mathcal{O}(n^0)$. In Fig. 6 we plot the evolution of the energy spectrum of the Hamiltonian H as a function of transverse field for the case of two impurity states $M = 2$.

III. COUPLING COEFFICIENTS IN THE DOWNFOLDED HAMILTONIAN

The coupling coefficient $c_{ij}(E) \equiv c(E, d_{ij})$ for $i \neq j$ determines the off-diagonal matrix element of the downfolded Hamiltonian (15) corresponding to the tunneling transition that connects marked states $|z_i\rangle$ and $|z_j\rangle$. In the IB model, the tunneling matrix element depends only on the Hamming distance d_{ij} between the states. It can be calculated in explicit form from Eq. (16). For this we use the basis of eigenstates $|x\rangle$ of the driver Hamiltonian $H_D |x\rangle = H_D^x |x\rangle$ in Eq. (16). They correspond to bit-strings $x = (x^1, \dots, x^n)$ of individual qubits polarized in positive $x^a = 0$ and negative $x^a = 1$ direction of the x axis. The eigenvalues of the driver $H_D^x = -B_\perp(n - 2h_x)$ depend only on the Hamming weight of the bit-strings x . Therefore one can perform explicitly the partial summation over basis vectors $|x\rangle$ in (16) under the conditions that $\sum_a x^a = k$ for all bit positions a such that $z_j^a \neq z_i^a$, and $\sum_a x^a = l$ for all a where $z_j^a = z_i^a$. Finally the result (16) can be written as a double sum over $k \in (0, n - d_{ij})$ and $l \in (0, d_{ij})$

$$c_{ij}(E) = \sum_{k=0}^{n-d_{ij}} \sum_{l=0}^{d_{ij}} \binom{n}{k} \binom{n-d_{ij}}{l} \frac{(-1)^l 2^{-n}}{1 + \frac{E}{B_\perp(n-2k-2l)}}. \quad (20)$$

Here d_{ij} is the Hamming distance between bit-strings z_i and z_j . Plots of coupling coefficients as a function of Hamming distance d based on (20) are given in Fig. 2. They display qualitatively different behavior depending on the value of the parameter $nB_\perp/|E|$.

For $nB_\perp/|E| < 1$ the coefficient $c(E, d)$ decays exponentially with d in the entire range of values $d \in [0, n]$. For $nB_\perp/|E| > 1$ the coefficient decays until $d \sim n/2$, corresponding to minimum overlap between the marked states, and then begins to grow. For large transverse field $B_\perp \gg 1$ the behavior with d is nearly symmetric with respect to $d = n/2$ and to leading order it does not depend on B_\perp . Unfortunately, the expression (20) is quite involved and is not suitable for the study of the asymptotic properties of the population transfer in the limit of large n .

For a very weak transverse field $B_\perp \ll n^{-1/2}$ using perturbation theory in B_\perp to the leading order one can

[width= 3.35in]cartoon-levels

Figure 1. Cartoon of the level diagram. Horizontal blue lines depict the energy levels $-B_\perp(n - 2m)$ of the driver Hamiltonian H_D in Eq. (2) separated by $2B_\perp$. A narrow impurity band of width $W \ll B_\perp$ is marked in light green. The sequence of short black lines depicts the energies of marked states $\mathcal{E}(z_i)$. Dashed lines depict the elementary path to leading order perturbation theory in B_\perp for the tunneling matrix element $c_{ij}(E)$ given in (16). In this paper we focus on the case of relatively large transverse fields $B_\perp > 1$ so that the IB energies lie above the ground state of the total Hamiltonian (2) that corresponds to nearly all qubits polarized in x direction.

obtain a standard expression [26] for the coupling coefficient, $|c(E, d)| \simeq d!(B_\perp/n)^d$. It is given by the sum of the transition amplitudes over the $d!$ shortest paths between the states $|z_i\rangle$ and $|z_j\rangle$ separated by a Hamming distance d . Intermediate states $|z\rangle$ along each path correspond to $\mathcal{E}(z) = 0$ while energies of initial and final states are $-n$ (see Fig. 1).

For larger transverse field values (but still $B_\perp \ll 1$) the perturbative expression in the small- B_\perp limit can be modified to include the range of $B_\perp = \mathcal{O}(n^0)$ but $B_\perp \ll 1$. In that range

$$|c(E, d)| \simeq d! \left(\frac{B_\perp}{n} \right)^d e^{B_\perp^2 \left(\frac{d^2(3n-2d)}{6n^2} + \frac{n}{12} \right)}. \quad (21)$$

One can see that, contrary to the conclusion in [26], for small B_\perp matrix element falls down with d extremely steeply despite the presence of the factorial factor $d!$ in (21).

For large transverse field, $B_\perp > |E|/n$, the dependence of $c_{ij}(E)$ on d_{ij} becomes non-monotonic, reaching its minimum at the point $n/2$ of minimum overlap between the bit-strings z_i and z_j . In a certain region around the minimum it has oscillatory behavior, as seen in Fig. 2. The boundary of this region is shown with black dots. The details of the behavior in the oscillatory region are shown in Fig. 4. The exponential dependence of the envelope of $c(E, d)$ on d is captured by the factor $1/\binom{n}{d}$ and is independent on the transverse field strength. This region of d and values of $B_\perp > |E|/n$ are of the most relevance to the present discussion.

In this paper we develop an approach (described in the Appendix B) based on the WKB theory for large spin [41] to calculate the coefficient $c(E, d)$ for $n \gg 1$ and arbitrary values of transverse fields B_\perp without relying on perturbation theory in B_\perp . The coefficient $c_{ij}(E)$ can be expressed in terms of the operator of the total spin- x projection $S_x = 1/2 \sum_{j=1}^n \sigma_x^j$

$$c_{ij}(E) = \delta_{ij} - E \langle z_i | (E + 2B_\perp S_x)^{-1} | z_j \rangle. \quad (22)$$

We will utilize the basis of eigenstates $|m\rangle$ of the operator $S_z = \sum_{k=1}^n \sigma_z^k$ corresponding to its eigenvalues $m \in [-n/2, n/2]$ and the maximum value of the total

spin $S = n/2$

$$S_z |m\rangle = m |m\rangle, \quad m = -n/2, \dots, n/2. \quad (23)$$

The state $|n/2 - d\rangle$ is a normalized sum of all computational basis states $|z\rangle$ with d spins pointing in the negative z direction and $n - d$ spins pointing in the positive z direction ($m = n/2 - d$)

$$|n/2 - d\rangle = \frac{1}{\sqrt{\binom{n}{d}}} \sum_{z \in \{0,1\}^n} \delta_{|z|, d} |z\rangle. \quad (24)$$

Here $|z| = \sum_{k=1}^n z^k$ and $\delta_{k,d}$ is a Kronecker delta.

Because the coefficients $c_{ij}(E)$ (20) depend only on the Hamming distance $|z_i - z_j|$ between the bit-strings z_i and z_j , we can assume, without loss of generality, that in Eq. (22) one of the bit-strings, e.g., $|z_j\rangle$, corresponds to all individual spins pointing in the positive z direction

$$|z_j\rangle = |00\dots 0\rangle \equiv |n/2\rangle \quad (m_z = n/2) \quad (25)$$

The main observation is that we can pick, instead of the state $|z_i\rangle$, any computational basis state $|z\rangle$ whose Hamming weight satisfies the condition $|z| = |z_i|$ without changing the value of the coefficient $c_{ij}(E) = c(E, |z_i|)$. Therefore averaging both sides of the Eq. (22) over the states $|z_i\rangle$ that satisfy the condition $|z_i| = d$ for some integer $d \in [0, n]$ we obtain

$$c(E, d) = \delta_{d,0} - \frac{E}{\sqrt{\binom{n}{d}}} G_{\frac{n}{2}-d, \frac{n}{2}}(E). \quad (26)$$

Here $G_{m, \frac{n}{2}}(E) = \langle m | (E + 2B_\perp S_x)^{-1} | n/2 \rangle$ are the matrix elements of the resolvent (9) of the transverse field Hamiltonian H_D between the states (24) that belong to a maximum total spin subspace $S = n/2$.

As will be shown below, for typical instances of the ensemble of Hamiltonians H , the Hamming distance from a randomly selected marked state to its closest neighbor is an extensive quantity $\mathcal{O}(n)$. Therefore the above off-diagonal matrix elements of the resolvent can be analyzed in a semiclassical approximation corresponding to $S = n/2 \gg 1$. This approximation for the quantum propagator of a large spin and *diagonal* elements of the resolvent was considered in [42, 43] using the spin coherent state path-integral representation. The analysis in these papers was quite involved because the path-integral formulation requires a careful treatment of the fluctuation determinant and a so-called Solari-Kochetov correction in the action. Also, these results were focused on a general case of large spin Hamiltonian and only considered *diagonal* elements of the resolvent. Because of this, instead of trying to extend the results in [42, 43] to our case, we follow a different path.

The resolvent satisfies the equation

$$I - 2B_\perp S_x G(E) = E G(E)$$

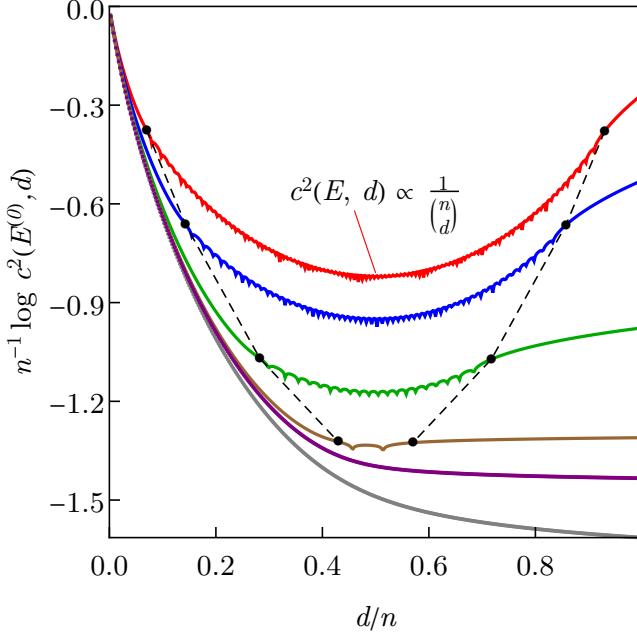


Figure 2. Colored lines show the dependence of the rescaled logarithm of the coupling coefficient $n^{-1} \log c^2(E, d)$, Eq. (20), on the rescaled Hamming distance d/n for $n = 400$. The energy E is set to the value $E^{(0)} \simeq -n - B_{\perp}^2$ that reflects the overall shift of the impurity band due to the transverse field (cf. (33),(34)). Different colors correspond to different values of the transverse field $B_{\perp} = 1.93$ (red), 1.43 (blue), 1.11 (green), 1.01 (brown), 0.99 (purple), 0.95 (gray). The scale along the y -axis suggests that $c(E^{(0)}, d)$ scales exponentially with n for $d/n = \mathcal{O}(n^0)$. The inset shows the leading order factor in the d -dependence of the coupling coefficient for $B_{\perp} > |E|/n$ (cf. (30)). Black dots show the boundaries $d = n/2 - m_0, n/2 + m_0$ of the region of the oscillatory behavior of $c(E, d)$ with d given by WKB theory (29) (see Appendix B for details).

where I is the identity operator. We write this equation in the basis of states $|m\rangle$ (23). From (9) we obtain

$$\delta_{m, \frac{n}{2}} + \sum_{s=\pm 1} u(m - s/2) G_{m+s, \frac{n}{2}} = E G_{m, \frac{n}{2}}, \quad (27)$$

$$u(m) = -B_{\perp} \sqrt{L^2 - m^2}, \quad L = \frac{n+1}{2}. \quad (28)$$

In the limit of large $n \gg 1$ we solve this equation using the discrete Wentzel-Kramers-Brillouin (WKB) approximation method [41, 44]. In the WKB analysis of Eq. (27) the function $2u(m)$ plays the role of an effective potential for the classical system with coordinate m and energy E . For $2u(m) > E$ the WKB solution for the resolvent $G_{m, n/2}(E)$ displays an oscillatory behavior with m while for $2u(m) < E$ it exponentially increases with m . The boundaries of the oscillatory region $m \in [-m_0(E), m_0(E)]$ are “turning points” of the classical motion and are given by the condition $2u(m_0) = E$

(see Fig. 3) where

$$m_0 = \sqrt{L^2 - \left(\frac{E}{4B_{\perp}}\right)^2}. \quad (29)$$

In Fig. 4 we plot the comparison between the coefficient $c(E, d)$ computed based on the exact expression (20) and the WKB asymptotic (details of the WKB analysis are given in Appendix B).

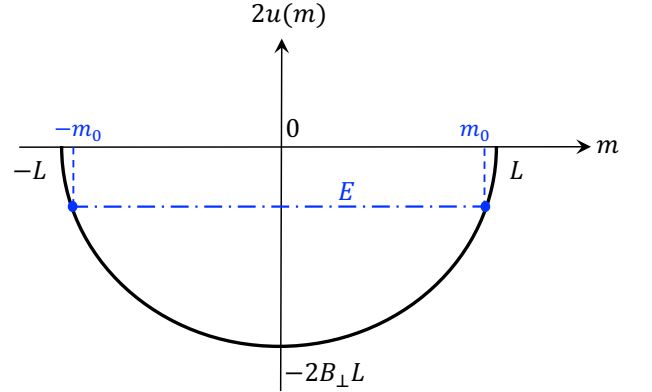


Figure 3. The black line shows the E -dependence of the turning points $m = \pm m_0(E)$ given by Eq. (29). It ends at the interval boundaries $\pm m = L = (n+1)/2$. The horizontal dashed blue line depicts the region of oscillatory behavior of $G_{m, n/2}(E)$ with m for a given E described by the WKB solution (30) (see also Eq. (B5) in Appendix) and shown in Fig. 4. The regions of $m \in [m_0(E), L] \cup [-L, -m_0(E)]$ correspond to the exponential growth of $G_{m, n/2}(E)$ with m . The WKB solution for the right region is given in Eq. (B10).

In what follows we will be interested in the region $d \in [n/2 - m_0, n/2 + m_0]$ with $m_0 \simeq \sqrt{(n/2)^2 - (E/B_{\perp})^2}$ defined by the condition $u(m_0) = E$. This is the region of oscillatory behavior of $c(E, d)$ with d where the leading order exponential dependence on n is given by the expression

$$c(E, d) \propto \frac{1}{\sqrt{\binom{n}{d}}} e^{-n\theta(B_{\perp})} \sin \phi(E, d), \quad (30)$$

with the prefactor given in Appendix, Eqs. (B23),(B24).

The function $\theta(B_{\perp})$ in (30) equals

$$\theta(B_{\perp}) = \frac{2 \operatorname{arctanh}(B_{\perp}^{-1}) + B_{\perp} \ln(1 - B_{\perp}^{-2})}{4B_{\perp}}. \quad (31)$$

It behaves at large argument as $\theta \simeq 1/(4B_{\perp}^2)$.

An explicit form of the WKB phase $\phi(E, d)$ in (30) is given in Appendix, Eq. (B11). The dependence of the phase on d for different values of B_{\perp} is shown in the Fig. 5. This phase varies by $\mathcal{O}(1)$ when d is changed by 1 and it is responsible for fast oscillation of the coupling coefficient with the Hamming distance between marked

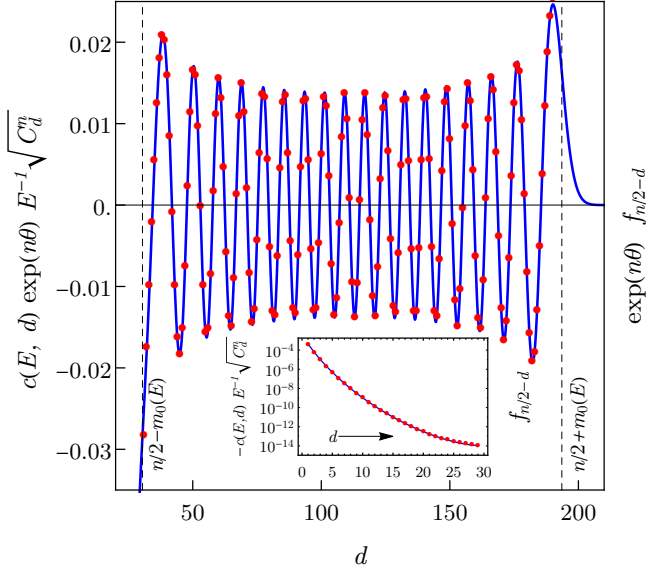


Figure 4. The blue curve shows the d -dependence of the (rescaled) coupling coefficients $c(E, d)$ computed from the exact expression (20) with $n = 224$ and $E = -226.15$. We denote the binomial coefficient as $\binom{n}{d} \equiv C_d^n$. The transverse field is $B_\perp = 1.459$. For this value of B_\perp the impurity band levels $\mathcal{E}(z_j)$ lie approximately in the middle of the interval between the $p = 34$ th and $p = 35$ th excited energy levels $-B_\perp(n - 2p)$ of the driver Hamiltonian. Red points depict the d -dependence of the same rescaled coefficients $c(E, d)$ given by $G_{n/2-d, n/2} \exp(n\theta)$ and determined by the asymptotic WKB expressions given in Appendix (see (B10), (B13)). Dashed lines indicate the boundaries of the oscillatory behavior of the WKB solution (B9). The inset shows the plot for the exponential d -dependence of the rescaled coupling coefficient $-c(E, d)$ in the region of its monotonic behavior $d \in [1, n/2 - m_0(E)]$ (cf. Eqs. (B13), (26)). The solid blue line corresponds to the exact expression (20), while the approximate WKB solution is shown with red points.

states d . Its dependence on d simplifies in the limit of large transverse field $B_\perp \gg 1$:

$$\phi(E, d) \simeq \frac{\pi d}{2} - \frac{\pi n}{4} \frac{\chi(1/2 - d/n)}{B_\perp}, \quad (32)$$

where $\chi(x) \simeq 1 - 2 \arcsin(x)/\pi + \mathcal{O}(n^{-1})$. The second term in (32) is much smaller than the first one, and varies very little when d is changed by 1. A predominately linear dependence of $\phi(E, d)$ on d at large fields can be seen in Fig. 5. This property will be important in the analytical study of population transfer.

For large transverse fields the magnitude of the squared coupling coefficient (30) can be estimated to exponential accuracy as $c^2(E, d) \sim \exp[-n/(2B_\perp^2)]/\binom{n}{d}$. We note that the number of marked states M_d accessible via all possible d -bit flips from a given state is $M_d = M 2^{-n} \binom{n}{d}$. Therefore the leading order dependence of the coupling coefficient on d is proportional to $1/\sqrt{M_d}$. As will be shown later, in the limit of large transverse fields this

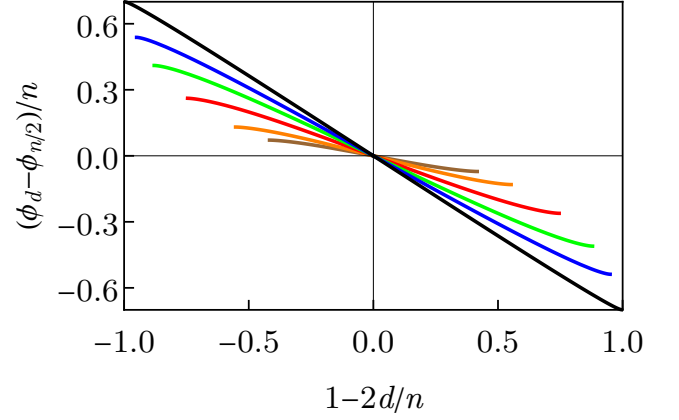


Figure 5. Plots of the WKB phase $\phi_d \equiv \phi(E, d)$ of the oscillations of the coupling coefficient $c(E, d)$ with the Hamming distance d for a number of qubits $n = 1000$. Both axes are rescaled by n . The phase is plotted relative to its value at $d = n/2$. We set the energy $E = E^{(0)}$ where $E^{(0)} \simeq -n - B_\perp^2$ reflects the overall shift of the impurity band due to the transverse field (cf. (33), (34)). Different color curves correspond to different values of $B_\perp > |E|/n$ with $B_\perp = 1.1$ (brown), $B_\perp = 1.2$ (orange), $B_\perp = 1.5$ (red), $B_\perp = 2.1$ (green), $B_\perp = 3.2$ (blue), $B_\perp = 10$ (black). Each curve varies in its own range $n/2 - d \in [-m_0, m_0]$ where m_0 is given in (29) and determines the region of oscillatory behavior of the coupling coefficients (see Appendix B for details). For $B_\perp \simeq 1$ the region of oscillatory behavior shrinks to a point $d \simeq n/2$. In the limit of large values of $B_\perp \gg 1$ this behavior occupies almost the entire range $d \in [0, n]$.

leads to a nearly Grover complexity of the PT algorithm, up to a factor $\sim \exp[-n/(4B_\perp^2)]$, which gives very small correction to Grover scaling for large B_\perp . However when d decreases below the boundary value $d < n/2 - m_0$, the coupling coefficient grows exponentially faster than $1/\sqrt{M_d}$, as follows from the discussion in Appendix (cf. Eq. (B13)).

IV. DOWNFOLDED HAMILTONIAN NEAR THE CENTER OF THE IMPURITY BAND

The coupling coefficients $c(E, d)$ (20) decay exponentially with Hamming distances for $d = \mathcal{O}(n)$ (see details in Sec. III). Marked states are selected at random and Hamming distances between them are order n when the number of the states M is exponentially smaller than 2^n . Because the off-diagonal matrix elements of the downfolded Hamiltonian $\mathcal{H}_{ij}(E) \propto c(E, d_{ij})$ they are exponentially small in n . At the same time the width of the distribution of energies of the marked states $\mathcal{E}(z_j) = -n + \epsilon_j$ is also assumed to be very small, $W \ll B_\perp$ (it is exponentially small in n for the cases of interest). Therefore we can solve the nonlinear eigenvalue problem (14)-(17) by an iterative approach treating the off-diagonal part of $\mathcal{H}(E)$ and terms $\propto \epsilon_j$ as a perturbation. Details are given in Appendix C.

At zeroth-order in the perturbation, the down-folded Hamiltonian $\mathcal{H}_{ij}^{(0)}(E) = \delta_{ij}n(c(E, 0) - 1)$ has one M -fold degenerate energy level $E^{(0)}$ that is a root of the equation $\mathcal{H}_{ij}^{(0)}(E) = E$ that originates from the marked state energy, $E^{(0)} \rightarrow -n$, in the limit of $B_{\perp} \rightarrow 0$. Using $c(E, 0)$ from Eqs. (16), (20) the explicit form of the equation for $E^{(0)}$ is

$$E^{(0)} = -n - \Delta_0, \quad (33)$$

$$\Delta_0 = n2^{-n} \sum_{d=0}^n \binom{n}{d} \frac{B_{\perp}(n-2d)}{n + \Delta_0 - B_{\perp}(n-2d)}. \quad (34)$$

Here Δ_0 is the root of the above transcendental equation that satisfies the condition $\lim_{B_{\perp} \rightarrow 0} \Delta_0 = 0$. In general, the sum (34) is dominated by the region of values of d such that $|d - n/2| = \mathcal{O}(n^{1/2})$ where the factor $2^{-n} \binom{n}{d}$ reaches its maximum $\sim n^{-1/2}$. In that region we replace the binomial coefficient with a Gaussian function of d and the summation with the integral over d . Taking the integral we obtain Δ_0 in a form of a series expansion in powers of n^{-1}

$$\Delta_0 \simeq -B_{\perp}^2 - \frac{B_{\perp}^4}{n} + \mathcal{O}(n^{-2}), \quad (35)$$

A comparison between the exact and asymptotic solutions for Δ_0 is shown in Fig. 6. For $B_{\perp} \ll n^{1/2}$ the overall shift of the energies of the marked states is negative and quadratic in B_{\perp} .

According to Eq. (18) all M degenerate eigenstates $|\psi\rangle_{\beta}$ have the same weight $Q(E^{(0)}) = \sum_{j=1}^M |\psi_{\beta}^{(0)}(z_j)|^2$ on the marked state subspace. In the large n limit we have

$$Q(E^{(0)}) \simeq 1 - \frac{B_{\perp}^2}{n} + \mathcal{O}(B_{\perp}^4/n^2). \quad (36)$$

Again, assuming that $\propto B_{\perp}^2/n \ll 1$, the eigenstates are dominated by their projections on the marked state subspace.

We observe that when B_{\perp} is increasing, $E^{(0)}$ repeatedly “crosses” one of the eigenvalues of the driver Hamiltonian, $E^{(0)} = -B_{\perp}(n-2m)$ for integer values of m , as shown in Fig. 6. As a result the denominator in Eq. (34) corresponding to $d = m$ will become zero at a “resonant” transverse field value $B_{\perp} = B_{\perp m}$ which is a root of the equation

$$B_{\perp m} = \frac{n + \Delta_0(B_{\perp m})}{n - 2m}, \quad (37)$$

approximately given by $B_{\perp m} \simeq n/(n-2m)$. For the magnitude of the transverse fields $B_{\perp} \ll \sqrt{n}$ where perturbation theory applies, levels of the driver that can cross with the impurity band satisfy the condition $n/2 - m \gg n^{1/2}$.

Near the m th resonance the term with $d = m$ in the

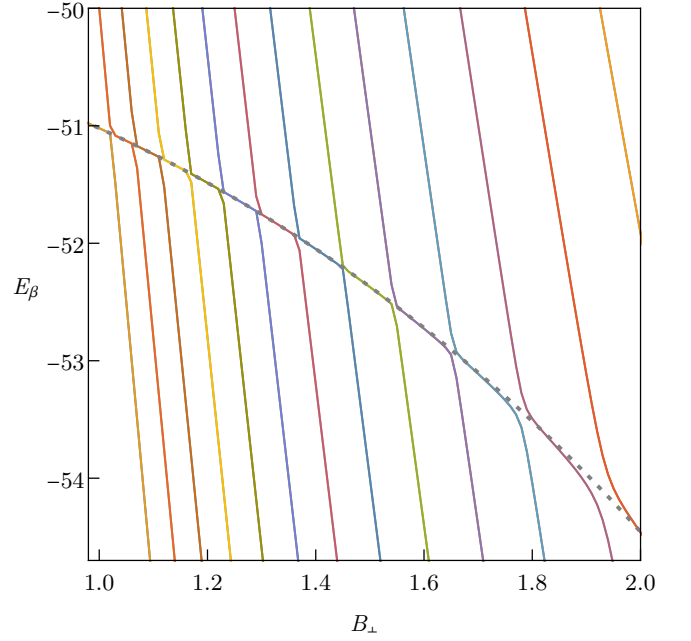


Figure 6. Solid lines show the dependence on the transverse field B_{\perp} of the eigenvalues E_{β} of the non-linear eigenvalue problem with Hamiltonian $\mathcal{H}(E)$ for the case of $n = 50$ and $M = 2$. The plot shows the repeated avoided crossing between the two systems of eigenvalues. One system (colored lines) corresponds to the eigenvalues of the transverse field (driver) Hamiltonian $H_D = -B_{\perp} \sum_{k=0}^n \sigma_x^k$ in the limit $H_{cl} \rightarrow 0$. The second system of eigenvalues corresponds to the energies of the two marked states in the limit $B_{\perp} \rightarrow 0$. The splitting of the eigenvalues is exponentially small in n and not resolved in the plot. The asymptotic expression (33),(34) for the two eigenvalues $E_{1,2}^{(0)} = E^{(0)}$ neglecting the tunneling splitting and setting $\mathcal{E}(z_j) = -n$ for all $j \in [1, M]$ are shown with dashed gray line.

sum (34) becomes anomalously large due to a small denominator despite the factor p_m being very small. One can show that the width of the resonance region is given by

$$\Delta B_{\perp m} \sim 2^{-n/2} \binom{n}{m} B_{\perp m}. \quad (38)$$

There the weight factor Q is decreasing dramatically (cf. Fig. 7) and the above perturbation theory breaks down. This corresponds to the hybridization of the marked states with the eigenstates of the transverse field operator H_D corresponding to its eigenvalue $-B_{\perp}(n-2m)$. The width of the resonant regions $\Delta B_{\perp m}$ (38) grows rapidly with m due to the increase in the degeneracy of the corresponding eigenvalue of H_D . However it remains exponentially small in n for $n/2 - m \gg n^{1/2}$.

In this study we will only focus on the off-resonance case depicted in Fig. 1. We note that when B_{\perp} becomes parametrically large compared to unity, one needs to make sure that n is also large enough so that the width

of the neighboring resonances is small. This dependence is shown in Fig. 8. Away from resonance, all M impurity band eigenstates are well localized in the marked states subspace (cf. (36)).

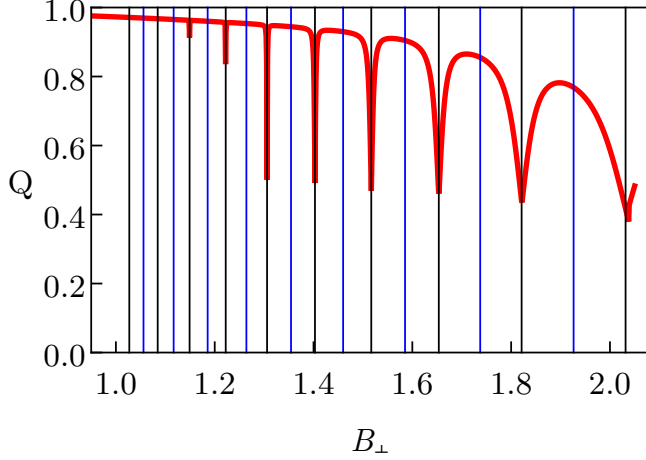


Figure 7. The solid red line shows the dependence of the total weight Q vs transverse field B_\perp for $n = 40$. Vertical black and blue lines correspond to the locations of p -even and p -odd resonances $B_\perp = B_{\perp m}$ (37), respectively. The total weight undergoes sharp decreases in the vicinity of even resonances. For $m < 5$ the resonance regions are so narrow that dips in Q are not seen. The width of the regions grow exponentially with m .

In the spirit of the degenerate perturbation theory, there exists an effective Hamiltonian \mathcal{H} that determines the correct zeroth order eigenstates and removes the de-

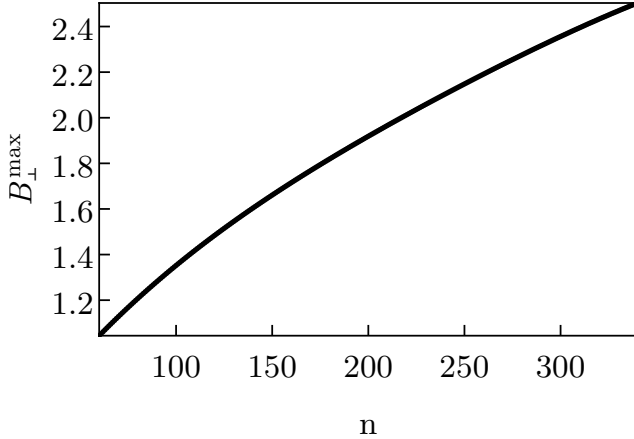


Figure 8. Plot of the maximum value of the transverse field at mid-resonance point B_\perp^{\max} as a function of n . The value of B_\perp^{\max} for a given n is defined as follows. We compute the weight factor $Q = Q(B_\perp)$ at a sequence of values of B_\perp taken at mid-resonance points $B_{\perp m}^* = (B_{\perp m} + B_{\perp m+1})/2$ with $m = 0, 1, \dots$. We determine the maximum value $m = m_{\max}$ for which $Q(B_{\perp m}^*) \geq 0.98$. Then $B_\perp^{\max} = B_{\perp m_{\max}}^*$.

generacy of the energy levels

$$\mathcal{H} |\psi_\beta^{(0)}\rangle = E_\beta^{(1)} |\psi_\beta^{(0)}\rangle, \quad (39)$$

Its matrix in the basis of the marked states has the form $\mathcal{H}_{ij} = \delta_{ij}\epsilon_i + nc(E^{(0)}, d_{ij})$ where we neglected small non-important corrections (see Appendix C). Using the expression for the coupling coefficient (30) given in Appendix B, ((B23),(B24)) we have

$$\mathcal{H}_{ij} = \delta_{ij}\epsilon_j + (1 - \delta_{ij})\mathcal{V}_{ij}\sqrt{2}\sin\phi(d_{ij}). \quad (40)$$

Here $\phi(d) \equiv \phi(E^{(0)}, d)$ is a WKB phase shown in Fig. 5 that describes the oscillation of the matrix elements with the Hamming distance. Its explicit form is given in Appendix B, Eq. (B11) and also above in Eq. (32) for the case of large transverse fields. The amplitude \mathcal{V}_{ij} equals

$$\mathcal{V}_{ij} \equiv V(d_{ij}), \quad V(d) = \sqrt{A(d/n)} \frac{n^{5/4} e^{-n\theta(B_\perp)}}{\sqrt{\binom{n}{d}}}, \quad (41)$$

where $i \neq j$ and the coefficient $A(\rho)$ equals (cf. (B24))

$$A(\rho) = \sqrt{\frac{\pi}{32}} \frac{e^{-B_\perp \operatorname{arccoth} B_\perp}}{(B_\perp^2 - 1)v(\rho)\sin^4(\phi(n/2))}, \quad (42)$$

$$v(\rho) = \left(1 - \frac{(1 - 2\rho)^2}{1 - B_\perp^{-2}}\right)^{1/2}. \quad (43)$$

It is independent on n apart from the phase $\phi(n/2)$ whose explicit form is

$$\phi(n/2) = \frac{\pi}{4} (n(1 - B_\perp^{-1}) - B_\perp). \quad (44)$$

The function $\theta(B_\perp)$ is given in (31). Expanding (31) in the limit $B_\perp \gg 1$,

$$\theta \simeq \frac{1}{4B_\perp^2} + \frac{1}{24B_\perp^4} + \frac{1}{60B_\perp^6} + \dots \quad (45)$$

In that limit $\theta \ll 1$. We note that even for modest values of transverse field, e.g., $B_\perp \simeq 1.46$ (corresponding to that in the Fig. 4) the first term provides a good estimate to the value of $\theta \simeq 0.13$ (error 9%). We shall refer to \mathcal{H} in (40) as the Impurity Band (IB) Hamiltonian.

The form of the IB Hamiltonian (40) only applies to the region of oscillatory behavior $d_{ij} \in [n/2 - m_0, n/2 + m_0]$ of the coupling coefficients $c_{ij}(E)$ with Hamming distance d_{ij} where m_0 is given in (29). This above condition for d_{ij} is always satisfied in a typical row of the matrix d_{ij} for the values of M considered in the paper (see the discussion in Appendix D and Eq. (D32)).

V. STATISTICAL ENSEMBLE OF THE IMPURITY BAND HAMILTONIANS

Properties of the eigenstates and eigenvalues (39) of the IB Hamiltonian \mathcal{H} (40) determine the population transfer within the Impurity Band and are thus of the central interest for us in this study. They depend on the statistical ensemble of IB Hamiltonians. In the model considered in this paper diagonal elements ϵ_j of \mathcal{H} are selected at random, independently from each other and from the choice of the corresponding marked states $|z_j\rangle$. We shall assume that the PDF $p(\epsilon)$ of ϵ_j is symmetric around zero and is well localized (exponentially bounded) with the width W

$$p(\epsilon) = \frac{1}{W} p_A(\epsilon/W), \quad \int_{-\infty}^{\infty} dx p_A(x) = 1. \quad (46)$$

The specific form of the PDF $p_A(x)$ is not important for the results. For calculations we will use the Gaussian, $p_A(x) = \frac{1}{\sqrt{2\pi}} \exp\left(-\frac{x^2}{2}\right)$, and step-function, $p_A(x) = \theta\left(\frac{1}{2} - |x|\right)$, PDFs where $\theta(x)$ is a Heaviside theta function. For the physical effects discussed in the paper to take place the width W needs to scale down exponentially with n

$$\lim_{n \rightarrow \infty} \log(W^{1/n}) = \mathcal{O}(n^0). \quad (47)$$

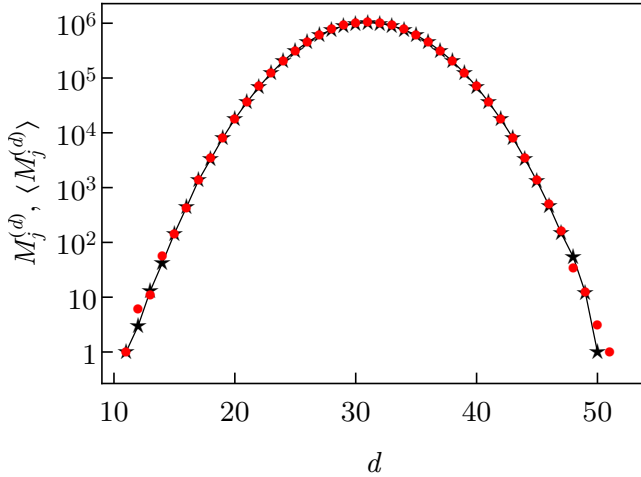


Figure 9. Red points show the empirical probability distribution $M_j^{(d)}$ vs d with $M_j^{(d)} = \sum_{j=1}^M \delta(d_{ij} - d)$. Here d_{ij} is a matrix of Hamming distances d_{ij} between the set of M randomly chosen n -bit-strings (marked states) and i is a randomly chosen marked state. The distribution corresponds to $M = 10^7$ and $n = 60$. Black stars connected by a black line show the samples m_d from multinomial distribution with mean values $\langle M_j^{(d)} \rangle = M p_d$ where p_d is binomial distribution (49).

A. Off-diagonal matrix elements

1. Statistical independence of matrix elements

For fixed energies ϵ_j the matrix of the IB Hamiltonian \mathcal{H}_{ij} is entirely determined by the symmetric matrix of Hamming distances d_{ij} between the bit-strings corresponding to the marked states. The set of M bit-strings is randomly sampled (without replacement) from the full set of all possible 2^n bit-strings $\{0, 1\}^n$. Instead of this ensemble one can consider a different one, where each of the M bit-strings is sampled *with replacement* from the full set $\{0, 1\}^n$. In this ensemble Hamming distances d_{ij} for distinct pairs i, j are statistically independent allowing for much simpler statistical averaging. Indeed, for a given row i of the matrix d_{ij} the joint probability distribution of the two distinct off-diagonal matrix elements can be estimated as

$$p_{d_{ij_1}, d_{ij_2}} - p_{d_{ij_1}} p_{d_{ij_2}} \propto \frac{1}{2^n} \Delta(d_{ij_1} - d_{ij_2}) p_{d_{ij_1}}. \quad (48)$$

Here $\Delta(d)$ denotes the Kronecker delta, $j_1 \neq j_2 \neq i$ and p_d corresponds to the modified binomial distribution

$$p_d = \frac{1}{Z} 2^{-n} \binom{n}{d}, \quad Z = \sum_{d=1}^n 2^{-n} \binom{n}{d} \quad (49)$$

(also $\sum_{d=1}^n p_{d_1, d_2} = 1$). One can see that the statistical correlation between a pair of Hamming distances d_{ij_1}, d_{ij_2} is exponentially small (in n) and can be neglected.

Such an ensemble allows for multiple copies of the same bit-string to be sampled. However this effect is not statistically significant for modest values of M

$$1 \ll M \ll 2^{n/2}. \quad (50)$$

This can be seen by comparing the number of ways to perform unordered sampling of M elements from the group of 2^n elements with and without replacement. Using Stirling's formula we write the former number as,

$$\binom{2^n + M - 1}{M} \simeq \binom{2^n}{M} \exp\left(\frac{M^2}{2^n}\right) (1 + \varepsilon), \quad (51)$$

where the latter number is given by $\binom{2^n}{M}$ with $\varepsilon \sim M 2^{-3n/4} \ll 1$. It is clear that when condition (50) is satisfied the two ensembles are statistically equivalent because repetitions can be neglected.

In summary, matrix elements of the matrix d_{ij} above or below main diagonal will be considered independent from each other and taken from the binomial distribution p_d . Then, for a given row of the matrix $M \times M$ of Hamming distances d_{ij} , the numbers of elements $M_j^{(d)}$ with $d_{ij} = d$ are samples from the multinomial distribution with mean values $\langle M_j^{(d)} \rangle = M p_d$. This property can be clearly seen from the Fig. 9. According to (40), (30) the statistical

ensemble of IB Hamiltonians (40) corresponds to that of symmetric random matrices whose associated graphs are fully connected and matrix elements are statistically independent.

Spectral properties associated with the local resolvent of the random matrices of this type can be studied with the cavity method [30–34] which is asymptotically exact in this case. In an analysis with the cavity method, the matrix elements always enter in a *squared* form, $(\mathcal{H}_{ij})^2$. As will be seen below the spectral properties of \mathcal{H} that are relevant for our study are determined by \mathcal{V}_{ij}^2 and not by the oscillatory factor in (40). Therefore we will be interested in the PDF of \mathcal{V}_{ij}^2 .

$$P(\mathcal{V}_{ij}^2) = \sum_{d=1}^n p_d \delta(V^2(d) - \mathcal{V}_{ij}^2), \quad (52)$$

where $i \neq j$.

2. Typical and extreme values of the off-diagonal matrix elements \mathcal{V}_{ij}

For a randomly chosen row of the matrix of Hamming distances d_{ij} the most probable value (mean) of its elements equals to $n/2$. According to (41), the off-diagonal matrix elements \mathcal{V}_{ij} decrease rapidly with the Hamming distance d_{ij} , reaching the minimum value at $d_{ij} \simeq n/2$. Therefore a typical minimum value of the matrix elements \mathcal{V}_{ij} corresponds to a typical value overall. We estimate it using Eq. (41) and Stirling's approximation

$$V_{\text{typ}} = V(n/2) \simeq \left(\frac{\pi A^2}{2} \right)^{1/4} n^2 2^{-n/2} e^{-n\theta}. \quad (53)$$

where coefficient $A = A(E^{(0)}, 1/2)$ (42) is essentially n -independent between the resonances (37) and θ is given in (31). The matrix elements \mathcal{V}_{ij} that scale with n as the typical value in (53) correspond to $|n/2 - d_{ij}| = \mathcal{O}(\sqrt{n})$.

We note that in the Fig. 9 the plot points do not reach the boundaries of the interval $d = 0, n$. In the matrix of Hamming distances d_{ij} the typical smallest off-diagonal element in a randomly chosen row can be estimated as follows $M p_{d_{\min}} = 1$ where p_d is binomial distribution (49)

$$\min_{j \neq i, 1 \leq j \leq M} d_{ij} \sim d_{\min}, \quad M 2^{-n} \binom{n}{d_{\min}} = 1. \quad (54)$$

Using Stirling's approximation for factorials in the limit $n \gg 1$ it is easy to show that minimum Hamming distance in a row is very close to the mean distance for $\log_2 M \ll n$

$$d_{\min} \simeq \frac{n}{2} - \sqrt{\frac{n \log_2 M}{2}}. \quad (55)$$

The minimum distance is extensive for $\log_2 M = \mathcal{O}(n^0)$. The typical largest magnitude off-diagonal matrix ele-

ment in a randomly chosen row of \mathcal{V}_{ij} is equal to $V(d_{\min})$. Using Stirling's approximation in (41) we get

$$\max_{j \neq i, 1 \leq j \leq M} |\mathcal{V}_{ij}| \sim M^{1/2} V_{\text{typ}}. \quad (56)$$

Using (53) one can see that the maximum off-diagonal matrix element in a randomly chosen row is still exponentially small in n because $\lim_{n \rightarrow \infty} \log_2(M^{1/n}) < 1$.

Similarly, one can estimate the typical value of the absolute minimum $d_{\text{abs min}}$ of a Hamming distance d_{ij} between a pair of marked states

$$\min_{1 \leq i < j \leq M} d_{ij} \sim d_{\text{abs min}}, \quad M^2 2^{-n} \binom{n}{d_{\text{abs min}}} = 1. \quad (57)$$

For $M = 2^{\mu n}$, $\mu = \mathcal{O}(1)$ the minimum distance remains extensive for $\mu < 1/2$ (cf. Eq. (50)). This distance corresponds to the overall largest in magnitude element of the matrix \mathcal{V}_{ij}

$$\max_{1 \leq i < j \leq M} |\mathcal{V}_{ij}| \sim M V_{\text{typ}}. \quad (58)$$

Using (53) the largest element is exponentially small in n provided that $\mu < 1/2$ which corresponds to the condition (50) of statistical independence of the elements of \mathcal{V}_{ij} .

One can use the above estimates of the typical largest matrix elements of the matrix \mathcal{V}_{ij} to consider the bounds on its eigenvalues given by the Gerschgorin circle theorem [45]. For the case of real eigenvalues the theorem states that every eigenvalue lies within at least one of the intervals $[\mathcal{V}_{ii} - R_i, \mathcal{V}_{ii} + R_i]$ where $i \in [1..M]$ and $R_i = \sum_{j \neq i} |\mathcal{V}_{ij}|$ is a sum of absolute values of the off-diagonal elements in the i th row. For a randomly chosen row the value of R_i can be estimated as follows

$$R_i \simeq M \sum_{d=1}^n p_d |V(d)|, \quad (59)$$

where p_d is defined in (49). From Eq. (41) one can see that the above sum is dominated by the terms satisfying $|n/2 - d| \ll n$. Using Stirling's approximation we get $R_i \sim M 2^{-n/2} e^{-n\theta}$. For typical diagonal matrix elements $|\mathcal{V}_{ii}| = |\epsilon_i| \lesssim W$. Therefore from the Gerschgorin theorem we conclude the eigenvalues $E_\beta^{(1)}$ of \mathcal{H} satisfy the following bound

$$|E_\beta^{(1)}| \leq \max \left\{ W, M 2^{-n/2} e^{-n\theta} \right\}. \quad (60)$$

One can see that Gerschgorin bound in our case precisely corresponds to the typical maximum element in the matrix \mathcal{H}_{ij} .

3. Mean value and standard deviation of the off-diagonal matrix elements \mathcal{H}_{ij}

The mean value of the off-diagonal matrix element

$$\langle \mathcal{H}_{ij} \rangle = n \sum_{d=0}^n p_d c(E, d) \simeq \frac{n}{2^n} \frac{B_{\perp}}{B_{\perp} - 1}. \quad (61)$$

is much smaller than its standard deviation

$$\langle (\mathcal{H}_{ij} - \langle \mathcal{H}_{ij} \rangle)^2 \rangle^{1/2} \simeq B_{\perp} \sqrt{\frac{n}{2^n}}. \quad (62)$$

This is related to the symmetry $p_d = p_{n-d}$ and a rapid oscillation of $c(E^{(0)}, d)$ with d (cf. (30), (B11) and Fig. 4).

We note from (53), (62) that the standard deviation is exponentially larger than the typical value

$$\langle (\mathcal{H}_{ij} - \langle \mathcal{H}_{ij} \rangle)^2 \rangle^{1/2} \sim V_{\text{typ}} e^{n\theta}.$$

This can be understood by looking at the values of d_{ij} that dominate the variance of \mathcal{H}_{ij} . We write

$$\langle (\mathcal{H}_{ij})^2 \rangle = n^2 \sum_{d=0}^n c^2(E^{(0)}, d) p_d. \quad (63)$$

It follows from the Eqs. (30) and (49) that for $d \in (n/2 - m_0, n/2 + m_0)$ the coefficient $c^2(E, d) \propto 1/\binom{n}{d}$ decreases exponentially with d , while the distribution $p_d \propto \binom{n}{d}$ increases exponentially with d . The binomial factors cancel out and the expression under the summation in (63) contains very slowly-varying with d (non-oscillatory) part. However for $d \in (0, n/2 - m_0)$ the coefficient $c(E, d)$ grows exponentially faster than $1/\binom{n}{d}$ with decreasing d (see Eqs. (B13), (26)). Therefore the variance (63) is dominated by non-extensive values of $d = \mathcal{O}(n^0)$ that are much smaller than the smallest Hamming distance $d_{\min} = \mathcal{O}(n)$ (54) in a randomly chosen row of d_{ij} . Therefore the variance of \mathcal{H}_{ij} is not a good statistical characteristic of the PDF of \mathcal{H}_{ij} . It is dominated by the extremely rare atypical instances of the ensemble.

B. Heavy tails

We observe that the relationship between the typical matrix element (53), maximum matrix element in a randomly chosen row of \mathcal{V}_{ij} (56), and the largest element of \mathcal{V}_{ij} overall (58) form a strong hierarchy that is a characteristic of the ensemble of dense matrices with broad non-exponential distribution of matrix elements (Levy matrices) [30]. The form of the hierarchy [34] suggests (up to a logarithmic factors) the following asymptotic behavior at the tail of the PDF of the matrix elements:

$$\text{PDF}(\mathcal{V}_{ij}^2) \propto |\mathcal{V}_{ij}|^{-2},$$

for $|\mathcal{V}_{ij}| \gg V_{\text{typ}}$.

We will build on the above observation and obtain the explicit form of the PDF of the matrix elements $P(\mathcal{V}_{ij}^2)$ (52), including its tails. In the asymptotic limit of large $n \gg 1$ we consider n to be a continuous variable (the validity of this approximation will be justified below). We replace the summation over d in (52) by an integral and Kronecker delta $\delta(x)$ by Dirac delta

$$P(\mathcal{V}_{ij}^2) \simeq \int_0^n p_x \delta(V^2(x) - \mathcal{V}_{ij}^2) dx. \quad (64)$$

This expression is obtained using the analytical continuation of the binomial distribution p_d (49) from the integer domain $d \in (0, n)$ onto the interval of a real axis $x \in (0, n)$ in terms of the Beta function and the resulting identity $\int_0^n dx p_x = 1$ (see Appendix D for details).

In what follows we will study the rescaled quantities

$$w_{ij} = \frac{\mathcal{V}_{ij}^2}{V_{\text{typ}}^2} \equiv \frac{V^2(d_{ij})}{V_{\text{typ}}^2}, \quad (65)$$

where $i \neq j$ and V_{typ} is given in (53). We apply Stirling's approximation for the binomial coefficient in Eq. (41) and (49) and obtain asymptotic expressions for $V^2(d)$ and p_d , respectively. Plugging them into the (64) and taking the integral there we can obtain the PDF

$$g(w_{ij}) = V_{\text{typ}}^2 P(V_{\text{typ}}^2 w_{ij}). \quad (66)$$

whose form is given in Appendix, Eqs. (D14), (D15).

The following assumption will be applied throughout the paper

$$\log_2 M \ll n. \quad (67)$$

According to Eqs. (41), (54), (D5) a typical largest element in a randomly chosen row of the matrix w_{ij} is $\sim M$. Therefore based on (67) the following condition is satisfied in a randomly chosen row of w_{ij}

$$\frac{1}{n} \log_2 w_{ij} \ll 1 \quad (1 \leq w_{ij} \lesssim M). \quad (68)$$

Under this condition, the PDF of w_{ij} takes a particularly simple form, $g(w) \simeq g_{\infty}(w)$

$$g_{\infty}(w) = \frac{1}{w^2 \sqrt{\pi \log w}}, \quad w \in (1, \infty), \quad (69)$$

with normalization condition $\int_1^{\infty} g_{\infty}(w) dw = 1$. Details of the derivation are given in Appendix D.

The above analysis assumes the scaling behavior (41) of \mathcal{V}_{ij} with d_{ij} that requires $|n/2 - d_{ij}| < m_0$ with m_0 given in (29). As shown in Appendix D this condition is always satisfied for a typical row of d_{ij} provided the constraint (67) on the values of M .

VI. BORN APPROXIMATION FOR THE TRANSITION RATES

Based on the above discussion, the problem of population transfer is reduced to the analysis of the ensemble of real symmetric $M \times M$ matrices of the dowfolded IB Hamiltonian \mathcal{H} (40). The ensemble is defined over an M -dimensional subset of the computational basis associated with marked states. The non-oscillatory "amplitude" factor \mathcal{V}_{ij} in the expression for the off-diagonal matrix elements of the Hamiltonian (40) obeys the Pareto-like distribution with polynomial tail and typical value V_{typ} (53). An explicit analytical form of the PDF $P(\mathcal{V}_{ij}^2)$ is given in (65),(69). The PDF of diagonal matrix elements $p(\epsilon_i)$ is assumed to be exponentially bounded with some width W . Unlike the ensemble of Levy matrices actively studied in the literature (cf., e.g., [30–32, 34]) the ensembles of matrices \mathcal{H}_{ij} posses a new control parameter: the ratio of typical diagonal to off-diagonal matrix elements W/V_{typ} that controls the preferential basis. The ensemble \mathcal{H}_{ij} is a generalization of the Levi matrix ensemble. The distinction is somewhat similar to that between Gaussian Orthogonal ensemble (GOE) and another Gaussian ensemble with broken $\text{SU}(N)$ symmetry corresponding to a Rosenzweig-Porter (RP) model [38].

Recent studies of RP ensemble [35] found the existence of 2 localization transitions that occur with varying parameter that controls the relative weight of the diagonal and off-diagonal matrix elements. One of them is the Anderson transition from the localized to the extended states that are non-ergodic and posses distinct multifractal features. These states and the corresponding eigenvalues are organized in "minibands" so that the states within the same miniband mostly share the same support over basis states. The spectral width of the minibands is polynomially small (in M) compared to W . The second transition is from the extended non-ergodic states to the extended ergodic states similar to the eigenstates of the Gaussian Orthogonal Ensemble.

In this paper we will focus on exploring the PT transfer within the non-ergodic delocalized phase. We introduce the parametrization similar to the RP case [35]

$$W = \lambda V_{\text{typ}} M^{\gamma/2} \quad (70)$$

where λ is a (redundant) number of order of $\mathcal{O}(M^0)$. In this section we will develop a simple picture relying on Fermi Golden Rule (FGR) to study the rates of population transfer away from a given marked state to a set of other marked states inside the same miniband.

Assume that the system is initially prepared at a randomly chosen marked state $|z_j\rangle$. The probability amplitude to remain in this state equals

$$\psi(z_j, t) = \sum_{\beta} \psi_{\beta}^2(z_j) e^{-iE_{\beta}t}, \quad (71)$$

where $|\psi(t)\rangle$ evolves with the IB Hamiltonian \mathcal{H} (40)

and $\mathcal{H}|\psi_{\beta}\rangle = E_{\beta}|\psi_{\beta}\rangle$. If the eigenstates dominantly coupled to the marked state $|z_j\rangle$ are extended then the amplitude $\psi(z_j, t)$ will undergo decay in time.

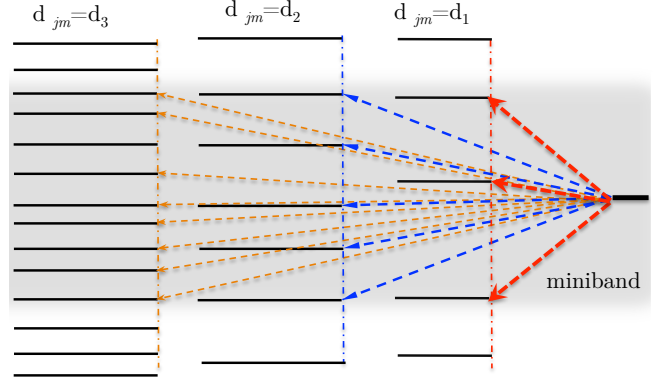


Figure 10. Cartoon of the energies of the marked states ϵ_m within the impurity band. Energy levels are shown with solid black lines forming groups arranged vertically. All states $|z_m\rangle$ within one group lie at the same Hamming distance $d_{jm} = d$ from a given state $|z_j\rangle$ with d increasing from right to left. The energy level ϵ_j is depicted at the right side of the figure with thick black line. Arrows depict the transitions away from the initial state $|\psi(0)\rangle = |z_j\rangle$ into the marked states $|z_m\rangle$ whose energy levels lie inside the miniband of the width Γ_j centered at ϵ_j , i.e., they satisfy the condition $|\epsilon_j - \epsilon_m| \lesssim \Gamma_j$. Miniband width is indicated with the gray shading area. Arrows of the same color depict transitions within one decay channel, connecting the state $|z_j\rangle$ to the states a Hamming distance d away from it. Smaller values of d correspond to bigger typical level spacings $\delta\epsilon_j^d$ (85) and fewer states in a miniband Ω_d (100) within the decay channel given by d .

Here we study this problem within a framework of the Fano-Andreson model for the decay of a discrete state into a continuum [46]. We consider a model Hamiltonian $\tilde{\mathcal{H}}$ that is obtained from the IB Hamiltonian \mathcal{H} (40) by zeroing out all off-diagonal matrix elements except those in the j th column and the j th row connecting state $|z_j\rangle$ to the rest of the marked states. We consider the dynamics on a time scale when the population of the state $|z_j\rangle$ decays into the other states and introduce a small imaginary part $-i\eta$ to their energies. It is assumed to be much bigger than the typical energy spacing, $\eta \gg \delta\epsilon = W/M$ but smaller than the time scale on which the decay takes place.

The Hamiltonian $\tilde{\mathcal{H}}$ has the form

$$\begin{aligned} \tilde{\mathcal{H}} = & \epsilon_j |z_j\rangle \langle z_j| + \sum_{m \neq j} (\epsilon_m - i\eta) |z_m\rangle \langle z_m| \\ & + \sum_{m \neq j} \mathcal{H}_{jm} (|z_j\rangle \langle z_m| + |z_m\rangle \langle z_j|). \end{aligned} \quad (72)$$

where the summation is over $m \in [1..M], m \neq j$.

The amplitude $\psi(t, z_j)$ has a well-known form [46]

$$\psi(z_j, t) = \int_{-\infty}^{\infty} \frac{dz}{\pi} \frac{\Sigma_j''(z) \exp(-izt)}{(z - \Sigma_j'(z) - \epsilon_j)^2 + (\Sigma_j''(z))^2}, \quad (73)$$

where we used a short-hand notation

$$\Sigma_j(z) = \Sigma_j'(z) - i\Sigma_j''(z) \quad (74)$$

for real and imaginary parts of self-energy of the marked state $|z_j\rangle$

$$\Sigma_j(z) = \sum_{m \neq j} \frac{\mathcal{H}_{jm}^2}{z - \epsilon_m + i\eta}, \quad (75)$$

and we keep z real. Calculating the above integral to the leading order in \mathcal{H}_{jm} ($j \neq m$) we get

$$\psi(z_j, t) \simeq \exp \left[-i(\epsilon_j + \Delta\epsilon_j)t - \frac{1}{2}\Gamma_j t \right], \quad (76)$$

where

$$\Delta\epsilon_j \simeq \Sigma_j'(\epsilon_j), \quad \Gamma_j \simeq 2\Sigma_j''(\epsilon_j). \quad (77)$$

The quantity Γ_j above is the decay rate of the state $|z_j\rangle$ which is twice the imaginary part of the self-energy of the state. Expressions (76),(77) correspond to a well-known Born approximation for the decay rate. Using (75) we get

$$\Gamma_j = 2\pi \sum_{m \in [1 \dots M]/j} \mathcal{H}_{mj}^2 \delta(\epsilon_j - \epsilon_m, \eta). \quad (78)$$

where we defined a function

$$\delta(\epsilon, \eta) \equiv \frac{1}{\pi} \frac{\eta}{\epsilon^2 + \eta^2}. \quad (79)$$

The expression for \mathcal{H}_{mj}^2 (cf. (40),(41)) depends in its indices only via the matrix of Hamming distances d_{ij} . Therefore we can break down the decay rate Γ_j into a sum over different decay channels

$$\Gamma_j = \sum_{d=1}^n \Gamma_j^{(d)}, \quad (80)$$

where $\Gamma_j^{(d)}$ corresponds to the transition rate from the initial state $|z_j\rangle$ into the subset of the marked states on a given Hamming distance from $|z_j\rangle$ (see Fig. 10).

$$\Gamma_j^{(d)} = 2\pi V^2(d)(1 - \cos 2\phi(d))\varrho_\eta^j(d), \quad (81)$$

$$\varrho_\eta^j(d) = \sum_{m \neq j} \delta(\epsilon_j - \epsilon_m, \eta) \Delta(d - d_{jm}). \quad (82)$$

Here $\Delta(d)$ is a Kronecker delta and $\delta(\epsilon, \eta)$ is defined in (79). The factor $\varrho_\eta^j(d)$ in (81) is a spectral density of the

marked states located at a distance d from the state $|z_j\rangle$ within the window of energies η around ϵ_j . We denote as $M_j^{(d)}$ the number of marked states that are separated by a Hamming distance d from the state $|z_j\rangle$ (number of terms in the sum (82))

$$M_j^{(d)} = \sum_{m \neq j} \Delta(d - d_{jm}). \quad (83)$$

As discussed in Sec. V A 1 the elements of the set $\{M_j^{(d)}\}_{d=1}^n$ are sampled from the multinomial distribution with mean values

$$\langle M_j^{(d)} \rangle = M p_d, \quad p_d \simeq 2^{-n} \binom{n}{d}, \quad (84)$$

where coefficient p_d defined in (49) is the probability that a randomly chosen state is located on a Hamming distance $d \neq 0$ from $|z_j\rangle$. The mean separation $\delta\epsilon_j^d$ between the adjacent energies ϵ_m in the sum (82) satisfies

$$\delta\epsilon_j^d = \frac{W}{M_j^{(d)}} \sim \delta\epsilon \frac{2^n}{\binom{n}{d}}, \quad (M_j^{(d)} \geq 1), \quad (85)$$

where $\delta\epsilon = W/M$ is mean spacing between the marked state energies. A substantial contribution to the sum in (82) comes from the terms corresponding to the marked states whose energy levels ϵ_j lie within the width η from the energy ϵ_m , i.e., they satisfy the resonant condition $|\epsilon_j - \epsilon_m| \lesssim \eta$ as shown in Fig. 10.

The contribution to a sum from each resonance is $\sim 1/\eta$ and the number of the resonances in a given decay channel is $\Omega_d \sim \eta/\delta\epsilon_j^d$ (cf. Fig. 10). It is shown in the Appendix G that the dominant contribution to Σ_j'' (80) comes from the values of d that correspond to $\Omega_d \gg 1$. For them the function $\delta(\epsilon_j - \epsilon_m, \eta)$ in Eq. (82) changes weakly between the adjacent values of ϵ_m and we estimate the sum over m in (82) by replacing it with an integral. The error induced by such approximation will be discussed below. Then the spectral density can be estimated as $\varrho_\eta^j(d) \sim 1/\delta\epsilon_j^d$ or, more precisely

$$\varrho_\eta^j(d) = \begin{cases} \frac{\chi(\epsilon_j/W, \eta/W)}{\delta\epsilon_j^d} & M_j^{(d)} \geq 1 \\ 0 & M_j^{(d)} = 0 \end{cases}. \quad (86)$$

where $\chi(x, y)$ explicitly depends on the form of the energy PDF ²

$$\chi(x, y) = \int_{-\infty}^{\infty} du p_A(u) \delta(u - x, y). \quad (87)$$

We plug (86) into the expression (81) for $\Gamma_j^{(d)}$ and then

²In case of step-function PDF, $p_A(u) = \theta(1/2 - |u|)$, we have $\chi(x, y) = \frac{1}{\pi} \sum_{s=\pm 1} \arctan \left(\frac{1/2 - sy}{x} \right)$.

plug the result into (80), obtaining the following relation

$$\Gamma_j = 2\pi \frac{\chi_j}{W} \sum_{d=1}^n M_j^{(d)} V^2(d) (1 - \cos 2\phi(d)) \quad (88)$$

$$= 2\pi \frac{\chi_j}{W} \sum_{m \neq j} V^2(d_{jm}) (1 - \cos 2\phi(d_{jm})) . \quad (89)$$

where we for brevity used $\chi_j \equiv \chi(\epsilon_j/W, \eta/W)$.

The sum in the first line above is dominated by values of d where $M_j^{(d)} \gg 1$ (see Appendix G). We write $M_j^{(d)} = \langle M_j^{(d)} \rangle + \delta M_j^{(d)}$ and obtain using the expression (41) for $V(d)$ that

$$V^2(d) \langle M_j^{(d)} \rangle \simeq A(d/n) n^{5/2} e^{-2n\theta} M 2^{-n}$$

Because $A(\rho)$ is a smooth function of ρ the above quantity changes only by $\mathcal{O}(n^{-1})$ when d changed by 1.

The term involving $\cos 2\phi(d)$ above oscillates around 0 on the scale $d \sim 1$ (cf. Eq. (32)). Therefore the contributions to the sum from the terms $\propto \bar{M}_j^{(d)} \cos 2\phi(d)$ average out. We will neglect the cross-product of fluctuational and oscillatory parts $\delta M_j^{(d)} \cos 2\phi(d)$ and drop the second term in the r.h.s of (89) that contains $\cos 2\phi(d)$. Essentially, this approximation corresponds to replacing the oscillatory part in the expression for the off-diagonal matrix elements $\mathcal{H}_{ij \neq i} = V(d_{ij}) \sqrt{2} \sin \phi(d_{ij})$ (40) as follows:

$$\mathcal{H}_{ij} \rightarrow V(d_{ij}) \beta_{ij}, \quad \beta_{ij} = \pm 1, \quad i < j, \quad (90)$$

where β_{ij} are instances of a dichotomous random variable that takes values ± 1 with probability 1/2.

Using the above approximation in the sum (89) and also Eqs. (65), (41), (53), we obtain the relation between the PDFs of the random variables

$$\Gamma = 2\Sigma'' \stackrel{d}{=} 2\pi \frac{V_{\text{typ}}^2 M}{W} s_M \chi(\epsilon/W, \eta/W), \quad (91)$$

$$s_M = \frac{1}{M} \sum_{m=1}^M w_m. \quad (92)$$

Here w_m are random variables independently sampled from the probability distribution $g_\infty(w)$ given in (69). Decay rates $\Gamma_j \equiv 2\Sigma_j''$ and energies ϵ_j of marked states for $1 \leq j \leq M$ are samples of random variables $\Gamma \equiv 2\Sigma''$ and ϵ , respectively. Eq. (91) relates the PDFs of Γ (Σ'') and ϵ to that of s_M while η, W, M are the parameters in that relation.

The above analysis required that the level width η initially introduced in the effective model (72) is much bigger than the individual level spacing. Now we will also require that η is much smaller than the total width of the impurity band,

$$\delta\epsilon \ll \eta \ll W. \quad (93)$$

In this case the second argument of the function $\chi(x, y)$ in (91) is very small and Eq. (87) takes the form

$$\lim_{y \rightarrow 0} \chi(x, y) = p_A(x) \quad (94)$$

(in this limit $\delta(u, y)$ (87) approaches the Dirac delta function). Then η drops out from Eq. (91) and one gets

$$\Gamma = 2\Sigma'' \stackrel{d}{=} 2\Sigma''_* s_M, \quad \Sigma''_* = \pi \frac{V_{\text{typ}}^2}{W/M}, \quad (95)$$

where we introduced for future purposes the characteristic value of the imaginary part of self-energy Σ''_* . The resulting expression for the decay rate of a marked state Γ formally corresponds to that given by FGR for the decay of the discrete level into the continuum [46]. The energies of the marked states into which a given marked state decays lie within the same miniband. The decay occurs simultaneously in many channels corresponding to different Hamming distances between the initial marked state and the states of the miniband. Random variable s_M describes the properties of the neighborhood of the marked state characterized by the random set of Hamming distances separating the state from other states satisfying the resonant condition.

With Eq. (95) the PDF of $\Gamma = 2\Sigma''$ is expressed entirely in terms of the PDF of a random variable s_M studied in details in Appendix F. Using Generalized Central Limit Theorem (GCLT) for the sums of a large number of identical heavy-tailed random variables [30, 40] it can be represented in the form

$$s_M \stackrel{d}{=} \sigma_M x + b_M \quad (96)$$

where x obeys a so-called Levy alpha-stable distribution $L_1^{1,1}(x)$ [30] defined in the Appendix, Eq. (F8), and shown in Fig. 11. Scaling factor and shift are

$$\sigma_M = \sqrt{\frac{\pi}{4 \log M}}, \quad (97)$$

$$b_M \simeq \sigma_M^{-1} - \frac{2}{\pi} \sigma_M \log(\sigma_M^{-1}) + \frac{2}{\pi} (1 - \gamma_{\text{Euler}}) \sigma_M, \quad (98)$$

($\gamma_{\text{Euler}} \simeq 0.577$ is the Euler constant). They display very weak logarithmic dependence on M as compared with the main factor $\propto V_{\text{typ}}^2/\delta\epsilon$ in (95). The width of the PDF of s_M is shrunk by a factor $(\log M)^{1/2} \gg 1$ and the location of its maximum is increased by a factor $(\log M)^{1/2} \gg 1$ compared to $L_1^{1,1}(x)$.

The PDF of s_M has polynomial tail. Therefore decay rates of marked states $\Gamma_j = 2\Sigma_j''$ can take a range values that are much bigger than their typical values $2\Sigma''_*$ (95), up to M times bigger in the sample of the size M . These atypically large decay rates correspond to rare clusters of marked states that are located anomalously close to each other. When clusters are formed by $\mathcal{O}(1)$ states the above picture of the decay fails.

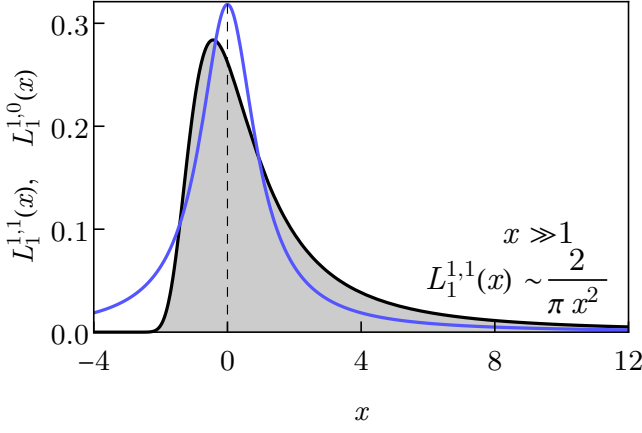


Figure 11. Black solid line shows the plot of the Levy alpha-stable distribution $L_{\alpha}^{C,\beta}(x)$ [30] with tail index $\alpha = 1$, asymmetry parameter $\beta = 1$ and unit scale parameter $C = 1$. Inset shows asymptotic behavior of the distribution at large positive x . At $-x \gg 1$ the function decays steeply as a double exponential, $\log L_1^{1,1}(x) \propto -\exp(-\frac{\pi}{2}x)$. Blue line shows the Cauchy distribution $L_1^{1,0}(x) = \frac{1}{\pi(1+x^2)}$. We follow here the definition introduced in [30] and used in subsequent papers on Levi matrices in physics literature. In mathematical literature [47, 48] a different definition is usually used, corresponding to $f(x; \alpha, \beta, C^{1/\alpha}, 0) = L_{\alpha}^{C,\beta}(x)$.

A. Number of states in a miniband

Using the expression (95) for the decay rate we can estimate the number of marked states Ω in a miniband corresponding to a given state $|z_j\rangle$. As before, we divide the states into the groups of the sizes Ω_d , each corresponding to the transitions with a fixed number of flipped bits d . Based on (93) set $\chi(\epsilon/W, \eta/W) = 1$ in the r.h.s. of Eq. (91). Then, using (41), (85) and replacing $M_j^{(d)}$ with its average value (84) we obtain the estimate for the rate $\Gamma_j^{(d)}$ (81) of transition away from the state $|z_j\rangle$ with flipping d bits

$$\Gamma_j^{(d)} \simeq 2\pi \frac{V_{\text{typ}}^2}{\delta\epsilon} \frac{1}{\sqrt{\pi n/2}} \frac{M_j^{(d)}}{\langle M_j^{(d)} \rangle}. \quad (99)$$

We note that the typical values of $M_j^{(d)}/\langle M_j^{(d)} \rangle \sim 1$ in (99) and therefore typical values of $\Gamma_j^{(d)}$ do not depend on d .

The estimate for the typical number of states in the miniband at the distance d from $|z_j\rangle$ is $\Omega_d \sim \Gamma_j/\delta\epsilon_j^d$. Then we get

$$\Omega_d \sim \Omega p_d, \quad \Omega \sim \frac{\Gamma_j}{\delta\epsilon} \sim \left(\frac{V_{\text{typ}}}{\delta\epsilon} \right)^2, \quad (100)$$

where $p_d = 2^{-n} \binom{n}{d}$ and Ω is the total number of states in the miniband.

We observe an interesting effect. While the typical

number of marked states in a decay channel varies very steeply with d , typical values of decay rates $\Gamma_j^{(d)}$ in different channels (99) do not depend on d . To understand this we note from Eqs. (81), (88), that $\Gamma_j^{(d)} \propto V^2(d) M_j^{(d)}/W$. The squared transition matrix element in a given channel rapidly decreases with Hamming distance, $V^2(d) \propto 1/\binom{n}{d}$. However this decrease is compensated by the rapid growth with d of the density of state $M_d/W \propto \binom{n}{d}$ (100) at a distance d . The binomial factors cancel out and $\Gamma_j^{(d)}$ is d -independent, except for the prefactor slow varying with d on a scale $d \sim n$.

One can also write the partial decay rate as $\Gamma_j^{(d)} \sim V(d)\Omega_d$ where the product $V(d)\Omega_d$ does not depend on d (except from the prefactor). Of course, the analysis based on the decay rate does not apply for the transition to the channels with very few states. The condition $\Omega_d \simeq 1$ leads to $\Gamma_j^{(d)} \sim V(d)$ for $d = d_{\text{min}}^{\text{res}}$ corresponding to the typical Hamming distance from $|z_j\rangle$ to the nearest marked state in a miniband where the condition $V(d) \simeq \delta\epsilon_j^d$ is satisfied (see Eq. (G1) in Appendix).

The above estimate gives the correct time scale $\sim 1/V(d_{\text{min}}^{\text{res}})$ over which the two states become hybridized. We note however that the total number of channels is $n - 2d_{\text{min}}^{\text{res}} = \mathcal{O}(n)$. As all $\Gamma_j^{(d)}$ are nearly the same, each channel contributes a small fraction $\mathcal{O}(1/n)$ to the total rate. Therefore $V(d_{\text{min}}^{\text{res}}) \sim \Gamma_j/n$ and marked state $|z_j\rangle$ decays into the large number of marked states within a miniband before it has a chance to hybridize with the nearest one at a distance $d_{\text{min}}^{\text{res}}$. This property is markedly different from the situation at finite dimension [22].

Using the scaling ansatz (70) we estimate the mean separation between the energies of marked states as

$$\delta\epsilon = \frac{W}{M} = \lambda V_{\text{typ}} M^{\gamma/2-1}. \quad (101)$$

Using the Eqs. (95) and (100) we obtain the estimates for typical values of the decay rates and number of marked states in a miniband

$$\Gamma = 2\Sigma'' \sim V_{\text{typ}} M^{1-\gamma/2}, \quad \Omega \sim M^{2-\gamma}. \quad (102)$$

We immediately observe that in the range of $\gamma > 2$ the number of marked states in a miniband vanishes. It corresponds to a localized phase, consistent with the fact that typical energy spacing δ becomes greater than the typical tunneling matrix element V_{typ} connecting the states. The number of states in a miniband Ω cannot be greater than the total number of states M in the IB. The expression above does not apply for $\gamma \leq 1$. This regime corresponds to ergodic phase.

In the region $2 > \gamma > 1$ the separation between adjacent eigenvalues of \mathcal{H} is of the same order as $\delta\epsilon$. The typical number of marked states in a miniband Ω corresponds to the typical number of non-ergodic delocalized

eigenstates of \mathcal{H} that form the miniband.

$$W \gg \Gamma \gg \delta\epsilon = \frac{W}{M}. \quad (103)$$

The number of states in a miniband scales as a fractional power of M less than one. This is a hallmark of non-ergodic delocalized phase.

VII. CAVITY METHOD: SUMMARY OF THE PREVIOUS RESULTS

The cavity method has been actively used to study Anderson Localization in Levy matrices in the last several decades [30–34, 39, 49] starting from the seminal work [30]. In the present work we use cavity method to study the properties of minibands of delocalized non-ergodic states that were previously discovered in the studies of Rosenzweig-Porter [33, 35] and Regular Random Graph (RRG) [36, 37] models. Initial studies suggested the existence of the mixed region with localized but non-ergodic states [30]. However, recent numerical studies based on exact diagonalization using very large number of samples established that initially large crossover region between localized and extended states collapses in the limit of increasing matrix sizes [32]. Multifractal properties of eigenstates in the localized phase and at criticality were studied in [34] using strong disorder perturbation theory.

Numerical solution of cavity equations to study localization transition in Levi matrices with power-law distributions $P(\mathcal{H}_{ij}^2) \propto 1/\mathcal{H}_{ij}^{2(\alpha+1)}$ were obtained using population dynamics algorithm [31] utilizing the approach developed in [49]. An alternative approach is based on the integral equation for the PDF of the diagonal elements of the resolvent [30, 39]. It was obtained in the limit where imaginary part of the self-energy is vanishingly small [30, 32, 39] (with the limit of infinite matrix size taken first). This allows one to derive analytically the global density of states [30, 39] and the mobility edge $E^*(\alpha)$ which gives the α -dependence of the energy E^* separating extended and localized eigenvalues of \mathcal{H} [32].

The cavity method proceeds as follows. First, we generate a random $M \times M$ matrix \mathcal{H}_{ij} (40) from the ensemble described in Sec. V. Then we add a new row (and a symmetric column) of independent numbers identically distributed as those in the old matrix \mathcal{H}_{ij} . This is done by generating a random energy ϵ_0 from the distribution $\frac{1}{W}p_A(\epsilon/W)$; then generating a random bit-string z_0 , computing the array of Hamming distances d_{j0} between z_0 and z_j and the corresponding matrix elements $\mathcal{H}_{j0} = \mathcal{H}_{0j}$ for integer $j \in [1, M]$. As a result we obtain a new $(M+1) \times (M+1)$ matrix \mathcal{H}^{+1} , where +1 emphasizes that it has one more row and one more column than \mathcal{H} . We will number elements of the new matrix by indices running over the range $[0, M]$ where the index 0 corresponds to the added marked state $|z_0\rangle$. The cavity

equations have the form [30, 39]

$$\Sigma_0^{+1}(z) = \sum_{m=1}^M \mathcal{H}_{0m}^2 G_{mm}(z),$$

where

$$G_{mm}(z) = (z - \epsilon_m - \Sigma_m)^{-1}.$$

It does not involve the non-diagonal matrix elements of the Green's function $G_{mm'}(z)$ when statistical average $\langle \mathcal{H}_{0m} \rangle = 0$. This is effectively our case as well (see Eq.(61)).

The main assumption of cavity method is that in the limit $M \rightarrow \infty$ the difference between the PDFs of $\Sigma_0^{+1}(z)$ and $\Sigma_0(z)$ disappears. This results in a self-consistent equations for the self-energy. Following [29] we add small imaginary parts to the diagonal matrix elements $\mathcal{H}_{mm} = \epsilon_m - i\eta$. It is a small “fictitious” quantity that is still assumed to be much bigger than the marked state energy spacing $\eta \gg W/M$. Results are not expected to depend on the value of η provided its scaling with M is chosen appropriately, as will be discussed below. We separate the real and imaginary parts of the self-energy, $\Sigma_m(z) = \Sigma'_m(z) - i\Sigma''_m(z)$ (cf. (74)), obtaining

$$\Sigma'_0 \doteq \pi \sum_{m=1}^M \mathcal{H}_{0m}^2 \delta(\Sigma''_m + \eta, z - \epsilon_m - \Sigma'_m), \quad (104a)$$

$$\Sigma''_0 \doteq \pi \sum_{m=1}^M \mathcal{H}_{0m}^2 \delta(z - \epsilon_m - \Sigma'_m, \Sigma''_m + \eta). \quad (104b)$$

where the function $\delta(x, y) \equiv \frac{1}{\pi} \frac{y}{x^2 + y^2}$ was already introduced in (79).

The self-consistent Eqs. (104) were derived by Abou-Chacra, Anderson and Thouless [29] for matrices on Bethe lattices and by Bouchaud and Cizeau for Levy matrices [30]. The solution of these equation was only found in the case when they can be linearized in Σ''_m [29, 30, 32] giving the location of mobility edge $E^*(\alpha)$ as a function of the power α in the tail of the PDF of the matrix elements $P(\mathcal{H}_{ij}^2) \propto 1/\mathcal{H}_{ij}^{2(\alpha+1)}$. Here we will provide a full solution of the nonlinear equations.

We will solve the self-consistent equations (104) under the assumption that pairs of variables (Σ'_m, Σ''_m) for each state $m \in [0, M]$ are taken from the *same* PDF $\mathcal{P}(\Sigma', \Sigma''; z)$ defined over the domain $x \in (-\infty, \infty)$, $y \in [0, \infty)$. In what following for brevity we omit the explicit dependence on the parameter z . Following [29] we introduce the characteristic function $\mathcal{F}(k_1, k_2)$ of the PDF $\mathcal{P}(\Sigma', \Sigma'')$

$$\mathcal{F}(k_1, k_2) = \int_{-\infty}^{\infty} d\Sigma' \int_0^{\infty} d\Sigma'' \mathcal{P}(\Sigma', \Sigma'') e^{ik_1 \Sigma' + ik_2 \Sigma''},$$

that satisfies the equation $\mathcal{F}_\eta(k_1, k_2) = \mathcal{G}_\eta^M(k_1, k_2)$ where

$$\mathcal{G}(k_1, k_2) = \langle e^{ifk_1 \delta(\eta + \Sigma'', z - \epsilon - \Sigma') + ifk_2 \delta(z - \epsilon - \Sigma', \eta + \Sigma'')} \rangle$$

Here $f = \mathcal{H}_{0m}^2$ and the average is performed with the joint PDF $\mathcal{P}(\Sigma', \Sigma'') \frac{1}{W} p_A(\frac{\epsilon}{W}) df P(f)$. The above relation between $\mathcal{F}(k_1, k_2)$ and $\mathcal{G}(k_1, k_2)$ is actually an equation for the PDF $\mathcal{P}(\Sigma', \Sigma'')$ because both \mathcal{G} and \mathcal{F} depend on \mathcal{P} .

VIII. SOLUTION OF CAVITY EQUATIONS IN NON-ERGODIC DELOCALIZED PHASE

A. Analysis of the imaginary part of self-energy

We note that the exponent in the integrand of the above expression for \mathcal{G} depends on Σ' and $\epsilon - z$ only via their combination $\Sigma' + \epsilon - z$. In the non-ergodic delocalized phase the typical width of the PDF of Σ' is much more narrow than the width W of $p(\epsilon)$ (46). We will also consider small values of $|z| \ll W$. Therefore in the first approximation we will neglect Σ' and z compared to ϵ . Then $\mathcal{G}(k_1, k_2)$ depends only on the marginalized PDF

$$\mathcal{P}(\Sigma'') = \int_{-\infty}^{\infty} d\Sigma' \mathcal{P}(\Sigma', \Sigma''). \quad (105)$$

Once this PDF is obtained, the PDF $\mathcal{P}(\Sigma', \Sigma'')$ can be analyzed from its characteristic function $\mathcal{F}(0, k_2)$. Inverting it we obtain the self-consistent equation for $\mathcal{P}(\Sigma'')$ in the limit $M \rightarrow \infty$

$$\mathcal{P}(\Sigma'') = \frac{1}{2\pi} \int_{-\infty}^{\infty} dk e^{M\theta(k) - ik\Sigma''}. \quad (106)$$

$$\theta(k) = \int_0^{\infty} df d\Sigma'' dh P(f) \mathcal{P}(\Sigma'') p_{\eta + \Sigma''}(h) (e^{ikfh} - 1)$$

Here $\theta(k) = 1 - \mathcal{G}_\eta(0, k)$ and the domain of integration for all variables is $[0, \infty)$. The function $p_{\eta + Y}(h)$ above is a conditional PDF of a random variable

$$h = \delta(\epsilon, \eta + Y)$$

with Y fixed and $\delta(x, y)$ given in (79). The explicit form of the PDF $p_{\eta + Y}(h)$ is obtained in Sec. H of the Appendix, Eqs. (H6), (H8).

To achieve further progress we use the approximation (90) and drop oscillatory factors in the off-diagonal matrix elements \mathcal{H}_{0m} . Then we have for the PDF $P(f) = g_\infty(f/V_{\text{typ}}^2)/V_{\text{typ}}^2$ (69) and in what follows we will use the rescaled variable $w = f/V_{\text{typ}}^2$ for the squared matrix elements, in accordance with (65). Instead of the variable h in (106) we will use the re-scaled variable

$$y = \sqrt{h(\eta + \Sigma'')}, \quad (107)$$

that obeys the distribution

$$p_{\eta + \Sigma''}(y) = \frac{2(\eta + \Sigma'')}{W} \frac{1}{y^2 \sqrt{1 - y^2}} \quad (108)$$

(see details in Appendix H, (H19)). Then $\theta(k)$ takes the form

$$\theta(k) = \int_0^{\infty} d\Sigma'' \mathcal{P}(\Sigma'') \phi_{\Sigma'' + \eta} \left(\frac{k V_{\text{typ}}^2}{\Sigma'' + \eta} \right). \quad (109)$$

Here $\phi_Y(u)$ is a characteristic function

$$\phi_Y(u) = \int_0^{\infty} dx g_Y(x) (e^{iux} - 1). \quad (110)$$

of the PDF $g_Y(x)$ of the random variable $x = wy^2$ where w obeys $g_\infty(w)$ and y obeys $p_Y(y)$ (108). Detailed study of $g_Y(x)$ is given in Appendix I. The PDF $g_Y(x)$ depends on Y via the ratio Y/W and its plot is shown in Fig. 12. It goes over into $g_\infty(y)$ for $Y \rightarrow \infty$.

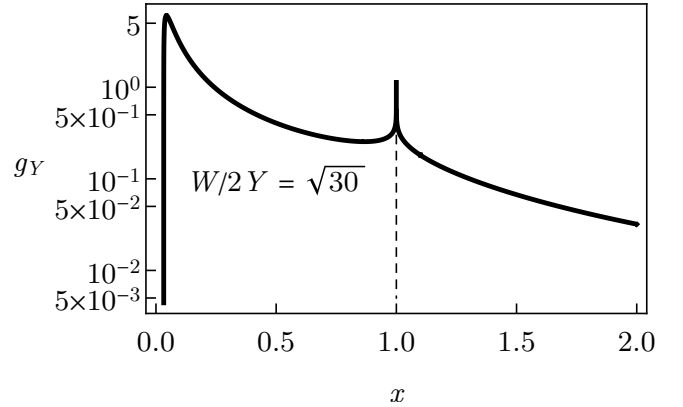


Figure 12. Plot of the PDF $g_Y(x)$ of the random variable $x = \frac{wY^2}{(z-\epsilon)^2 + Y^2}$ where random variables ϵ and w obey distributions $W^{-1}p_A(\epsilon/W)$ and $g_\infty(w)$, respectively, and $W/(2Y) = \sqrt{30}$. Detailed discussion of $g_Y(x)$ is given in Appendix I (see Eq. (I7)). Its maximum is located at $x \sim (Y/W)^2$. The singularity at $x = 1$ corresponds to $\epsilon = z$. For large values of $x \gg 1$ the conditional PDF of $\frac{Y^2}{(z-\epsilon)^2 + Y^2}$ is narrowly peaked around its mean value $\pi Y/W$ with $|\epsilon - z| \sim Y$, giving rise to the relation in Eq. (111).

We now make a key observation: in the limit of large $x \gg 1$ and for $W \gg Y$ the following relations holds for the PDF $\phi_Y(u)$ and its characteristic function (see the corresponding Eqs. (I26) and (I10) in Appendix I)

$$g_Y(x) \simeq \frac{\pi Y}{W} g_\infty(x), \quad \phi_Y(u) \simeq \frac{\pi Y}{W} \phi_\infty(u). \quad (111)$$

The reason for this can be explained as follows. For large deviations of $x = wY^2/(\epsilon^2 + Y^2)$ the conditional PDF $p(\epsilon|x)$ of the marked state energy ϵ is narrowly peaked in the range of values $|\epsilon| \sim Y$. In contrast, typical energy

values are much bigger $\epsilon \sim W$. This narrowing of the conditional PDF $p(\epsilon|x)$ gives rise to a small factor $\pi Y/W$ in the r.h.s. of (111).

We observe that $\lim_{k \rightarrow \infty} \theta(k) = 0$ and for $M \rightarrow \infty$ the integral in (106) is dominated by $|k| \ll 1$. We make an assumption (whose validity becomes obvious below) that for small enough k the integral in (109) is dominated by values of Σ'' such that $kV_{\text{typ}}^2/(\Sigma'' + \eta) \ll 1$. Therefore we will use in (109) the approximate expression for the characteristic function $\phi_{\Sigma''+\eta}$ given by Eq. (111). We rescale Σ'' with the typical value of imaginary part of self-energy of marked states Σ''_* (95) obtained in FGR-based calculation in Sec. VI. Making a change of variables

$$\Sigma'' = \Sigma''_* s, \quad \mathcal{P}(\Sigma'') = \frac{1}{\Sigma''_*} \rho(s), \quad (112)$$

we rewrite the self-consistent equation (106) in the limit $x \gg 1, W \gg Y$ for the rescaled PDF $\rho(s)$ in the following form:

$$\rho(s) = \frac{1}{2\pi} \int_{-\infty}^{\infty} du e^{-ius + \Phi(u, \Omega)}, \quad (113)$$

$$\Phi(u, \Omega) = \int_{-\infty}^{\infty} d\nu \rho(\nu - \beta_\eta) \Omega \nu \phi_\infty\left(\frac{q}{\Omega \nu}\right),$$

$$\beta_\eta = \frac{\eta}{\Sigma''_*}, \quad (114)$$

and

$$\Omega = \frac{\pi \Sigma''_*}{\delta \epsilon} = \left(\frac{\pi V_{\text{typ}}}{W/M} \right)^2, \quad (115)$$

Σ''_* and V_{typ} are defined in (95) and (53), respectively. We observe that Ω corresponds to the typical number of marked states in the mini-band that we estimated in Sec. VI using the Born approximation.

Assuming $\Omega \gg 1$ (delocalized phase) we expand $\Omega \nu \phi_\infty(q/(\Omega \nu))$ in inverse powers of $\log \Omega$ using asymptotic form of the characteristic function $\phi_\infty(u)$ at small argument studied in Appendix E, Eqs. ((E13)), (E14). Truncating the expansion at terms $\sim (\log M)^{-1/2}$ we get

$$\Omega \text{Re} \phi_\infty\left(\frac{q}{\Omega}\right) \simeq -\frac{\pi |q|}{2\sqrt{\log \Omega}}, \quad (116)$$

$$\Omega \text{Im} \phi_\infty\left(\frac{q}{\Omega}\right) \simeq 2q \left(\frac{\log \Omega}{\pi} \right)^{1/2} + q \frac{1 - \mathcal{C} - \log |q|}{(\pi \log \Omega)^{1/2}},$$

where $\mathcal{C} \approx 0.577$ is the Euler constant. It is clear from comparing individual terms in Eq. (116) with the exponential in Eq. (113) that $q = \mathcal{O}(\sqrt{\log \Omega})$. This justifies the order of truncation (see details in Appendix F, Eq. F5).

We make change of variables in the integral in (113) $q = 2\sqrt{\log \Omega}/\pi t$ and obtain

$$\rho(s) = \sigma_\Omega^{-1} L_1^{1,1}((s - \mu_\Omega)/\sigma_\Omega), \quad (117)$$

where quantity μ_Ω satisfies the equation

$$\mu_\Omega = b_\Omega + \frac{2\sigma_\Omega}{\pi} \int_{-\infty}^{\infty} ds \rho(s) \log |s + \beta_\eta|. \quad (118)$$

Above $L_1^{1,1}(x)$ is Levy distribution [30] defined in the Appendix, Eq. (F8), and shown in Fig. 11. Coefficients $\sigma_\Omega = \sqrt{\pi/(4 \log \Omega)}$ and $b_\Omega \simeq 1/\sigma_\Omega$ are given in Eqs. (97), (98) where the parameter M needs to be replaced by Ω .

We plug the above expression for $\rho(s)$ into (118) and express μ_Ω in terms of a new variable x

$$\mu_\Omega \equiv b_\Omega - \frac{2\sigma_\Omega}{\pi} \log \sigma_\Omega^{-1} + \sigma_\Omega x. \quad (119)$$

Then this variable satisfies the following equation

$$x = \frac{2}{\pi} \int_{-\infty}^{\infty} ds L_1^{1,1}(s) \log |s + x + \zeta_\Omega|, \quad (120)$$

that involves a scale-free Levy distribution and a single parameter ζ_Ω

$$\zeta_\Omega = \frac{b_\Omega}{\sigma_\Omega} - \frac{2}{\pi} \log \left(\frac{1}{\sigma_\Omega} \right) + \frac{1}{\sigma_\Omega} \frac{\eta}{\Sigma''_*} \quad (121)$$

where we used an explicit form of β_η (114). We note that the self-consistent equation for the function $\rho(s)$ is now reduced to the simple transcendental equation (120).

Using explicit form of σ_Ω and b_Ω (97), (98) one can see that ζ_Ω is large compared to unity in the delocalized phase, $\zeta_\Omega \simeq \sigma_\Omega^{-2} \sim \log \Omega \gg 1$. With this property the equation for x (120) can be solved by iteration using the asymptotic expansion of Levy distribution at large arguments, $L_1^{1,1}(\nu) \simeq (2/\pi)\nu^{-2}$ ($\nu \gg 1$). To the leading order

$$x \simeq \frac{2}{\pi} \log \zeta_\Omega + \mathcal{O}\left(\frac{\log \zeta_\Omega}{\zeta_\Omega}\right). \quad (122)$$

Then using (119) the expression for μ_Ω is

$$\mu_\Omega \simeq \frac{1}{\sigma_\Omega} + \frac{2\sigma_\Omega}{\pi} \log \left(1 + \frac{\eta \sigma_\Omega}{\Sigma''_*} \right) + \frac{2\sigma_\Omega(1 - \gamma_{\text{Euler}})}{\pi} \quad (123)$$

where we neglected terms $\sim \sigma_\Omega^3 \log \Omega$ that are much smaller than the width σ_Ω of the distribution $\rho(s) = \sigma_\Omega^{-1} L_1^{1,1}((s - \mu_\Omega)/\sigma_\Omega)$.

We note that the dependence of μ_Ω (123) on the initial (fictitious) level broadening η disappears when the later is chosen to be much smaller than the mini-band width [33, 36, 37], $W/M \ll \eta \ll \Sigma''_* \sigma_\Omega$. Using (95), (70) the scaling behavior of η with M in the non-ergodic delocalized regime must satisfy the condition

$$\eta = M^\kappa, \quad |\kappa| < 1 - \frac{\gamma}{2}, \quad \gamma \in (1, 2). \quad (124)$$

Finally the expression for the distribution function of

the imaginary part of self-energy has the form

$$\mathcal{P}(\Sigma'') = \frac{1}{C} L_1^{1,1} \left(\frac{\Sigma'' - \Sigma''_{\text{typ}}}{C} \right), \quad (125)$$

$$\Sigma''_{\text{typ}} = \mu_\Omega \Sigma''_*, \quad C = \sigma_\Omega \Sigma''_*. \quad (126)$$

Here Σ''_{typ} is a shift of the distribution and C its scale parameter (characteristic width). Also,

$$\mu_\Omega \simeq \frac{1}{\sigma_\Omega} + \frac{2\sigma_\Omega(1 - \gamma_{\text{Euler}})}{\pi}. \quad (127)$$

$$\sigma_\Omega = \sqrt{\frac{\pi}{4 \log \Omega}}. \quad (128)$$

Using the scaling ansatz (70) for the width W of the IB in terms of M , the typical number of states in a mini-band (number of resonances) equals,

$$\Omega = \left(\frac{\pi}{\lambda} \right)^2 M^{2-\gamma}. \quad (129)$$

Using the same scaling ansatz (70) and the expressions for σ_Ω (97) and μ_Ω (127) we obtain,

$$\Sigma''_{\text{typ}} \simeq \frac{2\pi^{1/2}}{\lambda} V_{\text{typ}} M^{1-\gamma/2} (\log \Omega)^{1/2}, \quad (130)$$

$$C \simeq \frac{\pi^{3/2}}{2\lambda} V_{\text{typ}} M^{1-\gamma/2} (\log \Omega)^{-1/2}. \quad (131)$$

Here $V_{\text{typ}} \sim n^{1/2} 2^{-n/2} e^{-n/(4B_\perp^2)}$ is given in (53). The shift Σ''_{typ} corresponds to the typical value of Σ'' . One can see from the above that it is $\log \Omega \sim \log M \gg 1$ times bigger than the distribution width. We note in passing that distribution of Σ'' determines that of the miniband width $\Gamma = 2\Sigma''$ (102).

1. Comparison between the cavity method and Born approximation

It is instructive to compare the above distribution of Σ'' obtained using the cavity method with that obtained within the Born approximation (95)-(98). In both cases the distribution of Σ'' is given by the appropriately rescaled and shifted Levy alpha-stable distribution $L_1^{1,1}(x)$. In both cases, the scale parameter C (characteristic width) of the distribution has the form $C = \sigma_S \Sigma''_*$ with $\sigma_S = \sqrt{\pi/(4 \log S)}$. In the case of the Born approximation $S = M$, corresponding to the total number of marked states, and in the case of cavity method $S = \Omega \ll M$, corresponding to the (much smaller) number of states in the mini-band. Using (129) we estimate

$$\frac{\sigma_M}{\sigma_\Omega} = \sqrt{2 - \gamma} < 1 \quad (W = \lambda M^{\gamma/2}). \quad (132)$$

Therefore Born approximation underestimates the width of the distribution of Σ'' . The ratio (132) is especially pronounced near the localization transition $\gamma = 2$. Value of σ_Ω^{-1} shrinks to zero at the transition while that of σ_M does not depend on the closeness to the transition point.

We note however that factors σ_Ω and σ_M depend on M only logarithmically. At the same time, the leading order (power-law) dependence of the rescaling coefficient on M is given by the factor $\Sigma''_* \propto M^{1-\gamma/2}$, and is identical in the cavity method and the Born approximation-based expressions.

The situation is similar with the shift parameter Σ''_{typ} in the Levy distribution of Σ'' corresponding its typical value, $\Sigma''_{\text{typ}} \simeq \Sigma''_*/\sigma_S$ with $S=M$ (Born approximation) and $S=\Omega$ (cavity method). The leading-order dependence of the shift on M is the same in both cases and is given by Σ''_* . In both cases the shift is greater than the rescaling coefficient by a factor $\sim \log M$. However the Born approximation overestimates the shift by a factor $(2 - \gamma)^{-1/2}$.

2. Comparison between the cavity method and self-consistent Born approximation

The Born approximation recovers the typical shift Σ''_{typ} and the scale parameter C of the distribution of Σ'' with exponential accuracy in $\log M$. However it gives an incorrect dependence of the prefactor on $\log M$ in these coefficients. The key approximation in Sec. VI was to assume that the partial sum in the expressions (81),(82) for the decay rate $\Gamma_j^{(d)}$ can be replaced by an integral over energies of the marked states located on the same Hamming distance d from the state $|z_j\rangle$. We revisit the decay rate equation (78), and removing the oscillatory parts in the matrix elements (90) we write

$$\Sigma'' = \frac{V_{\text{typ}}^2}{\eta} \sum_{m=1}^M x_m, \quad x_m = \frac{w_m \eta^2}{\epsilon_m^2 + \eta^2}. \quad (133)$$

Here in the l.h.s. we omitted the subscript in Σ''_j and made our usual assumption that $|\epsilon_j| \ll W$, and the rescaling $V(d_{jm})^2 = V_{\text{typ}}^2 w_m$. Random variables x_m are sampled from the distribution $g_\eta(x)$ given in (111) and plotted in Fig. 12).

Unlike the situation in the cavity method where the level broadening η in the effective model (72) has a fictitious meaning and drops out from the final result, here we will make a self-consistent assumption and set it equal to the characteristic width of the miniband

$$\eta = \Sigma''_*. \quad (134)$$

Then using GCLT for the sum in (133) one can obtain the PDF of Σ'' . The details are given in Appendix I and here we provide the result

$$\Sigma'' \stackrel{d}{=} \tilde{\Sigma}''_{\text{typ}} + x C,$$

$$\tilde{\Sigma}_{\text{typ}}'' = b_{\Omega} \Sigma_{*}'', \quad C = \sigma_{\Omega} \Sigma_{*}'' . \quad (135)$$

Here x is a random variable that obeys Levy distribution $L_1^{1,1}(x)$, coefficient σ_{Ω} is given in (128) and b_{Ω} is given in (98) where one should replace M with the number of marked states in a mini-band Ω defined in (115).

We conclude that the width C of the distribution of Σ'' given by the self-consistent Born approximation is the same as that given by the cavity method (131). The difference between the typical values of Σ'' in the two methods is

$$\Sigma_{\text{typ}}'' - \tilde{\Sigma}_{\text{typ}}'' = \frac{2}{\pi} C \log \sigma_{\Omega}^{-1} \ll \Sigma_{\text{typ}}''$$

This error is much smaller than in the case discussed in Sec. VIII A 1 (cf. Eq. (132)) where the self-consistent condition is not used. However it exceeds the distribution width C for sufficiently large $M \gg 1$ because in the non-ergodic delocalized phase $\log \sigma_{\Omega}^{-1} \sim \log \log M$.

B. Real part of self-energy

In this section we will find the marginalized probability distribution of real parts of self-energy

$$\mathcal{P}(\Sigma') = \int_0^{\infty} d\Sigma'' \mathcal{P}(\Sigma', \Sigma'') . \quad (136)$$

We consider the first equation in (104). Following the arguments provided in Sec. VIII A we neglect the terms $z - \Sigma_m'$ in the r.h.s of the equation and drop the oscillatory factors in \mathcal{H}_{0m} using the probability distribution $P(f) = g_{\infty}(f/V_{\text{typ}}^2)/V_{\text{typ}}^2$ (69) instead. Then Eq. (104a) takes the form

$$\Sigma' \stackrel{d}{=} \sum_{m=1}^M r_m . \quad (137)$$

Here r_m are instances of a random variable R such that

$$r = f \frac{\epsilon}{\epsilon^2 + (\Sigma'')^2} , \quad (138)$$

where ϵ , f , Σ'' are random variables independently sampled from the distributions $p(\epsilon)$, $P(f)$ and $\mathcal{P}(\Sigma'')$, respectively. Using GCLT, in the asymptotic limit of $M \rightarrow \infty$ the sum in (137) is determined by the tail of the probability distribution of r at $|r| \rightarrow \infty$. This analysis is very similar to the one already discussed in Sec. VI, VIII A and in Appendix F. Here we omit details of the calculations and simply provide the result. The tail of the PDF of r in the limit $|r| \rightarrow \infty$ has the form

$$\rho = \frac{r}{2\Sigma_{*}''/(\pi M)}, \quad \text{PDF}(\rho) \simeq \frac{1}{\rho^2} \sqrt{\frac{\log(\rho)}{\pi}} . \quad (139)$$

($\rho \gg 1$). The distribution function $\mathcal{P}(\Sigma')$ of the sum in (137) is the Cauchy distribution

$$\mathcal{P}(\Sigma') = \frac{1}{\pi} \frac{\Sigma'_{\text{typ}}}{(\Sigma'_{\text{typ}})^2 + (\Sigma')^2}, \quad \Sigma'_{\text{typ}} = \frac{\Sigma_{*}''}{\sigma_M} . \quad (140)$$

Here the expression for $\sigma_M \sim 1/\sqrt{\log M}$ is given in (97). Cauchy distribution has the form very similar to the stable distribution $L_1^{1,1}(x)$ that describes the fluctuations of the Σ'' (125) up to the shift and rescaling coefficients. Both distributions are displayed in Fig. 11. The tail of the Cauchy distribution differs from that of $L_1^{1,1}(x)$ by a factor of 2. Unlike that of Σ'' the distribution of Σ' is symmetric for impurity states with energies near the center of the band. The typical value of Σ' is greater than that of Σ'' by a constant factor

$$\frac{\Sigma'_{\text{typ}}}{\Sigma''_{\text{typ}}} = \frac{1}{\sqrt{2-\gamma}} \quad (W = \lambda M^{\gamma/2}) . \quad (141)$$

The width of the distribution of Σ' is the same as its typical value while the width C of the distribution of Σ'' is smaller by a factor $\sim 1/\log M$ (cf. Eqs. (130),(131)). These relations between the distributions of Σ' and Σ'' have implications for the complexity of the population transfer as discussed below. We also note that the real and imaginary parts of self-energy of a given marked state are correlated with each other because according to Eqs. (104a),(104b) the values of Σ_j' and Σ_j'' depend on the same set of parameters (\mathcal{H}_{jm} , ϵ_m , etc). In this work we will not study their correlations.

IX. COMPLEXITY OF THE POPULATION TRANSFER PROTOCOL

After the system is prepared at a given marked state $|z_j\rangle$ at $t = 0$ the probability for the population to be transferred to other marked states is $1 - \psi^2(z_j, t)$. At the initial stage the survival probability decays exponentially (76) with the mean decay time $1/\Gamma_j = 1/(2\Sigma_j'')$.

The initial marked state decays into the eigenstates $|\psi_{\beta}\rangle$ of the IB Hamiltonian \mathcal{H} with typical energies E_{β} inside the narrow interval corresponding to the miniband associated with $|z_j\rangle$. It has a width Σ_j'' and is centered around $\mathcal{H}_{jj} = \epsilon_j$. Typical classical energies ϵ of the bit-strings measured at the end of PT protocol will obey the probability distribution $\mathcal{P}(\epsilon - \epsilon_j - \Sigma_j'')$ with \mathcal{P} given in (140). The success of PT protocol is to find a bit-string distinct from z_j at a time t with energy inside that window $\Delta\mathcal{E}_{\text{cl}}$ around ϵ_j . The expected time to succeed in PT equals

$$t_{\text{pt}}^j = \frac{1}{2\Sigma_j'' p_{\Delta\mathcal{E}}}, \quad p_{\Delta\mathcal{E}} = \int_0^{\Delta\mathcal{E}_{\text{cl}}} \mathcal{P}\left(\epsilon - \Sigma_j' - \frac{\Delta\mathcal{E}_{\text{cl}}}{2}\right) d\epsilon .$$

Here $p_{\Delta\mathcal{E}}$ is the probability of detecting a bit-string inside the target window $\Delta\mathcal{E}_{\text{cl}}$ under the condition that initial

state has decayed. Let us assume that the PT window is as wide as the typical miniband width, $\Delta\mathcal{E}_{\text{cl}} = \Sigma''_{\text{typ}}$. In this case p_{mb} differs from 1 only by a constant factor that does not depend on M (cf. (141)). Therefore we will detect the bit-string inside the PT window with finite probability as long as we waited long enough for the transition away from the initial marked state to occur. Because the initial state $|z_j\rangle$ is picked at random we can estimate typical time to success of PT $t_{\text{PT}} \sim 1/\Sigma''_{\text{typ}}$ corresponding to the inverse typical width of the miniband. All of the states in a miniband are populated at (roughly) the same time t_{PT} because transition rate to a subset of states on a distance d away from $|z_j\rangle$ depends on d very weakly (see Eq. (99) and related discussion in Sec. VIA)).

From a computational perspective it is of interest to characterize the PT by the relation between the typical success time of PT t_{PT} and the number of states Ω over which the population is spread during PT

$$t_{\text{PT}} \sim \frac{1}{V_{\text{typ}} \sqrt{\Omega \log \Omega}} \sim \left(\frac{2^n}{n\Omega \log \Omega} \right)^{1/2} e^{2\theta n}. \quad (142)$$

where we set $\Delta\mathcal{E}_{\text{cl}} \sim \Sigma''_*$ (see discussion above). We note that the time t_{G} for the Grover algorithm for unstructured quantum search to find Ω items in a database of the size 2^n is $t_{\text{G}} \sim (2^n/\Omega)^{1/2}$. PT time t_{PT} scales worse than Grover time t_{G} by an additional exponential factor $e^{2\theta n} \simeq e^{\frac{n}{2B_{\perp}^2}}$ (45). The scaling exponent 2θ can be made arbitrarily small at large transverse fields $1 \ll B_{\perp} = \mathcal{O}(n^0)$.

One can expect that the distributions of eigenvalues and eigenvectors inside the mini-band are very similar to those in the ergodic case, albeit with the appropriately rescaled effective dimension Ω of the Hilbert space [35]. For example, the energy spectrum of the mini-bands in the non-ergodic delocalized phase of Rosenzweig-Porter (RP) model corresponds to the Gaussian Orthogonal ensemble. There, according to the semicircle law [50], the typical spectral width of the mini-band ($\sim 1/t_{\text{PT}}$) is proportional to the square root of the number of states Ω in it. Therefore the Grover scaling (142) for PT is consistent with semicircle law in the Gaussian random matrix models that allow for non-ergodic delocalized phase such as RP model.

However in the case of Levy matrices the distribution of eigenvalues has polynomial tails [30], their spectrum is not bounded and semi-circle law does not apply. As mentioned above, this leads to a broad distribution of PT rates. There exist statistically significant clusters of states of a relatively small size that will be populated faster than typical case because the corresponding classical bit-strings are located closer to each in Hamming distance than the typical inter-state separation. At first glance, this tendency is counter to the Grover scaling (142). We note however that fluctuations of Σ' and Σ'' are correlated with each other. Faster decay of a marked state will also correspond to bigger self-energy shift which

will reduce the likelihood of finding a marked state with its energy inside the target window $\Delta\mathcal{E}_{\text{cl}} \sim \Sigma''_*$.

However the Grover scaling still survives in a typical case corresponding to PT away from a randomly selected bit-string. For Levy matrices [30] it reflects the fact that the *typical* width Σ''_{typ} of the curve of the global density of states along the energy axis must scale as a square root of the corresponding typical number of states (area under the curve).

X. COMPARISON WITH THE ANALOGUE GROVER SEARCH

A. Grover search starting from a fully symmetrized state

So far we have studied the PT protocol with the Hamiltonian (2) $H = H_D + H_{\text{cl}}$ that starts from a given marked state of an IB model H_{cl} (3) and aims at finding a different marked state inside a given window of energies using a transverse field Hamiltonian $H_D = -B_{\perp} \sum_{m=1}^n \sigma_m^x$ (2) as a driver.

We consider here a different protocol inspired by the Hamiltonian version of Grover algorithm proposed in [18]. The new protocol finds marked states in the IB model H_{cl} starting from the ground state of H_D which is a fully symmetric state $|S\rangle = 2^{-n/2} \sum_{j=1}^n |z\rangle$ in a computational basis. This protocol can be implemented by adjusting the value of transverse field $B_{\perp} \approx 1$ so that the ground state energy of the driver is set near the center of the IB. Then we can replace the full driver with the projector on its ground state, $H_D \rightarrow -nB_{\perp} |S\rangle \langle S|$. The quantum evolution is guided by the Hamiltonian:

$$H_{\text{G}} = -nB_{\perp} |S\rangle \langle S| + \sum_{j=1}^M \mathcal{E}(z_j) |z_j\rangle \langle z_j|. \quad (143)$$

With the initial condition $|\psi(0)\rangle = |S\rangle$. In the case where all impurity energies are equal to each other, $\{\mathcal{E}(z_j) = -n\}_{j=1}^M$, and $B_{\perp} = 1$ the Hamiltonian H_{G} is a generalization of the analog version of Grover search [18] for the case of M target states. The system performs Rabi oscillations between the initial state $|S\rangle$ and the state which is an equal superposition of all marked (solution) states. Time to solution is the half-period of the oscillations, the "Grover time" t_{G}

$$t_{\text{G}} = \frac{\pi}{2nB_{\perp}} \sqrt{\frac{2^n}{M}}. \quad (144)$$

Hamiltonian versions of Grover search with transverse field driver whose ground state were tuned at resonance with that of the solution state were considered in [51, 52].

Robustness of the Grover algorithms to phase noise was considered previously in the case of a single marked state [53, 54]. Here we investigate the role of systematic phase errors in quantum oracle for the case of multiple

solutions by assuming that marked state energies take distinct values $\mathcal{E}(z_j) = -n + \epsilon_j$ randomly distributed over some narrow range W . We will also investigate the systematic error in the Grover diffusion operator[1]. In the Hamiltonian formulation [18] this corresponds to the deviation from unity of the parameter B_\perp that controls the weight of the driver in (144). We will define

$$B_\perp = 1 - \frac{\epsilon_0}{n}, \quad (145)$$

where ϵ_0 is the driver error.

We denote the computational basis states as $|j\rangle \equiv |z_j\rangle$ with $j \in [1, N]$, $N = 2^n$ and assume that marked states correspond to the range $j \in [1, M]$. We also introduce the state $|0\rangle = \frac{1}{\sqrt{N-M}} \sum_{j=M+1}^N |j\rangle$ that is orthogonal to all the marked states. The subset of basis vectors $\mathcal{S} = \{|j\rangle\}_{j=0}^M$ spans the $M+1$ dimensional subspace with the remaining set \mathcal{S}_\perp of basis vectors spanning the orthogonal $N-M-1$ dimensional subspace. One can show that H_G does not have matrix elements that couple \mathcal{S} with \mathcal{S}_\perp .

Assuming that $N \gg M$ one can consider the decay of the state $|0\rangle$ instead of the state $|S\rangle$. We use (145) and omit constant terms and small corrections $\mathcal{O}(M/N)$ in H_G . The non-zero matrix elements $H_G^{ij} = \langle i | H_G | j \rangle$ in this subspace \mathcal{S} have the form

$$H_G^{jj} = \epsilon_j, \quad H_G^{j0} = -(1 - \delta_{j0})V, \quad V = n2^{-n/2}, \quad (146)$$

where $j \in [0, M]$ and $H_G^{j0} = H_G^{0j}$. On a time scale $t \ll 1/\delta\epsilon = M/W$ much smaller than the inverse spacing of the energies ϵ_j the quantum evolution with initial condition $|\psi(0)\rangle = |0\rangle$ corresponds to the decay of the discrete state with energy ϵ_0 into the continuum [46] with the finite spectral width W [55]. It is a similar problem to that discussed in the Sec. VI.

1. Sensitivity to systematic oracle phase error

We first consider the case of relatively large oracle errors (wide energy band W)

$$V\sqrt{M} \ll W \ll VM, \quad (147)$$

and modest driver errors

$$\epsilon_0 = n(1 - B_\perp) \lesssim W. \quad (148)$$

In this case, following the results of the Sec. VI on the solution of the Fano-Anderson model [55] we obtain an exponential decay of the initial amplitude (cf. (76))

$$\psi_0(t) \simeq \exp[-\Sigma_0'' t - i\epsilon_0 t - i\Sigma_0'(\epsilon_0 + i0^+)t]. \quad (149)$$

where $\Sigma_0(z) = \Sigma_0'(z) + i\Sigma_0''(z)$ is a self-energy and

$$\Sigma_0(z) = V^2 \sum_{m=1}^M \frac{1}{z - \epsilon_m}, \quad \Sigma_0'' \equiv \frac{1}{2}\Gamma_0 = \frac{\pi V^2}{W/M}. \quad (150)$$

The state $|0\rangle$ undergoes an exponential decay with the rate $\Gamma_0 = 2\Sigma_0''$. After the characteristic time $t_{PT} \sim 1/\Gamma_0$ the population is transferred into a subset of the marked states with energies inside the window $|\epsilon_j - \epsilon_0| \simeq \Sigma_0'' \ll W$.

The number of marked states (solutions) to which the population is transferred is $\Omega \sim \Sigma_0''/\delta\epsilon$. The relation between t_{PT} and Ω is

$$t_{PT} \sim \frac{1}{V\sqrt{\Omega}}, \quad \Omega \sim \left(\frac{V}{W/M}\right)^2, \quad (151)$$

the same as in the Grover algorithm (144). It also recovers the scaling with Ω and n , up to a factor $\exp(-n/(2B_\perp^2))$, for the time of PT considered in the rest of the paper that uses transverse field as a driver and starts from any marked state instead of a fully-symmetric state.

To characterize the effect of oracle errors we introduce the scaling ansatz for the marked states bandwidth $W \sim 2^{-n/2} M^{\gamma/2}$ similar to that in (70). We observe that the number Ω of solution states populated over the time t_{PT} cannot be greater than M by construction. For $W \lesssim V\sqrt{M}$ (or $\gamma < 1$) the value of $\Omega \simeq M$ and the scaling of the transfer time t_{PT} with M is the same as t_G in the ideal Grover algorithm (144). In the region given by (147) (or $2 > \gamma > 1$) the algorithm performance is degraded because $\Omega \ll M$. For $W \gg VM$ (or $\gamma > 2$) the algorithm fails to find even one solution.

2. Sensitivity to the systematic driver error

We now consider the sensitivity of the algorithm to an error in the weight of the driver Hamiltonian, i.e., to the nonzero value of the parameter $\epsilon_0 = n(1 - B_\perp)$ (145). We assume that $\epsilon_0 \gg W$ while the spread of the marked state energies the condition (147), so that absent driver errors, PT time would follow a Grover-like scaling law (151).

In this case the state $|0\rangle$ is coupled non-resonantly to a continuum with narrow bandwidth. The expression for the population transfer to the marked states can be obtained from the time-dependent perturbation theory in the parameter ϵ_0/W

$$\sum_{m=1}^M |\psi_m(t)|^2 = \frac{2MV^2}{\epsilon_0^2} \left(1 - \cos(\epsilon_0 t) \frac{\sin(Wt/2)}{Wt/2}\right).$$

Maximum transfer occurs at the time $t_0 = \pi/\epsilon_0$ with the total transferred probability $p_0 = 4MV^2/\epsilon_0^2$. Typical time $t_{PT} \simeq t_0/p_0$ to achieve the successful population

transfer to marked states involves repeating the experiment $1/p_0$ times

$$t_{\text{PT}} = \frac{1}{\Gamma_0} \frac{\pi^2 \epsilon_0}{W}, \quad (152)$$

where Γ_0 is given in (150) and the first multiple in r.h.s gives the typical transfer time in the absence of driver errors. The later leads to an increase of the transfer time by a large factor ϵ_0/W .

For the maximum possible bandwidth W when nearly all states are populated, $W \sim \Gamma_0 \sim V\sqrt{M}$, the time of population transfer (152) is

$$t_{\text{PT}} \sim t_G (t_G \epsilon_0) \quad (\epsilon_0 \gg t_G^{-1} \sim V\sqrt{M}). \quad (153)$$

As expected, when the driver error exceeds inverse Grover time $1/t_G$ the performance of analogue Grover algorithms (143) degrades relative to t_G . This is a direct consequence of the fact that the quantum evolution begins from fully symmetric state which is a ground state of the driver Hamiltonian whose energy is tuned at resonance with the marked states. In this case the transverse field Hamiltonian driver effectively corresponds to the projector (143). Because the ground state is not degenerate, the resonance region is exponentially narrow ($\sim 2^{-n/2}\sqrt{M}$). This results in the exponential sensitivity of the Grover algorithm performance to the value of driver weight. This critical behavior was studied in the work on quantum spatial search [56] for the case of one marked state.

In contrast, in the PT protocol considered earlier in the paper there was no need to fine-tune the value of B_\perp other than making it large, $B_\perp \gg 1$. This happened because the effective coupling between the marked states described by the down-folded Hamiltonian \mathcal{H} (40) was not due to any one particular eigenstate of the driver (such as the state $|S\rangle$ for the Grover case). Instead this coupling was formed due to an exponentially large (in n) number of non-resonant, virtual transitions between the marked states and highly excited states of the transverse field Hamiltonian H_D . This resulted in a significant improvement in robustness for the proposed PT relative to the analogue Grover algorithm.

B. Grover search starting from a marked state

We now consider an implementation of the analogue Grover search that starts from the marked state similar to the PT protocol considered in previous Sections. The transition amplitude $U_{ij}(t) = \langle i | \exp(-iH_G t) | j \rangle$ between the two marked states can be written in the form

$$U_{ji}(t) = \sum_{\lambda} e^{-i\lambda t} \psi_{\lambda}(i) \psi_{\lambda}(j). \quad (154)$$

Here $\psi_{\lambda}(j) = \langle j | \psi_{\lambda} \rangle$ are amplitudes of the eigenstates of H_G in the $M+1$ dimensional subspace and λ are the

corresponding eigenvalues that obey the equation

$$\lambda = \epsilon_0 + \sum_{j=1}^M \frac{V^2}{\lambda - \epsilon_j}, \quad \psi_{\lambda}(j) = \frac{V}{\lambda - \epsilon_j} \frac{1}{\sqrt{Z_{\lambda}}}. \quad (155)$$

Here

$$Z(\lambda) = 1 + \sum_{m=0}^M \frac{V^2}{(\lambda - \epsilon_m)^2}. \quad (156)$$

Instead of providing a detailed analysis of the above solution we provide an order of magnitude estimate to extract the relevant scaling behavior. We again assume that the spread of the marked state energies, $W = t_G^{-1} = \mathcal{O}(V\sqrt{M})$ corresponds to the inverse of the Grover time t_G needed to find any one of the solutions with equal probability. The typical separation between the adjacent values of ϵ_j is $\delta\epsilon = W/M \sim V/\sqrt{M}$.

It follows from (155) that in the *ordered* array obtained by combining together the sets of energies $\{\epsilon_j\}_{j=0}^M$ and eigenvalues $\{\lambda_m\}_{m=0}^M$ their values appear alternatively and sequentially, e.g., $\epsilon_{j-1} < \lambda_j < \epsilon_j < \lambda_{j+1}$. The typical separation between the adjacent elements in the array is $|\lambda_j - \epsilon_j| \sim \delta\epsilon$. We observe that for a given value of λ the sum in the expression for $Z(\lambda)$ (156) is dominated by the small, $\mathcal{O}(1)$, number of terms with $|\epsilon_m - \lambda| \sim \delta\epsilon$, each term of the order of M . Indeed, there are $\mathcal{O}(M)$ remaining terms corresponding to $|\epsilon_m - \lambda| \sim W$. The magnitude of those terms is $V^2/W^2 \sim 1/M$ and their aggregated contribution to the sum is $\mathcal{O}(1)$. Therefore we can estimate $Z(\lambda) = \mathcal{O}(M)$ and for the amplitudes we have

$$\psi_{\lambda}(m) \sim \frac{V}{\lambda - \epsilon_m} \frac{1}{\sqrt{M}}, \quad m = i, j. \quad (157)$$

For a given initial state $|i\rangle$ at time t we pick the final state $|j\rangle$ within the energy window $\epsilon_j - \epsilon_i \sim \Delta = 1/t$ around ϵ_i . The sum in the expression (154) for the transition amplitude $U_{ji}(t)$ is dominated by the number of terms $\Omega = \Delta/\delta\epsilon \sim \Delta\sqrt{M}/V$ corresponding to the eigenvalues λ inside the same window of energies. For those terms $\lambda - \epsilon_i, \epsilon_j - \lambda \sim \Delta$ giving the estimate for the amplitudes $\psi_{\lambda}(i), \psi_{\lambda}(j) \sim 1/\Omega$ (cf. (157)). The magnitude of the sum in (154) can be estimated as $|U_{ij}(t)| \sim \Omega |\psi_{\lambda}(i)\psi_{\lambda}(j)| \sim 1/\Omega$. On the other hand, because ordered values of λ and ϵ_m alternate in sequence the probability $|U_{ij}(t)|^2$ is distributed over Ω marked states and $|U_{ij}(t)| \sim \Omega^{-1/2}$. By equating the above two estimates for $|U_{ij}(t)|$ we immediately obtain $\Omega \sim 1$ and therefore

$$\Delta = \frac{1}{t} \sim \delta\epsilon \sim \frac{V}{\sqrt{M}}, \quad (\Omega \sim 1). \quad (158)$$

In the case when there are only a few marked states ($M \sim 1$ and $W \sim V$) the probability is initially localized on a given marked state $|i\rangle$ and then it spreads over to

others states separated in energy by V during the time $t_G \sim 1/V \sim 2^{n/2}$. In this case the algorithm time scales with n identically to that of the analogue Grover search that starts at the fully symmetric state $|S\rangle$. Similar performance is achieved by the PT protocol using transverse field $B_\perp \gg 1$ and discussed in previous sections.

The difference from analogue Grover search starting at $|S\rangle$ from the above PT protocol using a transverse field becomes dramatic for large number of marked states $M \gg 1$. Both analogue Grover search and the PT protocol benefit from the increase in M : the algorithmic time shrinks $\propto 1/\sqrt{M}$ and the number of marked (solution) states Ω in the number of states in the final superposition increases with M .

In contrast, the quantum search with H_G starting from the marked state $|i\rangle$ does not create massive superpositions of solution states when M increases. Instead it involves a very few others states that are adjacent in energy, $|\epsilon_j - \epsilon_i| \sim V/\sqrt{M}$. The time of the algorithm increases with M (158). This happens because unlike the Hamiltonian H with a transverse field (2), the Hamiltonian H_G is integrable. The wave-function remains localized near the initial marked state.

XI. NUMERICAL SIMULATIONS

It is instructive to compare the results of analytical calculations presented in previous Sections to numerical simulations. In this Section we report exact diagonalization analysis of both the eigenstate statistics and the dynamic correlator and combine them to confirm the scaling of the population transfer time obtained analytically.

A. Numerical results

Instead of the sparse $2^n \times 2^n$ Hamiltonian Eq. (2), it is efficient to diagonalize the dense $M \times M$ down-folded Hamiltonian, which allows access to systems of up to $n = 200$ qubits. The down-folded matrix Hamiltonian ensemble, is constructed as in Sec. V,

$$\mathcal{H}_{ii} = \epsilon_i, \quad \mathcal{H}_{ij} = nc(E^{(0)}, d_{ij}), \quad (159)$$

where the diagonal elements ϵ_m are distributed uniformly in the energy window $[-n - W/2, -n + W/2]$, and the off-diagonal elements are constructed by sampling Hamming distances between uniformly random bitstrings of length n and using Eq. (20) with $E = E^{(0)}$ determined from Eqs. (33),(34). We introduce the scaling of the bandwidth, see also Eq. (70),

$$W = \lambda M^{\gamma/2} V_{\text{typ}}, \quad (160)$$

where γ is a real non-negative parameter, and λ is an auxiliary constant. The typical value of the matrix element V_{typ} given in Eq. (53).

1. Eigenstate statistics

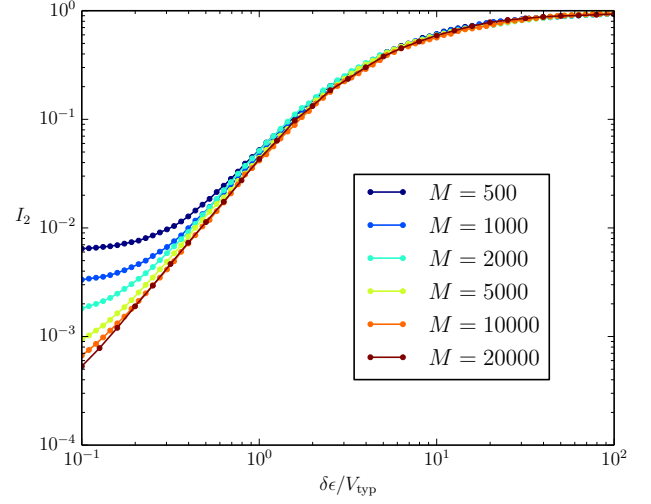


Figure 13. The inverse participation ratio $I_2 = \sum_i |\langle i|\psi\rangle|^4$ as a function of the average classical (at vanishing transverse field) energy level spacing $\delta\epsilon$ in units of the typical coupling V_{typ} for different numbers, M , of states in the impurity band. We see that for $\delta\epsilon/V_{\text{typ}} \geq 1$ the eigenstates become localized and $I_2 \rightarrow 1$ independent of M , indicative of eigenstates localized on single bitstring each.

We define the inverse participation ratios (IPRs) I_q and the entropy H^z as

$$I_q = \sum_i |\langle \psi_\beta | i \rangle|^{2q}, \quad (161)$$

$$H^z = - \sum_i |\langle \psi_\beta | i \rangle|^2 \ln |\langle \psi_\beta | i \rangle|^2, \quad (162)$$

where ψ_β denotes an eigenstate with eigenvalue E_β . IPR I_2 is the second moment of the wave function probability distribution $|\langle \psi_\beta | i \rangle|^2$ in the computational basis (bitstrings) $|i\rangle$. The entropy H^z characterizes the support set of an eigenstate in the computational basis [57], i.e. the subset of bitstrings where the probabilities $|\langle \psi_\beta | i \rangle|^2$ are concentrated. Fig. 13 indicates localized regime where $|\langle \psi_\beta | i \rangle|^2$ is localized over a finite number of basis states $|i\rangle$ with exponentially decaying tails, as a result $I_2 \sim 1$ and is system size independent. This occurs as average level spacing becomes larger than the typical matrix element $\delta\epsilon > V_{\text{typ}}$, and the eigenfunction is the superposition of a small number of basis states close in Hamming distance to each other. In our model marked states are separated by Hamming distance $d \approx n/2 + \mathcal{O}(\sqrt{n})$ with high probability and therefore most localized states have sharp peaks at exactly one bitstring, hence $I_2 \approx 1$. Fig. 14 indicates that the combination $I_2 M/3 \sim 1$ becomes system size independent as level spacing becomes smaller than the typical matrix element, characteristic of delocalized regime. The factor $1/3$ is consistent with Porter-

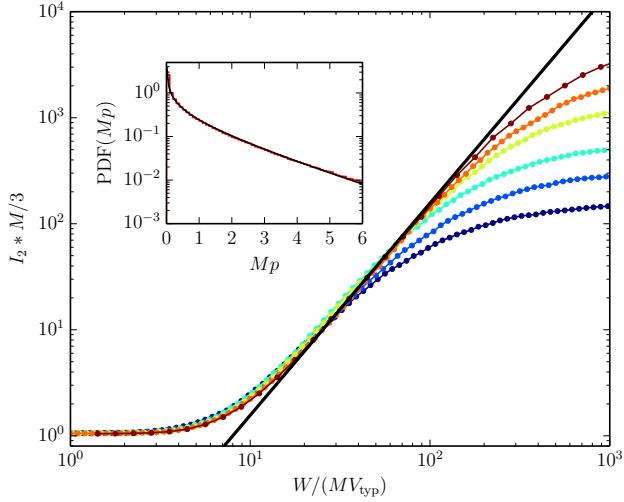


Figure 14. The re-scaled inverse participation ratio $I_2 * M/3$ as a function of the re-scaled impurity band width $W/(MV_{\text{typ}})$ for different numbers, M , of states in the impurity band. We see that in the ergodic regime, $W/(MV_{\text{typ}}) \leq 1$, we have $I_2 * M/3 = 1$, corresponding to the orthogonal Porter-Thomas distribution of states in the impurity band. The inset shows the numerical probability distribution of normalized probabilities Mp for an eigenstate over computational states z in the ergodic regime in black, and the analytical orthogonal Porter-Thomas distribution in red. Qualitative arguments in Section VI suggest that in the non-ergodic delocalized regime $I_2 * M/3 \propto (W/(MV_{\text{typ}}))^2$. The black line is proportional to $(W/(MV_{\text{typ}}))^2$ and we see that $I_2 * M/3$ aligns with this quantity as long as we do not enter the localized regime $\delta\epsilon/V_{\text{typ}} \geq 1$, see Fig. 13.

Thomas distribution of the wave function amplitudes in this regime $|\langle\psi_\beta|i\rangle|^2 \sim 1/M$. Both Figs. 13 and 14 show a wide intermediate region where non-ergodic dynamics is expected. This intermediate regime becomes apparent in Fig. 15 where we introduce the multi-fractal dimensions D_q and D_1 which determine the scaling of I_q and H^z with M , respectively,

$$\ln I_q(M) = -D_q(q-1) \ln M + c_q, \quad (163)$$

$$H^z(M) = D_1 \ln M + c_1, \quad (164)$$

where c_q is a q -dependent fitting parameter. The extracted dimensions shown in Fig. 15 as a function of the parameter γ vary continuously between $D_q = 1$ in the ergodic phase $\gamma \leq 1$ and $D_q = 0$ in the localized phase $\gamma \geq 2$, with $1 < \gamma < 2$ corresponding to non-ergodic regime for $q = 1, 2$.

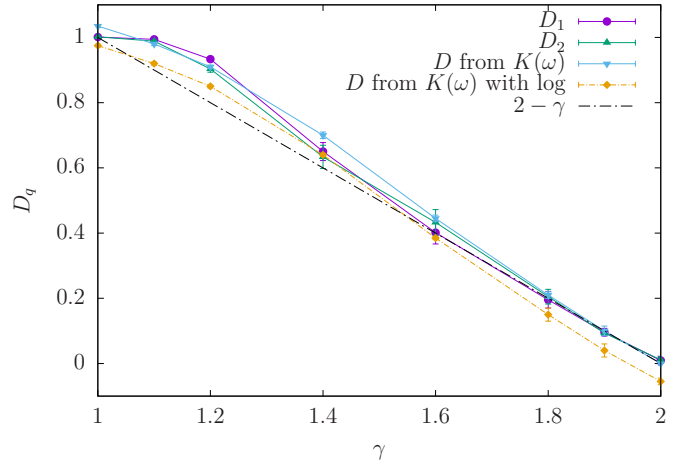


Figure 15. The multifractal dimensions D_1 (defined in Eq. (164)) and D_2 , (defined in Eq. (163)) as functions of γ for the ensemble of IB Hamiltonians with the dispersion of classical energies $W = \lambda V_{\text{typ}} M^{\gamma/2}$, with $\lambda = 3.3$. All the multifractal dimensions D_q approach 1 in the ergodic regime ($\gamma = 1$) and 0 in the localized regime ($\gamma = 2$). The difference between D_1 and D_2 is also likely due to finite size effects. We also extract a scaling exponent from the dynamical correlator (see Eqs. (166),(167)). Dot-dashed line corresponds to the analytical value in the Rosenzweig-Porter limit given by Eq. (170).

2. Dynamic correlation

The Fourier transform of the survival probability for a given initial marked state i is given by,

$$\begin{aligned} p_i(\omega) &= \text{Re} \int_0^\infty dt e^{i\omega t} |\langle i|\psi(t)\rangle|^2 \\ &= \pi \sum_{\beta, \beta'} |\langle i|\psi_\beta\rangle|^2 |\langle \psi_{\beta'}|i\rangle|^2 \delta(E_\beta - E_{\beta'} - \omega). \end{aligned} \quad (165)$$

Note that the limit $\omega \rightarrow 0$ gives the inverse participation ratio of a given bitstring in the basis of eigenstates,

$$p_i(0) = \pi \sum_{\beta} |\langle i|\psi_\beta\rangle|^4. \quad (166)$$

The average of $p_i(\omega)$ over the initial state is related to the overlap correlation function $K(\omega)$ defined by [35],

$$\begin{aligned} K(\omega) &\equiv \frac{1}{M} \sum_{i, \beta, \beta'} |\langle \psi_\beta|i\rangle|^2 |\langle \psi_{\beta'}|i\rangle|^2 \delta(E_\beta - E_{\beta'} - \omega) \\ &= \frac{1}{\pi M} \sum_i p_i(\omega). \end{aligned} \quad (167)$$

The fractal dimension extracted from the scaling of $K(0)$ with M is shown in Fig. 15, it follows closely those extracted from the IPR in the computational basis. The collapse of the plots in Fig. 16 is achieved when the fre-

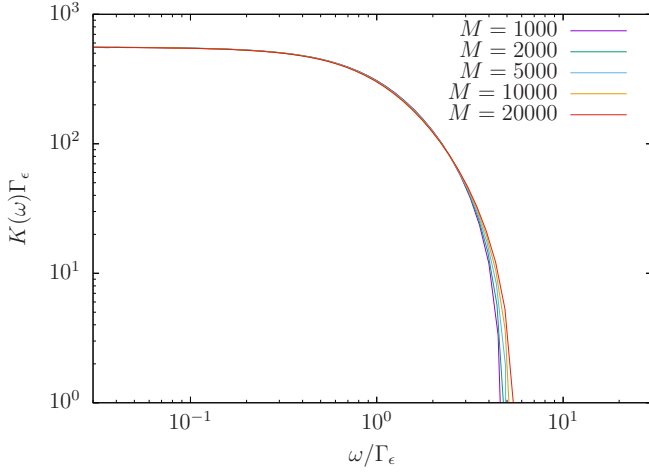


Figure 16. We plot the rescaled overlap correlation function $K(\omega)\Gamma_\epsilon$ vs. ω/Γ_ϵ , where $\Gamma_\epsilon = \Gamma_{\text{typ}}M^\epsilon$ and $\Gamma_{\text{typ}} = 2\Sigma''_{\text{typ}}$ is the typical mini-band width and $\Sigma''_{\text{typ}} \propto V_{\text{typ}}M^{1-\gamma/2}(\log M)^{1/2}$, Eq. (130). Different curves correspond to different values of M , and collapse well with $\epsilon = 0.05$. We used the ensemble of IB Hamiltonians with a dispersion of classical energies $W = \lambda V_{\text{typ}}M^{\gamma/2}$, with $\gamma = 1.2$ and $\lambda = 3.3$.

quency is rescaled by the characteristic energy,

$$\Gamma_\epsilon = 2\Sigma''_{\text{typ}}M^\epsilon, \quad (168)$$

where $\Gamma = 2\Sigma''_{\text{typ}}$ is the typical mini-band width. The correlator $K(\omega)$ is constant for a range of energy differences $\omega < \Gamma_\epsilon$ and decays quickly $\propto \omega^{-2}$ as $\omega > \Gamma_\epsilon$. This can be interpreted in the following way: for an average bitstring there is a range of eigenenergies E_β within a width Γ_ϵ around a bitstring dependent value ϵ_j where the eigenfunction overlaps with z_j are relatively large, whereas for larger energy difference the correlation decays quickly below the value corresponding to uncorrelated case $K(\omega) < K_{\text{uncorr}} \sim M/\Omega^2$ (where Ω is the number of states in the mini-band), i.e. the amplitudes repel each other. This picture is consistent with the interpretation in terms of mini-bands outlined in previous Sections, where the eigenstates within the mini-band have significantly overlapping supports reflected in the dynamical correlator. This means that the characteristic population transfer is given by the inverse of the characteristic energy scale of the mini-band Γ_ϵ , the range of energy eigenstates with significant amplitude at the given bitstring. The auxiliary fitting parameter takes a small value $\epsilon = 0.05$ indicating only a small deviation from $\Gamma_{\text{typ}} = 2\Sigma''_{\text{typ}}$ most likely due to finite size effects.

B. Comparison to analytical results

The size of the matrix of marked states used in exact diagonalization $M \leq 20000$ is a small fraction of the size of the total Hilbert space Hamiltonian $2^n \times 2^n$

with $n = 200$. For such a small sample the distribution of the Hamming distances d_{ij} between marked states is dominated by $|d_{ij} - n/2| \sim \mathcal{O}(\sqrt{n})$. In this regime the square of the off-diagonal matrix element, see Sec. III, has approximately Gaussian dependence on d_{ij} (cf. Eqs. (40),(41))

$$\mathcal{H}_{ij}^2 \approx V_{\text{typ}}^2 \exp\left(\frac{2}{n}\left(d_{ij} - \frac{n}{2}\right)^2\right), \quad (169)$$

and the probability of smaller distances d is strongly suppressed. The sign of \mathcal{H}_{ij} rapidly fluctuates as a function of d resulting in a negligible average $\langle \mathcal{H}_{ij}(d) \rangle \sim \mathcal{O}(2^{-n})$. This realizes an analog of the Rosenzweig-Porter (RP) model from random matrix theory, see Ref. 35 and 38 and references therein, where the matrix elements are given by Gaussian random variable with zero mean and variance for diagonal and all off-diagonal matrix elements set $\langle \mathcal{H}_{ii}^2 \rangle = 1$ and $\langle \mathcal{H}_{ij}^2 \rangle \propto M^\gamma$. The distribution of off-diagonal matrix elements in Eq. (169) is not Gaussian. Nonetheless, we expect properties of the two models to be qualitatively similar.

1. Eigenstate statistics

The eigenstate statistics and the respective fractal dimensions for the model Eq. (169) can be calculated using strong disorder perturbation theory [35],

$$D_1 = D_2 = 2 - \gamma. \quad (170)$$

This approach cannot take into account the effect of delocalized states in the mini-band and therefore the result in Eq. (170) is only an approximation. The solution of the non-linear cavity equations for the Green's function obtained in Sec. VIII together with expressions relating the IPRs and the Green's function [31, 58] allow a rigorous calculation of the fractal dimensions for our model. We leave this for future work. Comparison of the approximate Eq. (170) with numerical results is shown in Fig. 15 as the dot-dashed line. It appears that the D_1 and D_2 do not quite coincide with each other nor with Eq. (170), which may be due to finite size effects or a result of deviation of our model from the Rosenzweig-Porter model.

2. Dynamic correlations

For states close to the center of the band of marked states the typical value of the mini-band width can be connected to the average of the dynamical correlator, with the delta function regularized by a finite scale $\eta, \Sigma''_{\text{typ}} \gg \eta \gg \delta\epsilon, \delta(x) \rightarrow \delta_\eta(x) \equiv \frac{1}{\pi} \frac{\eta}{x^2 + \eta^2}$,

$$\frac{1}{\Sigma''_{\text{typ}} + \eta} = \frac{1}{\pi} \int_{-\infty}^{\infty} d\omega \frac{\eta}{\eta^2 + \omega^2} p(\omega), \quad (171)$$

which can be inverted to obtain,

$$p(\omega) \approx \begin{cases} \frac{1}{\Sigma''_{\text{typ}}}, & \omega \leq \omega_{\text{Th}} \\ \frac{1}{\Sigma''_{\text{typ}}} \left(\frac{\omega_{\text{Th}}}{|\omega|} \right)^2, & \omega > \omega_{\text{Th}} \end{cases} \quad (172)$$

where we introduced the Thouless energy,

$$\omega_{\text{Th}} = \frac{1}{2} \pi \Sigma''_{\text{typ}}. \quad (173)$$

The typical value of the mini-band width was obtained in Eq. (130). The scaling of the Thouless energy as well as,

$$K(0) = \frac{\lambda}{\sqrt{8\pi^3(1-\gamma/2)}} V_{\text{typ}}^{-1} (\log M)^{-1/2} M^{\gamma/2-1}, \quad (174)$$

with M can be directly compared to the mini-band width Γ_ε and $K(0)$ obtained numerically. From the comparison of the respective Fig. 15 we conclude that the scaling of the typical population transfer time $1/\omega_{\text{Th}}$ and the scaling of the value of the dynamical correlator $K(\omega)$ are consistent in numerical and analytical calculations, subject only to a small correction in the scaling exponent $\varepsilon = 0.05$.

Note that in our analysis of the PT protocol complexity, Sec. IX, in addition to the solution of cavity equations for the width of the many-body miniband we estimated the number of states in the mini-band Ω , see Eqs. (115), (129) using the classical value of the average level spacing $\delta\varepsilon$ (at vanishing transverse field). In Appendix J we report numerical simulations where we do not make this approximation.

XII. OUTLOOK

We believe that the approach developed in this paper can be generalized beyond the IB model to study PT in other types of transverse field quantum spin-glass problems (2). In the typical problem of interest, the classical energy landscape contains a large number of deep local minima separated by Hamming distances $d = \mathcal{O}(n)$ and an exponential number of them, $M = 2^{\mu n}$, $\mu = \mathcal{O}(1)$, are located within some narrow strip $\Delta\mathcal{E}_{\text{cl}}$ of classical energies chosen at the tail of the distribution $P_{\text{cl}}(\mathcal{E})$ that decays exponentially with the distance from its maximum. Such situation occurs, e.g., in the Random Energy Model [59], p -spin model with $p > 2$ [60], and other problems under certain choices of the ensemble parameters.

The objective as before is to estimate the statistics and the scaling of the miniband sizes with n in the energy strip $\Delta\mathcal{E}_{\text{cl}}$ for large enough values of n , where finite size effects are small, typically $n \sim 100$ or more. Direct numerical solution of the Schrödinger equation is no longer computationally tractable at these sizes.

Essentially, our approach is based on the existence of two distinct energy scales. The first scale is the typi-

cal change in classical energy corresponding to one bit flip: $\mathcal{E}_{\text{flip}} \lesssim B_\perp$. The second scale is the typical width of non-ergodic minibands Γ inside the energy window $\Delta\mathcal{E}_{\text{cl}} > \Gamma$, which decreases exponentially with n . The tunneling transitions between the states inside the miniband correspond to a high order of perturbation theory in B_\perp , and therefore $\mathcal{E}_{\text{flip}} > \Gamma$. Starting from the initial state $|z_i\rangle$ inside the strip of energies $\Delta\mathcal{E}_{\text{cl}}$, the quantum evolution is confined within the corresponding miniband. This evolution can be described by an effective down-folded Hamiltonian \mathcal{H}_{ij} defined over a subset of computational basis states whose classical energies lie within the energy strip $\Delta\mathcal{E}_{\text{cl}}$.

The effective Hamiltonian \mathcal{H} arises in the self-energy formalism [61, 62]. The off-diagonal matrix elements \mathcal{H}_{ij} can be understood in terms of the locator expansion [22], i.e., by expanding the matrix elements of the resolvent of H (2) in powers of the transverse field B_\perp . Each matrix element \mathcal{H}_{ij} corresponds to the sum over all elementary spin-flip processes that begin in the state $|z_i\rangle$, proceed through virtual states separated by energies at least $\mathcal{E}_{\text{flip}}$ from the corresponding miniband, and return back to the miniband only at the last step, at the state $|z_j\rangle$. We emphasize that \mathcal{H}_{ij} takes into account the trajectories containing loops, i.e., multiple visits of the high-energy virtual states.

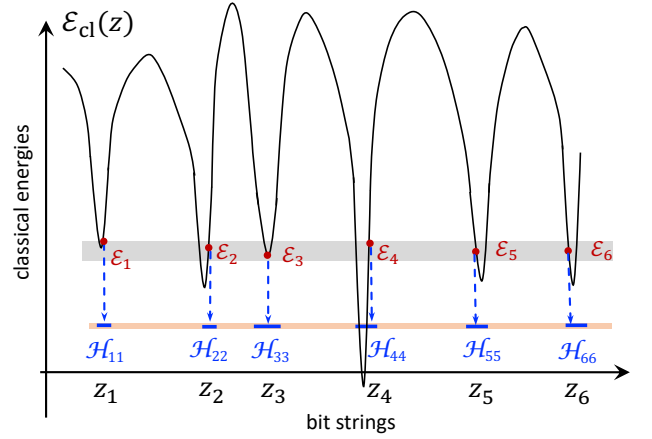


Figure 17. This cartoon depicts the energy landscape $\mathcal{E}(z)$. Red dots depict the classical energies \mathcal{E}_j of the computational basis states $|z_j\rangle$ whose shifted energies \mathcal{H}_{ij} (depicted with horizontal red lines) belong to the narrow miniband shown with the light orange line. Blue dashed arrows show the self-energy shifts. Light gray rectangle depicts the energy strip $\Delta\mathcal{E}_{\text{cl}}$ for the PT protocol.

There is an important difference between the diagonal and off-diagonal matrix elements of \mathcal{H} . The off-diagonal elements \mathcal{H}_{ij} are exponentially small in n since the Hamming distances between the states are extensive, $d_{ij} = \mathcal{O}(n)$. They are determined by the elementary spin-flip process of a very high order in B_\perp . The distribution of \mathcal{H}_{ij} can be estimated either analytically via the WKB approach or numerically via the forward scattering

approximation [26, 63].

At the same time the renormalization of the diagonal matrix elements $\mathcal{H}_{ii} - \mathcal{E}(z_i)$ appears already in the second order in B_\perp . This fact is not important for the IB model where the renormalization is exactly the same for all marked states z_i and thus leads to a uniform shift of their energies. Therefore if \mathcal{H}_{ii} and \mathcal{H}_{jj} are separated by a very small energy then so are $\mathcal{E}(z_i)$ and $\mathcal{E}(z_j)$.

Unfortunately generally this is not the case. Repeating PT experiments starting from the same state $|z_i\rangle$ will produce a set of states $|z_j\rangle$ at the output. The dispersion of the corresponding values of $\mathcal{H}_{jj} - \mathcal{H}_{ii}$ is very small – of the order of the miniband width Γ_i . However, the dispersion of the classical energies \mathcal{E}_j is much bigger due to renormalization of the diagonal matrix elements $\mathcal{H}_{ii} - \mathcal{E}_i$ by transverse field. The values of \mathcal{E}_j observed in PT will be distributed with the width $\mathcal{O}(n^{1/2})$ around some mean value shifted by $\mathcal{O}(n)$ from the center of the miniband (see Fig. 17). Therefore one must consider the PT window that is much wider than the miniband width, $\Delta\mathcal{E}_{\text{cl}} = \mathcal{O}(n^{1/2})$.

Suppose that a classical algorithm proceeds via a continuous-time random walk between the states inside the window $\Delta\mathcal{E}_{\text{cl}}$ with the transition rate matrix Q_{ij} and a typical matrix element Q_{typ} . Given the PDF of classical energies $P_{\text{cl}}(\mathcal{E})$ the separation between the neighboring energy values is $\delta\epsilon = 1/(2^n P_{\text{cl}}(\mathcal{E}_j))$ and the number of states with the classical energies inside the strip $\Delta\mathcal{E}_{\text{cl}}$ is $2^n P_{\text{cl}}(\mathcal{E}_j) \Delta\mathcal{E}_{\text{cl}}$. Then the quantum (t_{PT}) and classical (t_{cl}) search times starting from $|z_i\rangle$ are

$$t_{\text{pt}} \sim \frac{V_{\text{typ}}^{-2}}{2^n P_{\text{cl}}(\mathcal{E}_i)}, \quad t_{\text{cl}} \sim \frac{Q_{\text{typ}}^{-1}}{2^n P_{\text{cl}}(\mathcal{E}_i) \Delta\mathcal{E}_{\text{cl}}}, \quad (175)$$

where V_{typ} is the typical value of the off-diagonal matrix elements. Here we used the estimate (95) for the quantum transition rate that also determines the width of the mini-band $\Gamma_i \sim 1/t_{\text{PT}}$. Assuming that both the quantum and classical searches are unstructured we get $V_{\text{typ}}^2 \lesssim Q_{\text{typ}} \sim 2^{-n}$. It follows from Eq. (175) that the quantum speed-up observed in IB model is lost because $\Delta\mathcal{E}_{\text{cl}}$ scales down at most polynomially with n .

However the PT computational primitive can be modified in a way that the quantum speed up is restored. Given an initial bit-string z_i the task is to find a bit-string $z_j \neq z_i$ such that $|\mathcal{H}_{ii} - \mathcal{H}_{jj}| \leq \Delta\mathcal{E}_{\text{cl}}$. Quantum PT protocol to solve this problem is to start from the state $|z_i\rangle$, evolve the system under the Hamiltonian $H(2)$, measure in computational basis, and check if the outcome z_j is the solution.

Because the dispersion of the renormalized energy values \mathcal{H}_{jj} is small for the states within the same miniband, the width of the PT window can be chosen very narrow $\Delta\mathcal{E}_{\text{cl}} \gtrsim \Gamma_i \sim 1/t_{\text{PT}}$. Consequently, the quantum speed up in Eq. (175) is recovered.

It is crucial that we can check the correctness of the solution with a classical computer: given the bit-string z_j a classical algorithm should determine the value of \mathcal{H}_{jj}

with the accuracy $\mathcal{O}(\Gamma)$. This could be done by computing numerically the locator expansion of the resolvent of $H(2)$ in powers of B_\perp . An alternative approach is to use Stochastic Series Expansion (SSE) algorithms [64–66] to compute the contribution to the partition function $\text{Tr} \exp(-\beta H)$ from the valley of $\mathcal{E}(z)$ containing the bit-string z_j by expanding it in powers of inverse temperature β and transverse field [66].³ We note that the level of precision required does not involve the hybridization of the state $|z_j\rangle$ with the states from other deep minima with comparable energies (cf. Fig. 18). This limits the Hamming distance between the state $|z_j\rangle$ and the computational states involved in the SSE computation. The relevant number of terms of the aforementioned expansions as well as the computational time scale with n as $1/\Gamma \sim t_{\text{PT}}$, i.e., inversely proportional to the required precision.

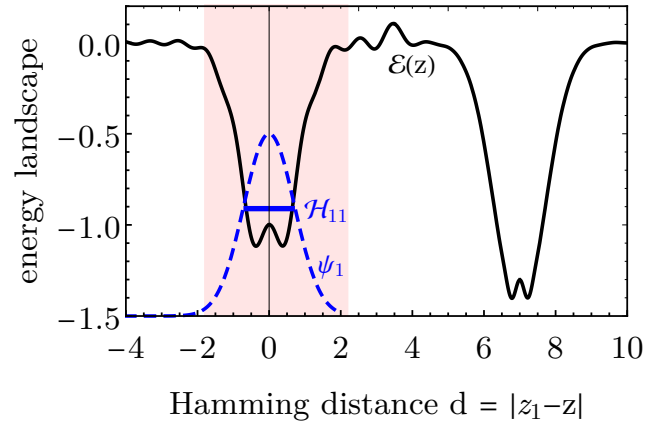


Figure 18. A cartoon depicting the energy landscape $\mathcal{E}(z)$ over the space of n -bit-strings z vs Hamming distance $d = |z - z_1|$ between z and a given marked state $|z_1\rangle$. The blue line shows the ground state energy level \mathcal{H}_{11} in one of the wells calculated without taking into account other deep minima. The dashed blue line depicts the wave-function for the eigenstate $\psi_1(z)$ that decays under the energy barrier and has a maximum at $z = z_1$ ($d = 0$). Light pink shading depicts the region of the landscape beyond which the effect of the tail of the wave-function on the value of \mathcal{H}_{11} is smaller than the given error threshold.

We note that for the bit-string z_i close to a local minimum of $\mathcal{E}(z)$, Quantum Monte Carlo (QMC) could simulate a tunneling transition away from z_i with the rate Q_{ij} that scales as $Q_{ij} \sim \mathcal{H}_{ij}^2$ [14, 15]. Therefore, from Eq.(175) we have $t_{\text{cl}}^{\text{QMC}} \propto t_{\text{pt}}^2$, which corresponds to a quadratic speedup of the quantum PT algorithm over QMC for this particular sampling task. In general, the states within the narrow energy belt $\Delta\mathcal{E}_{\text{cl}}$ are far away from the local minima and the QMC methods cannot be

³This can be done if the state $|z_j\rangle$ is sufficiently close in energy to the corresponding deep local minimum of $\mathcal{E}(z)$.

directly applied. In summary, we argue that coherent multi-qubit tunneling can be a powerful computational resource for solving PT problems with complicated energy landscapes.

We note that once a computational problem contains a structure, the associated minibands can be organized in a more complex way than in the IB model considered in our paper. E.g., the population transfer can proceed via the tree of resonances [36, 37]. The analysis of the computational complexity of the corresponding PT is referred to future studies.

XIII. CONCLUSION

Quantum tunneling has been proposed as a mechanism of efficient quantum search and optimization. However, Quantum Monte Carlo (QMC) can efficiently simulate tunneling transitions when the tunneling rate is dominated by a single path [14, 15], often described by an instanton calculus [67, 68].

We analyze the computational role of coherent multi-qubit tunneling that gives rise to bands of delocalized quantum states as a coherent pathway for population transfer (PT) between computational states with close energies. In this regime PT cannot be efficiently simulated by QMC.

We consider optimization problems with an energy function $\mathcal{E}(z)$ defined over the set of 2^n n -bit-strings z . We define a computational primitive with the objective to find bit-strings $z_j \neq z_i$ inside some narrow energy window $\Delta\mathcal{E}$ around the energy of the initial bit-string z_i . The problem is hard for sufficiently low starting energy $\mathcal{E}(z_i)$ in the region proliferated by deep local minima that are separated by large Hamming distances.

We propose to solve this problem using the following quantum population transfer (PT) protocol: prepare the system in a computational state $|z_j\rangle$ with classical energy $\mathcal{E}(z_j)$, then evolve it with the transverse-field quantum spin Hamiltonian. Classical energies $\mathcal{E}(z)$ are encoded in the problem Hamiltonian diagonal in the basis of states $|z\rangle$ similar to quantum annealing (QA) approaches [2–4]. A key difference from QA or analogue quantum search Hamiltonians [18, 56] is that the transverse field is kept constant throughout the algorithm and is not fine-tuned to any particular value. At the final moment of PT we projectively measure in the computational basis and check if the outcome z is a “solution”, i.e., $z \neq z_j$, and the energy $\mathcal{E}(z)$ is inside the window $\Delta\mathcal{E}_c$.

We study the Impurity Band (IB) model with a “bimodal” energy function. $\mathcal{E}(z) = 0$ for all states except for M “marked” states z_j picked at random with energies forming a narrow band of the width W separated by a large gap $\mathcal{O}(n)$ from the rest of the states. This landscape is similar to that in analogue Grover search [18, 51] with multiple target states and a distribution of oracle values for the targets. The best known classical algorithm for finding another marked state has cost $\mathcal{O}(2^n/M)$.

The transverse field gives rise to tunneling between a pair of marked states corresponding to a sum over a large number of virtual transitions connecting the two marked states via the states with $\mathcal{E}(z) = 0$. As a result the PT dynamics is described by the down-folded $M \times M$ Hamiltonian \mathcal{H} that is dense in the space of the marked states $|z_j\rangle$. Its off-diagonal matrix elements $\mathcal{H}_{ij} = V(d_{ij}) \cos \phi(d_{ij})$ are obtained using WKB method. They depend only on the Hamming distance d and have a form of decaying oscillations with phase $\phi(d)$ and amplitude $V(d) \propto \binom{n}{d}^{-1/2} \exp(-\frac{n}{4B_\perp^2})$. They are statistically independent with the typical value $V_{\text{typ}} = V(n/2)$.

We observed an interesting fact that PDF of the matrix elements has a heavy tail, decaying as a cubic power for $V(d) \gg V_{\text{typ}}$ despite the fact that matrix elements decrease very steeply with the Hamming distance d between the marked states. This happens because the total number of marked states $M_d \propto \binom{n}{d}$ (84) on a Hamming distance d from a given state grows rapidly with d . We emphasize that in finite dimensional systems polynomial tail of the PDF of matrix elements is only possible in the case of long-range interactions (e.g, dipolar glass). The above effect in our case is a result of the infinite dimension of the problem (in the $n \rightarrow \infty$ limit).

The diagonal elements coincide with classical energies $\mathcal{H}_{jj} = \mathcal{E}(z_j)$ and the dispersion is large, $W \sim V_{\text{typ}} M^{\gamma/2}$ with $\gamma \in [1, 2]$. Therefore we call \mathcal{H}_{ij} a Preferred Basis Levi matrix (PBLM). There exist two localization transitions in the PBLM ensemble, similar to the preferred basis Gaussian matrix ensemble, which is a so-called Rosenzweig-Porter (RP) model [33, 35].

We demonstrate that quantum PT finds another state within a target window of energies Ω in time $t_{\text{pt}} \propto 2^{n/2} \Omega^{-1/2} \exp(n/(2B_\perp^2))$. The scaling exponent of t_{pt} with n differs from that in Grover’s algorithm by a factor $\propto B_\perp^{-2}$, which can be made small with large transverse fields $n \gg B_\perp^2 \gg 1$.

Crucial distinctions between this case and the Hamiltonian in the analogue version of Grover’s algorithm [18] for the case of multiple target states are the non-integrability of our model, and the delocalized nature of the eigenstates within the energy band W . Furthermore, analogue Grover’s algorithm for multiple targets is exponentially sensitive in n to the weight of the driver Hamiltonian, and cannot be initialized with a computational basis state.

The locations of the localization transitions in our model are determined by the strong hierarchy of elements of the PBLM \mathcal{H}_{ij} . In the range $1 < \gamma < 2$ there exist minibands of non-ergodic delocalized eigenstates of \mathcal{H} . Their width is proportional to $1/t_{\text{pt}} \ll W$. Each miniband associated with a support set \mathcal{S} over the marked states. If $\gamma > 2$ then W exceeds the largest matrix element of \mathcal{H}_{ij} and the support set is empty, all eigenstates are localized. If $\gamma < 1$ then W is smaller than the typical largest element in a row of \mathcal{H}_{ij} and the support set extends to all marked states, – all eigenstates are “ergodic”.

Under certain conditions, PBLMs allow for minibands of non-ergodic delocalized states whose width is proportional to $1/t_{pt} \ll W$. This happens because the very steep decay of the off-diagonal matrix elements with the Hamming distance d between marked states is compensated by the steep increase in the number of neighbors at distance d .

We find the distribution of the miniband width $\Gamma = 1/t_{pt}$ analytically by solving the non-linear cavity equations for an ensemble of PBLMs. Unlike previous analyses focused on linearized cavity equations near the Anderson transition, we find the solution of the fully non-linear cavity equations in the non-ergodic delocalized phase.

The distribution of miniband widths Γ obeys alpha-stable Levy law with tail index 1. The typical value of Γ and its characteristic variance exceeds the typical matrix

element of \mathcal{H} by a factor $\Omega^{1/2}$ where $\Omega = (MV_{\text{typ}}/W)^2$ is a size of the support set in a typical miniband.

We provide qualitative arguments that our analysis of PT in IB model can be generalized to PT for sampling computation basis states within low-lying narrow energy bands of certain quantum spin glass models. We argue that coherent multi-qubit tunneling has a quantum advantage over QMC algorithms in those models.

ACKNOWLEDGMENTS

Authors are grateful to Edward Farhi, Christopher Laumann and Antonello Scardicchio for the fruitful discussions of this work.

-
- [1] L. K. Grover, “Quantum mechanics helps in searching for a needle in a haystack,” *Physical Review Letters*, vol. 79, no. 2, p. 325, 1997.
 - [2] T. Kadowaki and H. Nishimori, “Quantum annealing in the transverse ising model,” *Physical Review E*, vol. 58, no. 5, p. 5355, 1998.
 - [3] E. Farhi, J. Goldstone, S. Gutmann, J. Lapan, A. Lundgren, and D. Preda, “A quantum adiabatic evolution algorithm applied to random instances of an np-complete problem,” *Science*, vol. 292, no. 5516, pp. 472–475, 2001.
 - [4] J. Brooke, D. Bitko, G. Aeppli *et al.*, “Quantum annealing of a disordered magnet,” *Science*, vol. 284, no. 5415, pp. 779–781, 1999.
 - [5] V. N. Smelyanskiy, U. v. Toussaint, and D. A. Timucin, “Dynamics of quantum adiabatic evolution algorithm for number partitioning,” *arXiv preprint quant-ph/0202155*, 2002.
 - [6] S. Boixo, T. F. Rønnow, S. V. Isakov, Z. Wang, D. Wecker, D. A. Lidar, J. M. Martinis, and M. Troyer, “Evidence for quantum annealing with more than one hundred qubits,” *Nat. Phys.*, vol. 10, no. 3, pp. 218–224, Feb. 2014. [Online]. Available: <http://www.nature.com/doi/10.1038/nphys2900>
 - [7] S. Knysh, “Zero-temperature quantum annealing bottlenecks in the spin-glass phase,” *Nature communications*, vol. 7, p. 12370, 2016.
 - [8] S. Boixo, V. N. Smelyanskiy, A. Shabani, S. V. Isakov, M. Dykman, V. S. Denchev, M. H. Amin, A. Y. Smirnov, M. Mohseni, and H. Neven, “Computational multiqubit tunnelling in programmable quantum annealers,” *Nat. Comm.*, vol. 7, 2016.
 - [9] V. S. Denchev, S. Boixo, S. V. Isakov, N. Ding, R. Babush, V. Smelyanskiy, J. Martinis, and H. Neven, “What is the computational value of finite-range tunneling?” *Phys. Rev. X*, vol. 6, no. 3, p. 031015, 2016.
 - [10] T. Albash and D. A. Lidar, “Adiabatic quantum computation,” *Reviews of Modern Physics*, vol. 90, no. 1, p. 015002, 2018.
 - [11] E. Farhi, J. Goldstone, and S. Gutmann, “A quantum approximate optimization algorithm,” *arXiv preprint arXiv:1411.4028*, 2014.
 - [12] G. E. Santoro, R. Martonak, E. Tosatti, and R. Car, “Theory of quantum annealing of an Ising spin glass,” *Science*, vol. 295, no. 5564, pp. 2427–2430, Mar. 2002.
 - [13] B. Heim, T. F. Rønnow, S. V. Isakov, and M. Troyer, “Quantum versus classical annealing of ising spin glasses,” *Science*, vol. 348, no. 6231, pp. 215–217, 2015.
 - [14] S. V. Isakov, G. Mazzola, V. N. Smelyanskiy, Z. Jiang, S. Boixo, H. Neven, and M. Troyer, “Understanding quantum tunneling through quantum monte carlo simulations,” *Physical Review Letters*, vol. 117, no. 18, p. 180402, 2016.
 - [15] Z. Jiang, V. N. Smelyanskiy, S. V. Isakov, S. Boixo, G. Mazzola, M. Troyer, and H. Neven, “Scaling analysis and instantons for thermally assisted tunneling and quantum monte carlo simulations,” *Physical Review A*, vol. 95, no. 1, p. 012322, 2017.
 - [16] M. Mézard, G. Parisi, and M. Virasoro, *Spin glass theory and beyond: An Introduction to the Replica Method and Its Applications*. World Scientific Publishing Co Inc, 1987, vol. 9.
 - [17] Y. Fu and P. W. Anderson, “Application of statistical mechanics to np-complete problems in combinatorial optimisation,” in *Spin Glass Theory and Beyond: An Introduction to the Replica Method and Its Applications*. World Scientific, 1987, pp. 357–372.
 - [18] E. Farhi and S. Gutmann, “Analog analogue of a digital quantum computation,” *Physical Review A*, vol. 57, no. 4, p. 2403, 1998.
 - [19] H. Neven, “Enhancing simulated annealing with quantum annealing,” US Patent Application Publication PCT/US2016/068400, December 30, 2015. [Online]. Available: <https://patents.google.com/patent/WO2017117016A1>
 - [20] N. Chancellor, “Modernizing quantum annealing using local searches,” *New Journal of Physics*, vol. 19, no. 2, p. 023024, 2017.
 - [21] B. Altshuler, H. Krovi, and J. Roland, “Anderson localization makes adiabatic quantum optimization fail,” *Proceedings of the National Academy of Sciences*, vol. 107,

- no. 28, pp. 12 446–12 450, 2010.
- [22] P. W. Anderson, “Absence of diffusion in certain random lattices,” *Physical review*, vol. 109, no. 5, p. 1492, 1958.
 - [23] D. Basko, I. Aleiner, and B. Altshuler, “Metal–insulator transition in a weakly interacting many-electron system with localized single-particle states,” *Annals of physics*, vol. 321, no. 5, pp. 1126–1205, 2006.
 - [24] V. Oganesyan and D. A. Huse, “Localization of interacting fermions at high temperature,” *Physical Review B*, vol. 75, no. 15, p. 155111, 2007.
 - [25] S. Knysh and V. Smelyanskiy, “On the relevance of avoided crossings away from quantum critical point to the complexity of quantum adiabatic algorithm,” *arXiv preprint arXiv:1005.3011*, 2010.
 - [26] C. R. Laumann, A. Pal, and A. Scardicchio, “Many-body mobility edge in a mean-field quantum spin glass,” *Physical Review Letters*, vol. 113, no. 20, p. 200405, 2014.
 - [27] G. Mossi and A. Scardicchio, “Many body localization transition in quantum spin glasses on the bethe lattice,” *arXiv preprint arXiv:1703.03678*, 2017.
 - [28] B. I. Shklovskii and A. L. Efros, *Electronic properties of doped semiconductors*. Springer Science & Business Media, 2013, vol. 45.
 - [29] R. Abou-Chacra, D. Thouless, and P. Anderson, “A self-consistent theory of localization,” *Journal of Physics C: Solid State Physics*, vol. 6, no. 10, p. 1734, 1973.
 - [30] P. Cizeau and J.-P. Bouchaud, “Theory of lévy matrices,” *Physical Review E*, vol. 50, no. 3, p. 1810, 1994.
 - [31] F. L. Metz, I. Neri, and D. Bollé, “Localization transition in symmetric random matrices,” *Physical Review E*, vol. 82, no. 3, p. 031135, 2010.
 - [32] E. Tarquini, G. Biroli, and M. Tarzia, “Level statistics and localization transitions of lévy matrices,” *Physical Review Letters*, vol. 116, no. 1, p. 010601, 2016.
 - [33] D. Facchetti, P. Vivo, and G. Biroli, “From non-ergodic eigenvectors to local resolvent statistics and back: A random matrix perspective,” *EPL (Europhysics Letters)*, vol. 115, no. 4, p. 47003, 2016.
 - [34] C. Monthus, “Localization transition in random lévy matrices: multifractality of eigenvectors in the localized phase and at criticality,” *Journal of Statistical Mechanics: Theory and Experiment*, vol. 2016, no. 9, p. 093304, 2016.
 - [35] V. E. Kravtsov, I. M. Khaymovich, E. Cuevas, and M. Amini, “A random matrix model with localization and ergodic transitions,” *New Journal of Physics*, vol. 17, no. 12, p. 122002, 2015. [Online]. Available: <http://stacks.iop.org/1367-2630/17/i=12/a=122002>
 - [36] B. Altshuler, L. Ioffe, and V. Kravtsov, “Multifractal states in self-consistent theory of localization: analytical solution,” *arXiv preprint arXiv:1610.00758*, 2016.
 - [37] B. Altshuler, E. Cuevas, L. Ioffe, and V. Kravtsov, “Non-ergodic phases in strongly disordered random regular graphs,” *Physical Review Letters*, vol. 117, no. 15, p. 156601, 2016.
 - [38] N. Rosenzweig and C. E. Porter, “repulsion of energy levels” in complex atomic spectra,” *Physical Review*, vol. 120, no. 5, p. 1698, 1960.
 - [39] Z. Burda, J. Jurkiewicz, M. A. Nowak, G. Papp, and I. Zahed, “Free random lévy and wigner-lévy matrices,” *Physical Review E*, vol. 75, no. 5, p. 051126, 2007.
 - [40] B. Gnedenko and A. Kolmogorov, “Limit distributions for sums of independent,” *Am. J. Math.*, vol. 105, 1954.
 - [41] A. Garg, “Application of the discrete wentzel-kramers–brillouin method to spin tunneling,” *Journal of Mathematical Physics*, vol. 39, no. 10, pp. 5166–5179, 1998.
 - [42] A. Garg and M. Stone, “Bohr-sommerfeld quantization of spin hamiltonians,” *Physical Review Letters*, vol. 92, no. 1, p. 010401, 2004.
 - [43] M. Novaes and M. A. de Aguiar, “Semiclassical husimi functions for spin systems,” *Physical Review A*, vol. 71, no. 1, p. 012104, 2005.
 - [44] P. Braun, “Discrete semiclassical methods in the theory of rydberg atoms in external fields,” *Reviews of modern physics*, vol. 65, no. 1, p. 115, 1993.
 - [45] R. S. Varga, *Gershgorin and his circles*. Springer Science & Business Media, 2010, vol. 36.
 - [46] G. D. Mahan, *Many-particle physics*. Springer Science & Business Media, 2013.
 - [47] Wikipedia, *Stable Distribution*, https://en.wikipedia.org/wiki/Stable_distribution.
 - [48] J. Voit, *The statistical mechanics of financial markets*. Springer Science & Business Media, 2013.
 - [49] T. Rogers, I. P. Castillo, R. Kühn, and K. Takeda, “Cavity approach to the spectral density of sparse symmetric random matrices,” *Physical Review E*, vol. 78, no. 3, p. 031116, 2008.
 - [50] T. Tao, *Topics in random matrix theory*. American Mathematical Society Providence, RI, 2012, vol. 132.
 - [51] E. Farhi, J. Goldstone, S. Gutmann, and M. Sipser, “Quantum computation by adiabatic evolution,” *arXiv preprint quant-ph/0001106*, 2000.
 - [52] A. M. Childs, E. Deotto, E. Farhi, J. Goldstone, S. Gutmann, and A. J. Landahl, “Quantum search by measurement,” *Physical Review A*, vol. 66, no. 3, p. 032314, 2002.
 - [53] G.-L. Long, X. Li, and Y. Sun, “Phase matching condition for quantum search with a generalized initial state,” *Physics Letters A*, vol. 294, no. 3, pp. 143–152, 2002.
 - [54] N. Shenvi, K. R. Brown, and K. B. Whaley, “Effects of a random noisy oracle on search algorithm complexity,” *Physical Review A*, vol. 68, no. 5, p. 052313, 2003.
 - [55] E. Kogan, “On the analytic structure of green’s function for the fano-anderson model,” *arXiv preprint quant-ph/0611043*, 2006.
 - [56] A. M. Childs and J. Goldstone, “Spatial search by quantum walk,” *Physical Review A*, vol. 70, no. 2, p. 022314, 2004.
 - [57] A. De Luca, A. Scardicchio, V. E. Kravtsov, and B. L. Altshuler, “Support set of random wave-functions on the Bethe lattice,” *ArXiv e-prints*, Dec. 2014.
 - [58] Y. V. Fyodorov and A. D. Mirlin, “Localization in ensemble of sparse random matrices,” *Physical Review Letters*, vol. 67, no. 15, p. 2049, 1991.
 - [59] B. Derrida, “Random-energy model: An exactly solvable model of disordered systems,” *Physical Review B*, vol. 24, no. 5, p. 2613, 1981.
 - [60] T. Kirkpatrick and D. Thirumalai, “p-spin-interaction spin-glass models: Connections with the structural glass problem,” *Physical Review B*, vol. 36, no. 10, p. 5388, 1987.
 - [61] A. A. Abrikosov, L. P. Gorkov, I. E. Dzialochinski, D. Brown, and D. t. Haar, *Quantum field theoretical methods in statistical physics*. Pergamon Press, 1965.
 - [62] A. L. Fetter and J. D. Walecka, *Quantum theory of many-particle systems*. Courier Corporation, 2012.
 - [63] F. Pietracaprina, V. Ros, and A. Scardicchio, “Forward approximation as a mean-field approximation for the anderson and many-body localization transitions,” *Physical*

Review B, vol. 93, no. 5, p. 054201, 2016.

- [64] A. W. Sandvik, “Stochastic series expansion method with operator-loop update,” *Physical Review B*, vol. 59, no. 22, p. R14157, 1999.
- [65] A. Dorneich and M. Troyer, “Accessing the dynamics of large many-particle systems using the stochastic series expansion,” *Physical Review E*, vol. 64, no. 6, p. 066701, 2001.
- [66] T. Albash, G. Wagenbreth, and I. Hen, “Off-diagonal expansion quantum monte carlo,” *Physical Review E*, vol. 96, no. 6, p. 063309, 2017.
- [67] J. S. Langer, “Statistical theory of the decay of metastable states,” *Annals of Physics*, vol. 54, no. 2, pp. 258–275, 1969.
- [68] —, “Theory of the condensation point,” *Annals of Physics*, vol. 41, no. 1, pp. 108–157, 1967.

Appendix A: Matrix elements of the downfolded Hamiltonian and the normalization condition for its eigenvectors

We introduce eigenstates $|x\rangle$ of the transverse field (driver) Hamiltonian

$$H_D = -B_\perp \sum_{j=0}^n \sigma_j^x = \sum_{x \in \{0,1\}^n} H_D^x |x\rangle \langle x|, \quad (\text{A1})$$

Here

$$|x\rangle = |x^1\rangle \otimes \dots \otimes |x^n\rangle, \quad (\text{A2})$$

where $|x^k\rangle$ is the state of k th qubit such that $\sigma_x |x^k\rangle = (1 - 2x_k) |x^k\rangle$ and x -bits take values $x^k = 0, 1$. Also

$$H_D^x = -B_\perp (n - 2h_x), \quad h_x = \sum_{k=1}^n x^k, \quad (\text{A3})$$

where h_x is a Hamming weight of the bit-string x and $-B_\perp (n - 2h)$, $h \in (0, n)$ are eigenvalues of H_D .

We expand the eigenstates $|\psi\rangle$ of the system Hamiltonian H (2) into the basis of the eigenstates $|x\rangle$

$$|\psi\rangle = \sum_{x \in \{0,1\}^n} \Psi(x) |x\rangle. \quad (\text{A4})$$

We write the Schrodinger equation $H|\psi\rangle = E|\psi\rangle$ in the form

$$H_D |\psi\rangle + \sum_{j=1}^M \mathcal{E}(z_j) |z_j\rangle \psi(z_j) = E |\psi\rangle, \quad (\text{A5})$$

where $\psi(z_j) = \langle z_j | \psi \rangle$. Then we multiply it from the left by $\langle x |$ and obtain $\Psi(x)$ in terms of $\psi(z_j)$

$$\Psi(x) = \frac{\sum_{j=1}^M \mathcal{E}(z_j) v_{x,j} \psi(z_j)}{E - H_D^x}. \quad (\text{A6})$$

In Eq. (A6) the coefficients $v_{x,j} = \langle x | z_j \rangle$ equal

$$v_{x,j} = 2^{-n/2} (-1)^{x \cdot z_j}, \quad x \cdot z_j \equiv \sum_{k=1}^n x^k z_j^k, \quad (\text{A7})$$

and $z_j^k = 0, 1$.

We now multiply Eq. (A5) from the left by $\langle z_j |$ where $j \in (1, M)$ enumerates marked states and obtain

$$\sum_{x \in \{0,1\}^n} H_D^x \Psi(x) v_{x,j} = (E - \mathcal{E}(z_j)) \langle z_j | \psi \rangle. \quad (\text{A8})$$

Plugging here the expression for $\Psi(x)$ (A6) the matrix eigenvalue problem (A5) we obtain

$$\mathcal{E}(z_i) \psi(z_i) - \sum_{j=1}^M \mathcal{E}(z_j) c_{ij}(E) \psi(z_j) = E \psi(z_i) \quad (\text{A9})$$

where

$$c_{ij}(E) = \sum_{x \in \{0,1\}^n} v_{x,i} v_{x,j} \frac{H_D^x}{E - H_D^x}, \quad (\text{A10})$$

Because H_D^x depends on a bit-string x only via its Hamming weight $\sum_{j=1}^n x^j$ one can perform the partial summation in (A10) getting

$$c_{ij}(E) \equiv c(E, |z_i - z_j|), \quad |z_i - z_j| = \sum_{k=1}^n |z_i^k - z_j^k|, \quad (\text{A11})$$

where the function $c(E, d)$ has the form

$$c(E, d) = \sum_{k=0}^{n-d} \sum_{l=0}^d \binom{n}{k} \binom{n-d}{l} \frac{(-1)^l 2^{-n}}{1 + \frac{E}{B_\perp (n-2k-2l)}}. \quad (\text{A12})$$

Above $|z_i - z_j|$ denotes the Hamming distance between the bit-strings z_i and z_j . We introduce the rescaling

$$\psi(z_i) = \frac{A_i}{\sqrt{\mathcal{E}(z_i)}}, \quad i \in [1..M]. \quad (\text{A13})$$

Then Eq. (A9) can be written in the form

$$\sum_{j=1}^M \mathcal{H}_{ij}(E) A_j = E A_i, \quad (\text{A14})$$

where \mathcal{H}_{ij} is a symmetric $M \times M$ matrix

$$\mathcal{H}_{ij}(E) = \delta_{kj} \mathcal{E}(z_i) + \sqrt{\mathcal{E}(z_i) \mathcal{E}(z_j)} c(E, d_{ij}), \quad (\text{A15})$$

indices $k, j = 1:M$ and δ_{kj} is Kronecker delta. This is a nonlinear eigenproblem given in the main text, Eq. (15).

We note that the projections of the eigenvectors of H onto the marked state subspace are not, in general, normalized nor they are orthogonal. Let us consider the

eigenstate $|\psi_\beta\rangle$ and the corresponding eigenvalue E_β of H . We calculate the corresponding amplitude $\Psi_\beta(x)$ using Eq. (A6) and plug it into the normalization condition

$$\sum_{x \in \{0,1\}^n} \Psi_\beta^2(x) = 1, \quad (\text{A16})$$

obtaining after partial summation

$$\sum_{i,j=1}^M \mathcal{E}_i \mathcal{E}_j r(E_\beta, d_{ij}) \psi_\beta(z_i) \psi_\beta(z_j) = 1, \quad (\text{A17})$$

where the coefficient $r(E, d)$ equals

$$r(E, d) = 2^{-n} \sum_{k=0}^{n-d} \sum_{l=0}^d \frac{(-1)^k \binom{d}{k} \binom{n-d}{l}}{B_\perp (n - 2(k+l) + E)^2}. \quad (\text{A18})$$

It can be written in the form

$$r(E, d) = \frac{\partial}{\partial E} \left(\frac{c(E, d) - \delta_{d,0}}{E} \right), \quad (\text{A19})$$

where $\delta_{d,0}$ is the Kronecker delta. We use (A15) and write

$$r(E, d_{ij}) = \frac{1}{\sqrt{\mathcal{E}_i \mathcal{E}_j}} \frac{\partial \mathcal{H}_{ij}(E)}{\partial E}. \quad (\text{A20})$$

We now define the coefficients $Q_{ij}(E)$ such that

$$\frac{1}{Q_{ij}(E)} = \mathcal{E}_i \mathcal{E}_j r(E, d_{ij}) = \sqrt{\mathcal{E}_i \mathcal{E}_j} \frac{\partial \mathcal{H}_{ij}(E)}{\partial E}. \quad (\text{A21})$$

Then Eq.(A17) takes the form

$$\sum_{i,j} \frac{1}{Q_{ij}(E)} \psi_\beta(z_i) \psi_\beta(z_j) = 1. \quad (\text{A22})$$

The above equations (A21) and (A22) correspond to Eqs. (18) and (19) of the main text.

Appendix B: Details of the WKB analysis of the coupling coefficients

In the main text we expressed the coupling coefficient $c(E, d)$ in terms of the off-diagonal matrix elements of the resolvent (9) of the transverse field Hamiltonian H_D between the states that belong to a maximum total spin subspace $S = n/2$. The results are given in the expressions (26), (27) from the main text repeated below for convenience

$$c(E, d) = \delta_{d,0} - \frac{E}{\sqrt{\binom{n}{d}}} G_{\frac{n}{2}-d, \frac{n}{2}}(E). \quad (\text{B1})$$

Here the resolvent $G_{\frac{n}{2}-d, \frac{n}{2}}(E)$ obeys the inhomogeneous equation

$$\delta_{m, \frac{n}{2}} + \sum_{s=\pm 1} u(m - s/2) G_{m+s, \frac{n}{2}} = E G_{m, \frac{n}{2}}, \quad (\text{B2})$$

$$u(m) = -B_\perp \sqrt{L^2 - m^2}, \quad L = \frac{n+1}{2}. \quad (\text{B3})$$

We will solve the above equations for the case where the energy E of the resolvent is not far from the center of the Impurity Band

$$E = -n + \Delta, \quad \Delta = \mathcal{O}(n^0). \quad (\text{B4})$$

The WKB solution to Eq. (B2) is sought in the exponential form

$$G_{m, \frac{n}{2}} \propto \exp \left(i \int_0^m dk p(k) \right). \quad (\text{B5})$$

It is assumed that $\int_0^m dk p(k) = \mathcal{O}(n)$ and $|p(k)| = \mathcal{O}(n^0)$ so that $G_{m, \frac{n}{2}}$ is varying steeply with m changing by 1. However $|p'(m)| = \mathcal{O}(1/n)$ and $p(m)$ is varying very slowly with m due to the similar property of the coefficients $u(m)/L$ in the Eq. (B2). This property is at the root of WKB approximation [44]. The quantity p corresponds to the ‘‘momentum’’ of the effective mechanical system with coordinate m , energy E and Hamiltonian function $u(m) \cos p$. The function $p = p(E, m)$ is obtained from the equation

$$u(m) \cos p = E. \quad (\text{B6})$$

This equation also defines the curve on the (m, E) plane with $p = 0$ shown in Fig. 3. Points on that curve are turning points of the classical motion with energy E .

For not too small transverse fields

$$B_\perp > \frac{2L}{|E|} \simeq 1, \quad (\text{B7})$$

the Eq. (B6) has two types of WKB solutions that correspond to real or imaginary momentum $p(m)$ depending on the value of m relative to the turning points

$m = \pm m_0(E)$ given below⁴

$$m_0 = \sqrt{L^2 - \left(\frac{E}{2B_\perp}\right)^2}. \quad (\text{B8})$$

In the region

$$n/2 + m_0 > d > n/2 - m_0, \quad (\text{B9})$$

the amplitude $G_{\frac{n}{2}-d, \frac{n}{2}}$ (B5) is rapidly oscillating with d and can be written in the form

$$G_{\frac{n}{2}-d, \frac{n}{2}} = -\mathcal{C}(E) \frac{\sin \phi(E, d)}{[m_0^2(E) - (n/2 - d)^2]^{1/4}}, \quad (\text{B10})$$

where

$$\phi(E, d) = \int_{n/2-d}^{m_0} dk \arcsin \left(\sqrt{\frac{m_0^2 - k^2}{L^2 - k^2}} \right) - \frac{\pi}{4}, \quad (\text{B11})$$

is a phase of WKB solution and $\mathcal{C}(E)$ is the constant of integration that will be discussed below.

On the other hand, in the two regions

$$d \in [0, n/2 - m_0] \cup [n/2 + m_0, n] \quad (\text{B12})$$

the resolvent $G_{\frac{n}{2}-d, \frac{n}{2}}$ is decreasing exponentially with d . For example, in the left region

$$G_{\frac{n}{2}-d, \frac{n}{2}} = \frac{\mathcal{C}(E)}{2} \frac{e^{|\text{Im} \phi(E, d)|}}{[(n/2 - d)^2 - m_0^2(E)]^{1/4}}. \quad (\text{B13})$$

We omit here for brevity the expression in the right region (B12).

1. Determination of the integration constant in WKB solution

Within the WKB approach the integration constant $\mathcal{C}(E)$ can be obtained by matching the exponential asymptotic (B13) with the solution obtained near the boundary of the interval $d = 0$. However as discussed in Sec. VB of the main text, for the relevant range of the model parameters the properties of the typical sample in the ensemble of the IB Hamiltonians \mathcal{H} depend only on $G_{\frac{n}{2}-d, \frac{n}{2}}$ in the region of its oscillatory behavior (B9)

⁴The expression (B8) for $m_0(E)$ should be evaluated for the energy $E = E^{(0)} \simeq -n - B_\perp^2$ corresponding to the eigenvalues of impurity band (33),(35) In this case the $\mathcal{O}(n^0)$ corrections in the r.h.s. of (B8) vanishes.

$$m_0(E^{(0)}) \simeq \frac{n}{2} \sqrt{1 - B_\perp^{-2}} + \frac{1 - 3B_\perp^2}{4n\sqrt{1 - B_\perp^{-2}}}.$$

The terms $\mathcal{O}(1/n)$ above and can be neglected in the exponents of the WKB solutions (B10) and (B13).

away from the boundaries of the interval $d = 0, n$. To avoid the analysis in the region of no consequence for us we determine $\mathcal{C}(E)$ by equating the above WKB asymptotic for $G_{\frac{n}{2}-d, \frac{n}{2}}$ at the center of the interval $d = n/2$ with expression for $G_{0, \frac{n}{2}}$ at that point obtained in a different way.

Using Eq. (20) we write $c(E, n/2)$ in the integral form

$$c\left(E, \frac{n}{2}\right) = \frac{iE}{2^n B_\perp} \int_0^\infty d\tau (1 - e^{4i\tau})^{n/2} e^{i(E/B_\perp - n + i\sigma)\tau}$$

($\sigma \rightarrow +0$). The integral can be expressed in terms of the Gamma function $\Gamma(x)$. In the region of not too small transverse fields (B7) it has the form

$$c\left(E, \frac{n}{2}\right) = \frac{2^{1-n} \pi a (a^2 - 1)^{-1} \Gamma\left(\frac{n}{2}\right)}{\sin\left(\frac{\pi(a-1)n}{4a}\right) \Gamma\left(\frac{(a+1)n}{4a}\right) \Gamma\left(\frac{(a-1)n}{4a}\right)}. \quad (\text{B14})$$

where

$$a = -\frac{nB_\perp}{E} > 1. \quad (\text{B15})$$

Using Sterling formulae for Gamma function we obtain in the limit $n \gg 1$, $a = \mathcal{O}(n^0)$

$$c\left(E, \frac{n}{2}\right) = \frac{\sqrt{n\pi}}{2a \sin\left(\frac{\pi(a-1)n}{4a}\right)} 2^{-n/2} e^{-n\theta(a)}, \quad (\text{B16})$$

$$\theta(a) = \frac{2 \operatorname{arctanh}\left(\frac{1}{a}\right) + a \ln(1 - a^{-2})}{4a}. \quad (\text{B17})$$

For large transverse fields $a \gg 1$ and we have $\theta \simeq a^2/4$.

Using Eq. (B1) we obtain the asymptotic of the Green function at the zone center

$$G_{0, \frac{n}{2}}(E) = \left(\frac{\pi}{8n^3}\right)^{1/4} \frac{\exp(-n\theta(a))}{\sqrt{B_\perp^2 - 1} \sin \phi(n/2, E)}. \quad (\text{B18})$$

Here we used the equality for the phase WKB $\phi(E, n/2)$ (B11) at the zone center

$$\phi(E, n/2) = \pi \frac{(a-1)n}{4a}. \quad (\text{B19})$$

On the other hand, from the WKB expression (B10) we get

$$G_{0, \frac{n}{2}} = -\mathcal{C}(E) \left(\frac{2}{n}\right)^{1/2} \frac{\sin \phi(E, n/2)}{(1 - B_\perp^{-2})^{1/4}}. \quad (\text{B20})$$

By comparing the Eqs. (B18) and (B20) we finally obtain the constant of integration $\mathcal{C}(E)$

$$\mathcal{C}(E) = -\frac{\pi^{1/4}}{(32nB_\perp^2(B_\perp^2 - 1)^{1/4} (\sin \phi(E, n/2))^2} \exp(-n\theta(a)). \quad (\text{B21})$$

One can use (B21) in (B10) and (26) to obtain the expression for $c(E, d)$ in the region (B9). Before providing

the result we observe that for energies E not too far from the Impurity Band center (cf. Eq. (B4)) the expression for $n\theta(a)$ can be expanded in powers of $1/n$

$$n\theta(a) \simeq n\theta(B_\perp) - \frac{E+n}{2B_\perp} \operatorname{arccoth} B_\perp + \mathcal{O}(n^{-1}). \quad (\text{B22})$$

where $E+n \equiv \Delta = \mathcal{O}(n^0)$.

Finally the expression for the coupling coefficient has the form

$$c(E, d) = \sqrt{A(E, d/n)} \frac{n^{\frac{1}{4}} e^{-n\theta(B_\perp)}}{\sqrt{\binom{n}{d}}} \times \sqrt{2} \sin \phi(E, d), \quad (\text{B23})$$

where the WKB phase $\phi(E, d)$ is given in (B11) and the coefficient $A(E, \rho)$ equals

$$A(E, \rho) = \sqrt{\frac{\pi}{32}} \frac{e^{\frac{E+n}{B_\perp} \operatorname{arccoth} B_\perp}}{(B_\perp^2 - 1)v(\rho) \sin^4(\phi(E, n/2))}, \quad (\text{B24})$$

$$v(\rho) = \left(1 - \frac{(1-2\rho)^2}{1-B_\perp^{-2}}\right)^{1/2}, \quad (\text{B25})$$

It is related to $A(\rho)$ in the Eq. (42) of the main text as follows: $A(\rho) = A(E^{(0)}, \rho)$. The phase $\phi(E, n/2)$ in (B24) has an explicit form

$$\phi(E, n/2) = \frac{\pi}{4} \left(n(1 - B_\perp^{-1}) + \frac{n+E}{B_\perp} \right). \quad (\text{B26})$$

2. Limit of large transverse fields $B_\perp \gg 1$

In the limit of large transverse fields the tuning point m_0 (B8) is very close to the boundary of the interval $m = L$ so that one has a small parameter

$$\sqrt{\frac{L - m_0}{L}} = \frac{1}{\sqrt{8}} \frac{|E|}{LB_\perp} \ll 1 \quad (\text{B27})$$

In this case the expression for the WKB phase takes a simple form

$$\phi(E, d) = \frac{\pi d}{2} - \frac{\pi n}{4} \frac{\chi(E, d/n)}{B_\perp}, \quad (\text{B28})$$

$$\chi(E, \rho) = \left(1 - \frac{\Delta}{n}\right) \left(1 - \frac{2}{\pi} \tan^{-1} \frac{1-2\rho}{\sqrt{1-(1-2\rho)^2}}\right)$$

where $\Delta = E+n = \mathcal{O}(n^0)$ and values of d are not too close to the interval boundaries

$$n-d, d \gg L - m_0 \sim \frac{n}{B_\perp^2}. \quad (\text{B29})$$

We note that for large transverse fields $B_\perp \gg 1$ the phase is a sum of the two terms. First term changes rapidly with d with the slope $\pi/2$ and second term changes very little (by an amount $\mathcal{O}(n^{-1})$) when d is changed by 1.

We note that unlike the study of the WKB eigenfunctions where one has to select the WKB solution that decays into the classically forbidden region (B12), the Green function $G_{n/2-d, n/2}(E)$ corresponds to the solution that *increases* exponentially with $m = n/2 - d > m_0$. Using the oscillating (B10) and exponentially growing (B13) WKB solutions one can obtain the coefficient $c(E, d)$ from the relation (26). This will provide an asymptotic WKB form of $c(E, d)$ almost everywhere on the interval $d \in [0, n]$ except for the small vicinities of the turning points, $|n/2 - m_0(E) - d| = \mathcal{O}(n^0)$ and end points, $n-d, d = \mathcal{O}(n^0)$. In Fig. 4 we plot the comparison between the coefficients $c(E, d)$ computed based on exact expression (20) and the results of asymptotic WKB analysis using Eqs. (B10), (B13).

Appendix C: Linearization of the down-folded Hamiltonian near the center of the Impurity Band

We divide the Hamiltonian $\mathcal{H}(E)$ for a given E on two parts, accordingly

$$\mathcal{H}_{ij}(E) = \mathcal{H}_{ij}^{(0)}(E) + \mathcal{H}_{ij}^{(1)}(E), \quad (\text{C1})$$

where we defined

$$\mathcal{H}_{ij}^{(0)}(E) = n(c(E, 0) - 1) \delta_{ij}, \quad (\text{C2})$$

$$\mathcal{H}_{ij}^{(1)}(E) = \delta_{ij}(1 - c(E, 0))\epsilon_i + nc(E, d_{ij})(1 - \delta_{ij}). \quad (\text{C3})$$

We write similar expansions for energies and amplitudes

$$E \approx E^{(0)} + E^{(1)}, \quad \psi(z_j) \approx \psi^{(0)}(z_j) + \psi^{(1)}(z_j), \quad (\text{C4})$$

and get

$$\mathcal{H}(E) \approx \mathcal{H}^{(0)}(E^{(0)}) + \frac{\mathcal{H}^{(0)}(E^{(0)})}{\partial E} E^{(1)} + \mathcal{H}^{(1)}(E^{(0)}),$$

where the parts of the Hamiltonian $\mathcal{H}^{(0,1)}$ are given above. We plug the above expansions into the system of equations (14) $\sum_{j=1}^M \mathcal{H}_{ij}(E) \mathcal{A}_j = E \mathcal{A}_i$, and use (A13) to express $\mathcal{A}_j^{(0)} = n^{1/2} \psi^{(0)}(z_j)$. Equating terms of the same order in ϵ_j and $c(E, d_{ij})$, $i \neq j$, we obtain the equation for eigenstates and eigenvalues in zeroth order

$$n[c(E^{(0)}, 0) - 1] \psi^{(0)}(z_j) = E^{(0)} \psi^{(0)}(z_j), \quad (\text{C5})$$

$j \in [1..M]$, and in the first order

$$\begin{aligned} a \epsilon_i \psi^{(0)}(z_j) + b \sum_{j \neq i=1}^M n c(E^{(0)}, d_{ij}) \psi^{(0)}(z_j) \\ = E^{(1)} \psi^{(0)}(z_j) \end{aligned} \quad (C6)$$

Above index j enumerates marked states. Also the coefficients a, b equal

$$a = b(1 - c(E^{(0)}, 0)), \quad b^{-1} = 1 - n \frac{\partial c(E^{(0)}, 0)}{\partial E}. \quad (C7)$$

Similarly to the above we find from Eqs. (18),(19) the zeroth-order approximation to the the total probabilistic weight of an eigenfunctions $|\psi\rangle$ over the marked state subspace $Q_{jk}^{(0)} = \delta_{jk} Q$ where

$$Q_{jk}^{(0)} = \delta_{jk} Q, \quad \frac{1}{Q} = n^2 \frac{\partial}{\partial E} \left(\frac{c(E, 0) - 1}{E} \right)_{E=E^{(0)}}. \quad (C8)$$

a. Zeroth-order of the perturbation theory

Eq. (C5) admits the solution corresponding to the M -fold degenerate energy level that originates from the band of the marked states, $E^{(0)} \rightarrow -n$ in the limit of $B_\perp \rightarrow 0$. The corresponding M eigenstates $\psi_\beta(z_j)$ ($\beta \in [1..M]$) have support over the part of computational basis corresponding to marked states: $\psi_{z_j}^\beta \neq 0$, $j \in (1, M)$. Using $c(E, 0)$ from (C16) the explicit form of the equation (C5) for eigenvalue in zeroth order is given in the main text, Eqs. (33),(34) which we repeat here for convenience.

$$E^{(0)} = -n - \Delta_0, \quad (C9)$$

$$\Delta_0 = n 2^{-n} \sum_{d=0}^n \binom{n}{d} \frac{B_\perp (n - 2d)}{n + \Delta_0 - B_\perp (n - 2d)}. \quad (C10)$$

Here Δ_0 is the root of the above transcendental equation that satisfies the condition $\lim_{B_\perp \rightarrow 0} \Delta_0 = 0$. In general, the sum (34) is dominated by the region of values of d such that $|d - n/2| = \mathcal{O}(n^{1/2})$. We obtain Δ_0 in a form of a series expansion in powers of n^{-1}

$$\Delta_0 \simeq -B_\perp^2 - \frac{B_\perp^4}{n} + \mathcal{O}(n^{-2}), \quad (C11)$$

Similarly, using $c(E, 0)$ from (20) in the equation (C8) for the zeroth-order total weight over the marked state subspace we obtain

$$\sum_{k=1}^M |\psi_{z_k}^{(0)}|^2 = Q,$$

$$\frac{1}{Q} = \frac{1}{2^n} \sum_{d=0}^n \binom{n}{d} \frac{1}{(B_\perp (n - 2d) - n - \Delta_0)^2}. \quad (C12)$$

Using (35) and employing similar approximations to that from the above we get an asymptotical expression in large n limit

$$Q \simeq 1 - \frac{B_\perp^2}{n} - \frac{3B_\perp^4}{n^2} + \mathcal{O}(n^{-3}). \quad (C13)$$

We recall that in our study n is asymptotically large and we always assume that the transverse field $B_\perp = \mathcal{O}(n^0)$ (but can be parametrically large, $B_\perp \gg 1$).

The denominator in Eqs. (C10),(C12) corresponding to $d = m$ will become zero at “resonant” transverse field value $B_\perp = B_{\perp m}$ which is a root of the equation (37) in the main text. In the range of B_\perp under consideration $n/2 - m \gg n^{1/2}$.

Near the m th resonance the term with $d = m$ in the sum (34) becomes anomalously large due to a small denominator despite the factor p_m being very small. We keep this term (34) along with the terms corresponding to $|n/2 - d| \sim n^{1/2}$ and obtain

$$\Delta_0 \simeq \frac{\delta_B}{2} \pm \sqrt{\frac{\delta_B^2}{4} + n^2 p_m}, \quad (C14)$$

where we introduced rescaled transverse field difference from its value at resonance

$$\delta_B = n \frac{B_\perp - B_{\perp m}}{B_{\perp m}^{(0)}}, \quad (C15)$$

where $B_{\perp m}^{(0)} = n/(n - 2m)$.

Clearly, in the resonance region $\delta_B \sim n p_m^{1/2}$ and $|B_\perp - B_{\perp m}| \sim \Delta B_{\perp m}$ where $\Delta B_{\perp m} \sim 2^{-n/2} \binom{n}{m} B_{\perp m}^{(0)}$. There the weight factor Q is decreasing dramatically (cf. Fig. 7) and the above perturbation theory breaks down. The width of the resonant regions $\Delta B_{\perp m}$ (38) remains exponentially small in n for $n/2 - m \gg n^{1/2}$.

In this study we will only focus on the off-resonance case, assuming the condition

$$\Delta B_{\perp m} \ll |B_{\perp m} - B_\perp| \sim |B_{\perp m+1} - B_\perp| = \mathcal{O}(B_\perp).$$

b. First order of the perturbation theory

The first order equation (C6) determines the correct zeroth order eigenstates $\{\psi_\beta(z_j)\}_{\beta=1}^M$ and removes the degeneracy of the energy levels. To evaluate the coefficients a, b in (C6) we calculate $c(E, 0)$ away from resonance using the same approach as that in the evaluation of the sum in (34)

$$c(E, 0) \simeq -\frac{n B_\perp^2}{E^2} + \mathcal{O}\left(\frac{n^2 B_\perp^4}{E^4}\right). \quad (C16)$$

The coefficients $a, b \simeq 1 + \mathcal{O}(B_{\perp}^2/n)$ and in what following will be replaced by unity. Then Eq. (C6) corresponds to the effective Hamiltonian \mathcal{H} with the matrix elements, $\mathcal{H}_{ii} = \epsilon_i$ and $\mathcal{H}_{ij \neq i} = nc(E^{(0)}, d_{ij})$ where coupling coefficients c are given in (30). Using Eqs. (33), (34) for zeroth-order energy $E^{(0)}$, the matrix \mathcal{H}_{ij} can be written in the form (40).

Appendix D: PDF of the squared off-diagonal matrix elements of impurity band Hamiltonian

In this section we provide the details of the derivation of the PDF for the non-oscillatory parts of the (squared) off-diagonal matrix elements \mathcal{V}_{ij}^2 of the IB Hamiltonian. As discussed in the main text, in the asymptotical limit of large $n \gg 1$ one can make an approximation that n is a continuous variable and we replace the summation over d in (52) by an integral and Kronecker delta $\delta(x)$ by Dirac delta. This results in the Eq. (64) displayed below for convenience

$$P(\mathcal{V}_{ij}^2) = \int_0^n p_x \delta(V^2(x) - \mathcal{V}_{ij}^2) dx. \quad (\text{D1})$$

It was discussed in the main text (see also below) that the condition for this validity of this approximation is

$$\frac{1}{n} \log_2 M \ll 1. \quad (\text{D2})$$

It corresponds to the number of marked states M that is not very large. For example, it can still scale exponentially with n so that $M = 2^{\mu n}$, $\mu = \mathcal{O}(n^0)$, but the coefficient μ in the exponent needs to be small $\mu \ll 1$.

The expression (D1) is obtained using the analytical continuation p_x of the binomial distribution p_d (49) from the integer domain $d \in [0, n]$ onto the interval of a real axis $x \in [0, n]$ in terms of the Beta function $B(x, y)$

$$p_x = 2^{-n} \binom{n}{x} = \frac{2^{-n}}{(n+1)B(x+1, n+1-x)}, \quad (\text{D3})$$

and the resulting identity

$$\int_0^n dx p_x = 1. \quad (\text{D4})$$

In what following we will study the rescaled quantities

$$w_{ij} \equiv \frac{\mathcal{V}_{ij}^2}{V_{\text{typ}}^2} = \left(\frac{2}{\pi n} \right)^{1/2} \frac{1}{p_{d_{ij}}}, \quad (\text{D5})$$

where $i \neq j$, V_{typ} is given in (53) and $p_d = 2^{-n} \binom{n}{d}$. Using Stirling's approximation in binomial coefficient

$$p_x \equiv p_B(x/n), \quad p_B(\rho) = \frac{e^{-n\mathcal{A}(\rho)}}{\sqrt{2\pi n\rho(1-\rho)}}. \quad (\text{D6a})$$

$$\mathcal{A}(\rho) = \rho \log \rho + (1-\rho) \log(1-\rho) + \log 2. \quad (\text{D6b})$$

we get from Eq. (41) for $\mathcal{V}_{ij} = V(d_{ij})$

$$w(\rho) \equiv \frac{V^2(n\rho)}{V_{\text{typ}}^2} \simeq \frac{\sqrt{4\rho(1-\rho)}}{v(\rho)} e^{n\mathcal{A}(\rho)}, \quad (\text{D7})$$

where $v(\rho)$ is given in (43). Eq. (D5) takes the form

$$w_{ij} = w(d_{ij}/n). \quad (\text{D8})$$

Then the expression for the PDF for w_{ij}

$$g(w_{ij}) = V_{\text{typ}}^2 P(V_{\text{typ}}^2 w_{ij}), \quad (\text{D9})$$

can be written in the form (cf. (D1))

$$g(w) = 2n \int_0^{1/2} p_B(\rho) \delta(w - w(\rho)) d\rho. \quad (\text{D10})$$

We note that the domain of $g(w)$ is bounded from below by $w = 1$ and from above by $w = \mathcal{O}(2^n)$. Taking the integral in (D10) we get

$$g(w) = 2n \frac{p_B(\rho_w)}{\left| \frac{dw(\rho)}{d\rho} \right|_{\rho=\rho_w}}, \quad (\text{D11})$$

where the rescaled Hamming distance ρ_w is a root of the transcendental equation

$$w(\rho_w) = w. \quad (\text{D12})$$

In the leading order in $n \gg 1$ this equation gives

$$\mathcal{A}(\rho_w) = \frac{1}{n} \log w, \quad (\text{D13})$$

where $\mathcal{A}(\rho)$ is given in (D6b). Also using Eqs. (D6), (D7) in (D11) we get

$$g(w) = \frac{1}{w^2 \sqrt{\pi \ell(w)}}, \quad (\text{D14})$$

where

$$\ell(w) = \frac{n}{8} v^2(\rho_w) |\log(\rho_w^{-1} - 1)|^2 \quad (\text{D15})$$

Here the dependence of $\ell(w)$ on w is shown in Fig. 19. In the entire range the dependence is logarithmically slow.

We note that the (D13) is a valid approximation to (D12) for $\rho - \rho_0 \gg 1/n$ where ρ_0 is a zero of $v(\rho)$

$$v(\rho_0) = 0, \quad \rho_0 = \frac{1}{1 - \sqrt{1 - B_{\perp}^{-2}}} \quad (\text{D16})$$

It corresponds to Hamming distance $n\rho_0 = n/2 - m_0$ (29) which lies at the boundary of the interval (B9) where the WKB solution (30), (41) applies (see the discussion in

the Sec. III). It is assumed that $n\rho_0$ is smaller than the typical smallest Hamming distance d_{\min} in a randomly selected row

$$d_{\min} - n\rho_0 \gg 1. \quad (\text{D17})$$

Using the asymptotic expression (D6) for the binomial distribution in Eqs. (54) we get the equation for d_{\min} in the form

$$\mathcal{A}(d_{\min}/n) = \frac{1}{n} \log M \quad (\text{D18})$$

The function $\mathcal{A}(\rho)$ is decreasing with ρ for $\rho(0, 1/2)$. Therefore Eq. (D17) leads to the condition $\mathcal{A}(\rho_0) - \mathcal{A}(d_{\min}/n) \gg 1/n$, or

$$\mathcal{A}(\rho_0) - \frac{1}{n} \log M \gg \frac{1}{n}. \quad (\text{D19})$$

Using explicit forms of $\mathcal{A}(\rho)$ and ρ_0 we get in the limit of $B_{\perp} \gg 1$

$$\log 2 - \frac{1}{n} \log M > \frac{2 \log B_{\perp} + 2 \log 2 + 1}{4B_{\perp}^2} + \varepsilon$$

$$0 < \varepsilon = \mathcal{O}(B_{\perp}^{-4}). \quad (\text{D20})$$

This is the condition for (D17). Clearly it corresponds to a much weaker constraint on the values of M than the condition $\frac{1}{n} \log M < \frac{1}{2} \log 2$ provided by the requirement of a statistical independence of matrix elements of \mathcal{V}_{ij} (cf. (50)).

a. Case of $\frac{1}{n} \log_2 M \ll 1$

The rescaled Hamming distance ρ_w depends on w via the logarithmic factor $\alpha = \frac{1}{n} \log_2 w$. This dependence is shown in the inset to the Fig. 19. In this section we consider

$$\alpha = \frac{1}{n} \log_2 w \ll 1. \quad (\text{D21})$$

Then we get

$$p_B(\rho) \simeq \left(\frac{2}{\pi n} \right)^{1/2} e^{-n\mathcal{A}(\rho)}, \quad (\text{D22})$$

$$\mathcal{A}(\rho) \simeq 2 \left(\frac{1}{2} - \rho \right)^2.$$

Then using (D13) we get

$$\rho_w \simeq \frac{1}{2} - \left(\frac{\alpha}{2} \right)^{1/2}. \quad (\text{D23})$$

$$\ell(w) \simeq \log w, \quad (\text{D24})$$

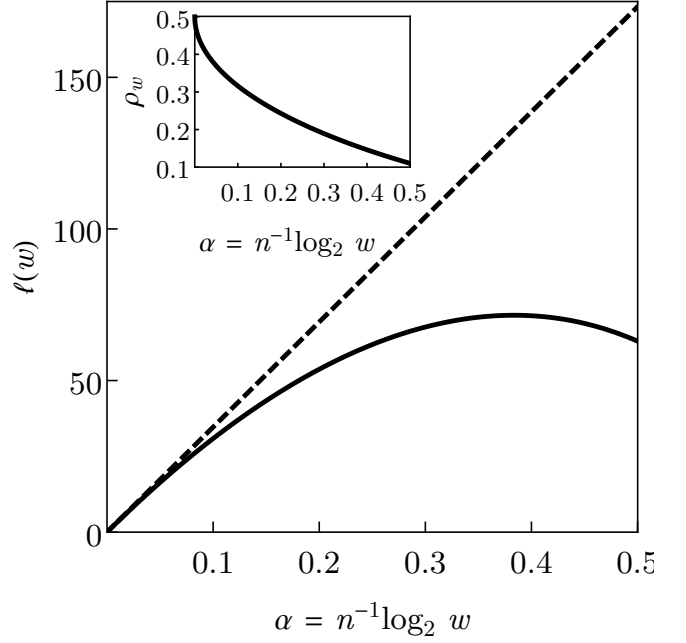


Figure 19. Solid line shows the dependence of $\ell(w)$ on $\alpha = \frac{1}{n} \log_2 w$ from Eq. (D15). Dashed line shows the tangent to the solid curve at the point $\alpha = 0$ ($w = 1$). This line corresponds to $\ell(w) \simeq \sqrt{\log w}$, in accordance with (D24). Inset shows the dependence of the root ρ_w of the equation (D12) on $\alpha = \log_2 w^{1/n}$. Small $\alpha \ll 1$ corresponds to Hamming distances $\rho_w \approx 1/2$. Near that point the dependence of ρ_w on α follows (D23).

and finally,

$$g(w) \simeq g_{\infty}(w) = \frac{1}{w^2 \sqrt{\pi \log w}}. \quad (\text{D25})$$

The subscript here indicates that, unlike $g(w)$, the PDF $g_{\infty}(w)$ has the upper boundary of its domain equal to infinity. It is of interest to calculate for a given w the magnitude of the relative changes of $V^2(d)$ and of the binomial coefficient p_d when Hamming distance is changing by 1 (and ρ_w is changing by $1/n$). We define as in Eqs. (D8),(D7) $w = V^2(d)/V_{\text{typ}}^2$ and obtain

$$\frac{V^2(d+1) - V^2(d)}{V^2(d)} \simeq \frac{p_{d+1} - p_d}{p_d} \quad (\text{D26})$$

$$\simeq 4 \left(\frac{1}{2} - \rho_w \right) = \sqrt{8\alpha} \ll 1. \quad (\text{D27})$$

Here we used Eqs. (D23) and (D21). The above inequality justifies using the continuous approximation (D1) in (52).

In a randomly chosen row of w_{ij} the PDF that the largest element equals w is

$$\text{PDF}(\max_m w_m = w) \simeq \frac{M e^{-M w \log w}}{w \log w}, \quad M \gg 1. \quad (\text{D28})$$

Typical largest element in a row $\max_{1 \leq j \leq i} w_{ij} \sim M$ in agreement with the results obtained earlier, cf. Eqs. (41), (54) and (D5). Therefore in order to ensure that $\alpha \ll 1$ for all matrix elements in a typical row of w_{ij} we require that $\log_2 M \ll n$

$$1 \leq w \lesssim M, \quad \frac{1}{n} \log_2 M \ll 1. \quad (\text{D29})$$

The typical value of the smallest element in a randomly selected row of the rescaled matrix of Hamming distances d_{ij}/n equals

$$\rho_{\min} = \frac{d_{\min}}{n} = \frac{1}{2} - \sqrt{\frac{\log_2 M}{2n}}. \quad (\text{D30})$$

We note that in the case we consider

$$n \gg n/2 - d_{\min} = \mathcal{O}(n), \quad (\text{D31})$$

minimum value d_{\min} is close to $n/2$ but is still separated by extensive distance from it.

In this paper we use the expression for the matrix elements of the IB Hamiltonian \mathcal{H}_{ij} (40) that only applies in the region $|n/2 - d_{ij}| < m_0$ where m_0 is given in (29). The elements in a typical row of the matrix d_{ij} belong to this region if the condition $|n/2 - d_{\min}| < m_0$ is fulfilled. Using (D30) we can re-write this as an inequality for M

$$M < 2^{\frac{n}{2}(1-B_1^{-2})}. \quad (\text{D32})$$

This inequality is satisfied under the condition (D29).

Appendix E: Characteristic function of the PDF of the squared off-diagonal matrix elements of impurity band Hamiltonian

Here we compute the characteristic function of the PDF $g_\infty(w)$ (D25) (also given in Eq. (69) of the main text). It is defined as follows

$$\phi_\infty(u) = \int_1^\infty dw g_\infty(w)(e^{i u w} - 1). \quad (\text{E1})$$

We will be interested in the asymptotic limit of the above expression at small $|u| \ll 1$. It is convenient to calculate separately real and imaginary parts of $\phi_\infty(u)$.

For real part we have

$$-\frac{\sqrt{\pi}}{2} \text{Re}[\phi_\infty(u)] = \int_1^\infty \frac{1}{x^2 \sqrt{\log x}} \sin^2\left(\frac{ux}{2}\right) dx. \quad (\text{E2})$$

Because $\phi_\infty(-u) = \phi_\infty^*(u)$ we can assume that $u > 0$ and break the interval of integration above on two parts

$$x \in [1, X/u] \cup [X/u, \infty), \quad u \ll X \ll 1. \quad (\text{E3})$$

We write

$$-\frac{\sqrt{\pi}}{2} \text{Re}[\phi_\infty(u)] = R_1(u) + R_2(u). \quad (\text{E4})$$

Here

$$R_1(u) = \int_1^{X/u} \frac{1}{x^2 \sqrt{\log x}} \sin^2\left(\frac{ux}{2}\right) dx, \quad (\text{E5})$$

$$R_2(u) = \int_{X/u}^\infty \frac{1}{x^2 \sqrt{\log x}} \sin^2\left(\frac{ux}{2}\right) dx. \quad (\text{E6})$$

Using (E3) asymptotic expansion of $R_1(u)$ has the form

$$R_1(u) \simeq \frac{u X}{4(\log(1/u))^{1/2}} + \frac{u X \log(1/X)}{8(\log(1/u))^{3/2}} + \dots \quad (\text{E7})$$

Also after some tedious calculations we obtain

$$R_2(u) \simeq \frac{u}{(\log(1/u))^{1/2}} \left(\frac{\pi}{4} - \frac{X}{4} \right) + \frac{u}{2(\log(1/u))^{3/2}} \frac{\pi(\gamma_{\text{Euler}} - 1)}{4}. \quad (\text{E8})$$

where

$$\gamma_{\text{Euler}} \simeq 0.577 \quad (\text{E9})$$

is the Euler constant.

Similarly to the above we also break the interval of integration in the imaginary part of $\phi_\infty(u)$ on two parts given in (E3)

$$\text{Im}[\phi_\infty(u)] = I_1(u) + I_2(u). \quad (\text{E10})$$

where

$$I_1(u) = \int_1^{X/u} \frac{\sin ux}{x^2 \sqrt{\pi \log x}} dx, \quad (\text{E11})$$

$$I_2(u) = \int_{X/u}^\infty \frac{\sin ux}{x^2 \sqrt{\pi \log x}} dx. \quad (\text{E12})$$

Expanding the integrand (E11) in u and using condition (E3) we get

$$I_1(u) \simeq \frac{2u \sqrt{\log \frac{1}{|u|}}}{\sqrt{\pi}} - \frac{u \log \frac{1}{X}}{\sqrt{\pi \log \frac{1}{|u|}}} + \mathcal{O}\left(\frac{u \log^2 X}{\log^{3/2} |u|}\right).$$

Performing similar asymptotic expansion in $I_2(u)$ we obtain

$$I_2(u) \simeq \frac{u(1 - \gamma_{\text{Euler}} - \log X)}{\sqrt{\pi \log \frac{1}{|u|}}} + \mathcal{O}\left(\frac{u \log^2 X}{\log^{3/2} u}\right).$$

Finally, we combine together Eqs. (E7),(E8) into Eq. (E4) to obtain first two terms in the asymptotic expansion of $\text{Re}[\phi_\infty(u)]$ in powers of $1/\log u \ll 1$

$$\text{Re}[\phi_\infty(u)] = -\frac{|u|\sqrt{\pi}}{2\sqrt{\log|u|^{-1}}} \left(1 - \frac{1 - \gamma_{\text{Euler}}}{2\log|u|^{-1}}\right). \quad (\text{E13})$$

We also combine together the above expressions for I_1 and I_2 to obtain a similar asymptotic expansion of $\text{Im}[\phi_\infty(u)]$

$$\text{Im}[\phi_\infty(u)] \simeq \frac{2u\sqrt{\log\frac{1}{|u|}}}{\sqrt{\pi}} + \frac{u(1 - \gamma_{\text{Euler}})}{\sqrt{\pi \log\frac{1}{|u|}}}. \quad (\text{E14})$$

Note that in both cases the terms involving X cancels out confirming the validity of the matching procedures.

Appendix F: Generalized Central Limit Theorem for the sum of M random variables w_m that obey the distribution $g_\infty(w)$

In this section we will study the asymptotic PDF for the sum of the independent identically distributed random variables in Eq. (92) sampled from the probability distribution (D25). We note that the variance of the random variables does not exist. The PDFs with polynomial tails at infinity are known as Pareto (heavy-tailed) distributions. According to the Generalized Central Limit Theorem (GCLT), the PDF of the sum of M Pareto variables for $M \rightarrow \infty$ approaches its asymptotic form given by the stable law [40]. This general property coincides with the usual Central Limit Theorem for the case when random variables in a sum have finite variances. In this case the limiting PDF has Gaussian form.

We note that the PDF given by Eq. (D25) is not strictly polynomial at $w \rightarrow \infty$ because of the additional logarithmic factor. We will derive the asymptotic form of the sum (92) of random variables (D25) explicitly and compare with the standard GCLT result without the logarithmic factor.

We are interested in the PDF of the random variable s_M such that (cf. (69),(92))

$$s_M = \frac{1}{M} \sum_{i=1}^M w_i, \quad g_\infty(w) = \frac{1}{w^2 \sqrt{\pi \log w}}. \quad (\text{F1})$$

Here w_i are i.i.d random variables sampled from $g_\infty(w)$ and we are interested in the asymptotic limit $M \gg 1$.

Using the convolution property of a sum of statistically independent random variables we get for the PDF of s_M

$$\text{PDF}(s_M) = \frac{1}{2\pi} \int_{-\infty}^{\infty} dq [\varphi_\infty(q/M)]^M e^{-iqs_M}, \quad (\text{F2})$$

where

$$\varphi_\infty(u) = 1 + \phi_\infty(u),$$

and $\phi_\infty(u)$ is given in (E1). The limit $M \gg 1$ corresponds to $|u| \ll 1$. We note that

$$\lim_{u \rightarrow 0} \phi_\infty(u) = 0 \quad (\text{F3})$$

Taking into account that $\phi(u)$ is small in the above limit we write

$$\text{PDF}(s_M) \simeq \frac{1}{2\pi} \int_{-\infty}^{\infty} dq \exp[-iqs_M + M\phi_\infty(q/M)]. \quad (\text{F4})$$

Quantity $M\phi_\infty(q/M)$ can be expanded in inverse powers of $\log M \gg 1$ using asymptotic form of the characteristic function at small argument given in Eqs. (E13),(E14). First few terms of expansion have the form

$$\begin{aligned} M \text{Re} \phi_\infty\left(\frac{q}{M}\right) &\simeq -\frac{\pi|q|}{2\sqrt{\log M}} + \frac{\sqrt{\pi}|q|(1 - \gamma_{\text{Euler}} - \log|q|)}{4(\log M)^{3/2}}, \\ M \text{Im} \phi_\infty\left(\frac{q}{M}\right) &\simeq 2q \left(\frac{\log M}{\pi}\right)^{1/2} + q \frac{1 - \gamma_{\text{Euler}} - \log|q|}{(\pi \log M)^{1/2}} \\ &\quad + \frac{q \log|q|(1 - \gamma_{\text{Euler}})}{2\sqrt{\pi}(\log M)^{3/2}}. \end{aligned} \quad (\text{F5})$$

where γ_{Euler} is the Euler constant.

It is clear from comparing individual terms in Eq. (F5) with the exponential in the integrand in Eq.(F4) that $q = \mathcal{O}(\sqrt{\log M})$. Therefore we can drop in Eqs. (F5) terms $\mathcal{O}(1/(\log M)^{3/2})$. We make the change of variables in the integral in (F4)

$$q = 2\sqrt{\frac{\log M}{\pi}} t, \quad (\text{F6})$$

and obtain

$$\text{PDF}(s_M) = \frac{1}{\sigma_M} L_1^{1,1} \left(\frac{s_M - b_M}{\sigma_M} \right), \quad (\text{F7})$$

$$L_1^{1,1}(x) \equiv \frac{1}{2\pi} \int_{-\infty}^{\infty} dt e^{-itx - |t| - \frac{2i}{\pi} t \log|t|}. \quad (\text{F8})$$

Function $L_1^{1,1}(x)$ above is a so-called Levy alpha-stable distribution [30, 47, 48] shown in Fig. 11. The distribution is defined by its characteristic function. Parameters b_M and σ_M in (F7) are typical values that characterize the shift of the maximum of the $\text{PDF}(s_M)$ from the origin and its overall scale, respectively. They are given in Eqs. (98) and (97) of the main text and we also provide them for convenience below

$$\sigma_M = \frac{\pi}{2} \frac{1}{(\pi \log M)^{1/2}}, \quad (\text{F9})$$

$$b_M \simeq \sigma_M^{-1} - \frac{2}{\pi} \sigma_M \log(\sigma_M^{-1}) + \frac{2}{\pi} (1 - \gamma_{\text{Euler}}) \sigma_M, \quad (\text{F10})$$

where γ_{Euler} is the Euler constant.

It is instructive to compare the above expressions with the result for the sum of random variables that obey a standard Pareto distribution (i.e., without the logarithmic factor present in $g_\infty(w)$)

$$s_M^0 = \frac{1}{M} \sum_{i=1}^M w_i, \quad w_i \sim g_0(w) = w^{-2}. \quad (\text{F11})$$

The PDF of s_M^0 has the same form as the PDF of s_M given in (F7) but the expressions for the shift b_M^0 and the overall scale σ_M^0 are different

$$\sigma_M^0 = \frac{\pi}{2}, \quad b_M^0 = \log M + 1 - \gamma_{\text{Euler}} + \log\left(\frac{\pi}{2}\right) \quad (\text{F12})$$

One can see that

$$\frac{\sigma_M^0}{\sigma_M} \sim \frac{b_M^0}{b_M} \sim (\log M)^{1/2} \gg 1. \quad (\text{F13})$$

The rescaling factor $(\log M)^{1/2}$ between the PDFs of s_M and s_M^0 can be explained by a similar logarithmic factor in the ratio $g_0(w)/g_\infty(w) \sim (\log w)^{1/2}$, taking into account the fact that typical of $w \sim M$.

Appendix G: Justification of replacing sum with integral in Eq. (82).

We note that the number of marked states Ω_d in a miniband (100) on a Hamming distance d from a given marked state $|z_j\rangle$ decreases rapidly when d . There is a typical minimum Hamming distance $d \simeq d_{\min}^{\text{res}}$ such that

$$d_{\min}^{\text{res}} = \text{argmin}(\Omega_d) = \mathcal{O}(1). \quad (\text{G1})$$

There will be no states in the miniband located at the Hamming distances d from the state $|z_j\rangle$ that lie inside the intervals $d \in [1, d_{\min}^{\text{res}}) \cup (n - d_{\min}^{\text{res}}, n]$. For those values of d we have $\Gamma_j^{(d)} = 0$. Using (D22) we get

$$d_{\min}^{\text{res}} \simeq \frac{n}{2} - \sqrt{\frac{n}{2} \log \frac{2A\Omega}{\pi n^2}}. \quad (\text{G2})$$

where $A = A(E^{(0)}, 1/2)$ (42).

On the one hand we assume throughout the paper that the number of marked states in a miniband $\Omega \gg 1$ is sufficiently large so that the number $n - 2d_{\min}^{\text{res}}$ of dominant terms in the sum (80) is much bigger than 1. For example, using the scaling ansatz (70) we have $\Omega \sim M^{2-\gamma}$ (102). Then assuming that $\gamma < 2$ and $1 > \frac{1}{n} \log_2 M = \mathcal{O}(n^0)$ we can see that the second term in the r.h.s of (G2) is of the order of n and therefore the number $n - 2d_{\min}^{\text{res}} = \mathcal{O}(n)$.

On the other hand we note that the number Ω_d (100) of marked states in a miniband on a Hamming distance d from a given marked state $|z_j\rangle$ is large ($M_j^{(d)} > \Omega_d \gg 1$) for almost all d , aside from $\mathcal{O}(n^0)$ values of d near the boundaries of the interval $d \in [d_{\min}^{\text{res}}, n - d_{\min}^{\text{res}}]$.

We recall that all terms in a sum (80) are nearly equal to each other and therefore the relative contributions to Γ_j from the boundary terms is $\mathcal{O}(1/n)$ and can be neglected in a leading order estimates of the typical quantities. For d away from the interval boundaries the function $\delta_\eta(\epsilon_j - \epsilon_m)$ in Eq. (82) changes little between the adjacent values of ϵ_m (by an amount $\sim 1/\Omega_d \gg 1$). This provides the justification for us to replace the sum over m in (82) by an integral.

Appendix H: PDF of the random variable $h = \frac{\eta}{(z-\epsilon)^2 + \eta^2}$

Consider the PDF $p_\eta(h; z)$ introduced in the Eq. (106)

$$p_\eta(h; z) = \int_{-\infty}^{\infty} \frac{1}{W} p_A(\epsilon/W) \delta[h - \delta(z - \epsilon, \eta)] d\epsilon, \quad (\text{H1})$$

Here the function of two arguments $\delta(x, y)$ is defined in (79) and $\delta[x]$ is Dirac delta-function denoted here with bold font to distinguish from the above function. We also used the relation (46) for the PDF of marked state energies. Solving equation

$$h = \frac{\eta}{(z - \epsilon)^2 + \eta^2}, \quad (\text{H2})$$

for ϵ we get

$$\epsilon_{\pm} = z \pm \sqrt{\eta(h^{-1} - \eta)} \quad (\text{H3})$$

From here and from (H1) we get

$$p_\eta(h; z) = \frac{\sqrt{\eta}}{2h^{3/2}\sqrt{1-\eta h}} (\varphi_+(h; z) + \varphi_-(h; z)) \quad (\text{H4})$$

$$\varphi_{\pm}(h; z) = W^{-1} p_A(z \pm \sqrt{\eta(1/h - \eta)}) \quad (\text{H5})$$

For $|z| \ll W$ we get $p_\eta(h; \eta) \simeq p_\eta(h; 0)$

$$p_\eta(h; 0) = \frac{\sqrt{\eta}}{h^{3/2}\sqrt{1-\eta h}} p_A(\sqrt{\eta(1/h - \eta)}). \quad (\text{H6})$$

a. Uniform Distribution For the case of uniform distribution

$$p_A(\epsilon) = \frac{1}{W} \theta(W/2 - \epsilon), \quad (\text{H7})$$

where $\theta(x)$ is Heaviside theta-function we have

$$p_\eta(h; 0) = \frac{1}{h^{3/2}\sqrt{\eta^{-1} - h}}. \quad (\text{H8})$$

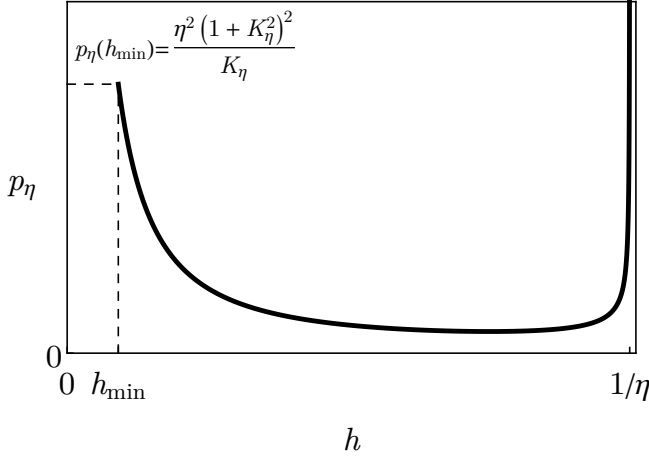


Figure 20. Plot of the PDF of $p_\eta(h; 0) \equiv p_\eta(h)$ given in (H6).

Domain of values of h is $h \in [h_{\min}, h_{\max}]$ where

$$h_{\min} = \frac{1}{\eta(1 + K_\eta^2)}, \quad h_{\max} = \frac{1}{\eta}. \quad (\text{H9})$$

$$K_\eta \equiv \frac{W}{2\eta}. \quad (\text{H10})$$

And the value of the PDF on the lower boundary is

$$p_\eta(h_{\min}) = \eta^2 \frac{(1 + K_\eta^2)^2}{K_\eta}. \quad (\text{H11})$$

In the case of delocalized non-ergodic states (103)

$$M \gg K_\eta \gg 1. \quad (\text{H12})$$

The PDF $p_\eta(h; 0) \equiv p_\eta(h)$ is plotted in Fig. 20. The PDF reaches the local maximum on the lower boundary h_{\min} corresponding to values of marked state energies $\epsilon \simeq W$ located at the edges of the IB. In the region $h \sim 1/\eta$ the probability density reaches very small values, $p_\eta(h, z) \sim \eta^2$, corresponding to the energies of marked states $|\epsilon - z| \simeq \eta$. Maximum value of $h = 1/\eta$ corresponds to exact resonance $\epsilon = z$. The PDF $p_\eta(h; 0)$ has an integrable singularity at this point.

It is of interest to consider the PDF of the sum of random variables h_m over all marked states

$$s_M^h = \frac{1}{M} \sum_{m=1}^M h_m, \quad h_m = \frac{\eta}{(z - \epsilon_m)^2 + \eta^2}. \quad (\text{H13})$$

In the non ergodic phase $W \gg \eta$ mean value of h_m is much smaller than its standard deviation

$$\langle h_m \rangle = \frac{\sum_{\sigma=\pm 1} \text{arccot} \left(\frac{2\eta}{W - 2\sigma z} \right)}{W} \simeq \frac{\pi}{W}, \quad (\text{H14})$$

$$\langle h_m^2 \rangle \simeq \frac{\pi}{2W\eta} \gg \langle h_m \rangle^2. \quad (\text{H15})$$

Note that the mean is dominated by small marked state energies $\epsilon_m \sim \eta$ while standard deviation is dominated by $\epsilon_m \sim W$.

However for sufficiently large M the mean value of the sum $\sum_{m=1}^M h_m$ is much greater than its standard deviation provided that $\delta\epsilon \ll \eta$

$$\frac{\langle s_M^h \rangle^2 - \langle s_M^h \rangle^2}{\langle s_M^h \rangle^2} \simeq \frac{1}{2\pi} \frac{\delta\epsilon}{\eta} \ll 1 \quad (\text{H16})$$

Therefore in the delocalized phase

$$\eta \gg \delta\epsilon = \frac{W}{M}, \quad (\text{H17})$$

the sum $\sum_{m=1}^M h_m$ is self-averaging.

It is convenient to introduce rescaled variables

$$y_m = \sqrt{h_m \eta}. \quad (\text{H18})$$

Their PDF has the form

$$\mathfrak{p}_\eta(y) = \frac{1}{K_\eta y^2 \sqrt{1 - y^2}}. \quad (\text{H19})$$

Boundaries of the domain of $p_\eta(y)$ are

$$y_{\min} = \frac{1}{\sqrt{1 + K_\eta^2}} \leq y < y_{\max} = 1. \quad (\text{H20})$$

Appendix I: PDF of the imaginary part of self-energy in self-consistent Born approximation

In this section we provide details of calculations of self-consistent Born approximation presented in Sec. VIII A 2 of the main text. We study the PDF of the sum

$$\Sigma'' = V_{\text{typ}}^2 \sum_{m=1}^M \frac{w_m \eta}{(z - \epsilon_m)^2 + \eta^2}, \quad (\text{I1})$$

where $w_m = \mathcal{V}^2(d_{0m})/V_{\text{typ}}^2$ (see Eqs. (D7), (D8)) are random variables sampled from the distribution $g_\infty(w)$ (69) and marked state energies ϵ_m obey the distribution $p_A(\epsilon/W)/W$ (46). The sum in (I1) can be written in the form

$$\Sigma'' = \frac{V_{\text{typ}}^2}{\eta} \sum_{m=1}^M x_m, \quad x_m = w_m y_m^2, \quad (\text{I2})$$

where y_m are random variables (H18) sampled from the distribution $\mathfrak{p}_\eta(y)$ (H19). For $|z| \ll W$ random variables

x_m obey the PDF $g_\eta(x)$ such that

$$g_\eta(x) = \int_{y_{\min}}^1 dy \int_1^\infty dw \mathbf{p}_\eta(y) g_\infty(w) \delta(x - wy^2). \quad (\text{I3})$$

Using (H19) and (H20) one can show that (cf. also (I7))

$$\lim_{\eta \rightarrow \infty} g_\eta(x) = g_\infty(x). \quad (\text{I4})$$

In order to calculate the PDF of the sum Σ'' (I1) in the limit $M \rightarrow \infty$ we use GCLT following the same approach as that in Sec. F. The PDF of the random variable Σ'' equals

$$\text{PDF}(\Sigma'') \simeq \frac{1}{2\pi} \int_{-\infty}^\infty dk e^{-ik\Sigma'' + M\phi_\eta(kV_{\text{typ}}^2/\eta)}, \quad (\text{I5})$$

where $\phi_\eta(u)$ is the characteristic function of the PDF $g_\eta(x)$ (I7)

$$\phi_\eta(u) = \int_{\frac{1}{1+K_\eta^2}}^\infty dx g_\eta(x) (e^{iux} - 1). \quad (\text{I6})$$

1. PDF of individual terms in the sum

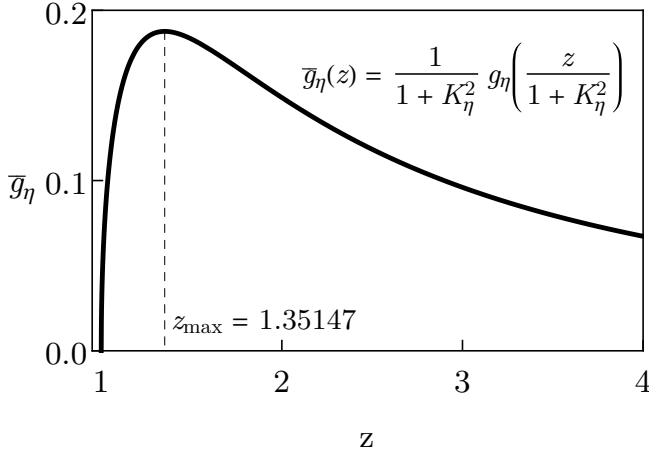


Figure 21. Plot of $\bar{g}_\eta(z)$ given in (I8) for $K_\eta = \sqrt{30}$.

After some transformations we get from Eq. (I3)

$$g_\eta(x) = \frac{1}{x^2 K_\eta \sqrt{2\pi}} \times \int_{\frac{1}{\sqrt{1+K_\eta^2}}}^{\min(1, \sqrt{x})} \frac{dy}{\sqrt{(1-y^2)(\log x^{1/2} - \log y)}}. \quad (\text{I7})$$

The PDF is plotted in Fig. 12. Its maximum lies very close to the left boundary of its domain $x \in [1/(1+K_\eta^2), \infty)$. For $x \ll 1$ the PDF $g_\eta(x)$ depends on x in terms of the rescaled parameter $z = x(1+K_\eta^2)$ whose

PDF is

$$\bar{g}_\eta(z) \simeq \frac{\text{erf}\left(\sqrt{\frac{1}{2} \log z}\right)}{z^{3/2} \sqrt{2}}. \quad (\text{I8})$$

The plot of $\bar{g}_\eta(z)$ is given in Fig. 21), its maximum $z_{\max} \simeq 1.35$. Typical values of $x_m \simeq z_{\max}/K_\eta^2 \ll 1$ correspond to $w_m \sim 1$ and to a broad PDF of marked state energies, $|z - \epsilon_m| \sim W$.

We are interested in the limits (cf. (H12))

$$x \gg 1, \quad K_\eta \gg 1. \quad (\text{I9})$$

We note that $\log x \gg |\log y|$ in the denominator of (I7) for all y except for the small interval

$$\frac{1}{\sqrt{1+K_\eta^2}} \leq y \lesssim \frac{1}{x},$$

whose contribution to the integral neglected. Expanding the integrand in powers of $(\log x)^{-1/2}$ we get

$$g_\eta(x) \simeq \frac{\pi}{2K_\eta} g_\infty(x) - \frac{\pi \log 2}{2K_\eta \pi^{1/2} x^2 \log^{\frac{3}{2}} x}, \quad (\text{I10})$$

where function $g_\infty(x)$ is defined in (69). We observe from (H10), (H14) that $\eta \langle h_m \rangle = \frac{\pi}{2K_\eta}$. Using the expressions for g_∞ (69) and $\langle h \rangle$ (H14) we obtain under the condition (I9)

$$g_\eta(x) \simeq \eta \langle h \rangle g_\infty\left(\frac{x}{\eta \langle h \rangle}\right), \quad x \gg 1. \quad (\text{I11})$$

Given a large deviation of x_m satisfying (I9), the conditional PDF of ηh_m is narrowly peaked around its mean value corresponding to $|\epsilon_m - z| \sim \eta$. In contrast, typical values of x_m correspond to a much broader PDF of $\epsilon_m \sim W$. This gives rise to a small factor $\pi/2K_\eta \sim \eta/W$ in the leading order term in (I10).

2. Characteristic function of the PDF of the elements in the sum

The relation between the characteristic functions $\phi_\eta(u)$ and $\phi_\infty(u)$ (E1) in the limit

$$|u| \ll 1, \quad (\text{I12})$$

should be the same as the relation (I10) between the corresponding PDFs $g_\eta(x)$ and $g_\infty(x)$ in the limit of large x (I9). Here we will establish this directly. We break $\phi_\eta(u)$ in two parts

$$\phi_\eta(u) = \phi_\eta^1(u) + \phi_\eta^2(u), \quad (\text{I13})$$

where

$$\phi_\eta^1(u) = \int_{\frac{1}{1+K_\eta^2}}^1 dw g_\eta(w) (e^{i u w} - 1) , \quad (\text{I14})$$

$$\phi_\eta^2(u) = \int_1^\infty dw g_\eta(w) (e^{i u w} - 1) . \quad (\text{I15})$$

Expanding $\phi_\eta^1(u)$ in u we get

$$\phi_\eta^1(u) \simeq \frac{\pi}{2K_\eta} i \zeta_1 u , \quad (\text{I16})$$

where

$$\zeta_1 = \frac{2}{\pi^{3/2}} \int_0^1 \frac{dx}{x} \int_0^{\sqrt{x}} dy \frac{1}{\sqrt{(1-y^2) \log(x/y^2)}} . \quad (\text{I17})$$

To calculate $\phi_\eta^2(u)$ in the limit of small $|u|$ we introduce $X \gg 1$ such that

$$|u| \ll X|u| \ll 1 , \quad (\text{I18})$$

and write

$$\phi_\eta^2(u) = \phi_\eta^{2,-}(u) + \phi_\eta^{2,+}(u) . \quad (\text{I19})$$

Here

$$\phi_\eta^{2,-}(u) = \int_1^X dx g_\eta(x) (e^{i u x} - 1) , \quad (\text{I20})$$

$$\phi_\eta^{2,+}(u) = \int_X^\infty dx g_\eta(x) (e^{i u x} - 1) . \quad (\text{I21})$$

We use (I18) and expand $\phi_\eta^{2,-}(u)$ in u

$$\phi_\eta^{2,-}(u) \simeq i u \int_1^X g_\eta(x) dx . \quad (\text{I22})$$

To calculate the term $\phi_\eta^{2,+}(u)$ we use the approximation (I10) and write

$$\phi_\eta^{2,+}(u) = \frac{\pi}{2K_\eta} \phi_\infty(u) - i u \frac{\pi}{2K_\eta} \int_1^X g_\infty(x) x dx . \quad (\text{I23})$$

$$- \frac{\pi \log 2}{2K_\eta} \int_X^\infty dx \frac{e^{i u x} - 1}{\sqrt{\pi x^2 (\log x)^{3/2}}} \quad (\text{I24})$$

where the characteristic function ϕ_∞ is defined in (E1).

Combining $\phi_\eta^{2,\pm}(u)$ together and taking the limit $X \rightarrow \infty$ we get after some transformations

$$\phi_\eta^2(u) \simeq \frac{\pi}{2K_\eta} (\phi_\infty(u) - i \zeta_2 u) \quad (\text{I25})$$

$$\zeta_2 = \left(\frac{32}{\pi^3} \right)^{1/2} \int_0^1 dy \left(\frac{\log(1/y)}{1-y^2} \right)^{1/2} .$$

After some transformations one can show that $\zeta_1 = \zeta_2$. Therefore terms $\sim u$ in $\phi_\eta^1(u)$ and $\phi_\eta^2(u)$ cancel each other. Combining these two quantities together in (I13) we finally get

$$\phi_\eta(u) \simeq \frac{\pi}{2K_\eta} \phi_\infty(u) + \mathcal{O} \left(\frac{|u|}{K_\eta |\log u|^{3/2}} \right) . \quad (\text{I26})$$

As expected, this relation corresponds to the relation (I10) between the PDFs g_k and g_∞ .

3. GCLT for the sum

We now revisit the expression (I5) for the PDF of the variable Σ'' (I1). In the limit $M \rightarrow \infty$ the integral over k in the r.h.s of (I5) is dominated by small values of the argument in $\phi_\eta(k V_{\text{typ}}^2 / \eta)$. Then using (I26) and (H10) we get after the change of a variable of integration in (I5)

$$\text{PDF}(\Sigma'') = \frac{1}{2\pi \Sigma''_*} \int_{-\infty}^{\infty} dq e^{-i q \frac{\Sigma''}{\Sigma''_*} + \Omega_\eta \phi_\infty(q / \Omega_\eta)} , \quad (\text{I27})$$

where Σ''_* (95) is the characteristic value of imaginary part of self-energy of marked states obtained in FGR-based calculation in Sec. VI and quantity Ω_η equals

$$\Omega_\eta = \frac{\pi M}{2K_\eta} = \frac{\pi \eta}{\delta \epsilon} . \quad (\text{I28})$$

It has a meaning of the typical number of marked states within the non-ergodic miniband of the width η (cf. Eq. (100) and Fig. 10).

We make a self-consistent assumption (cf. Eq. (134) in the main text) and set

$$\eta = \Sigma''_* . \quad (\text{I29})$$

Then, one can immediately see that

$$\Omega_\eta = \Omega_{\Sigma''_*} = \Omega , \quad (\text{I30})$$

where Ω is the typical number of marked states in a miniband defined in (115).

Comparing the expression (I27) with (F4) and (I30) we represent the random variable Σ'' in the form

$$\Sigma'' \stackrel{d}{=} \sigma_\Omega \Sigma''_* x + b_\Omega \Sigma''_* , \quad \text{PDF}(x) = L_1^{1,1}(x) . \quad (\text{I31})$$

Here random variable x obeys a Levy alpha-stable distribution (F8) shown in Fig. 11. The quantities b_Ω , σ_Ω are given below

$$\sigma_\Omega = \sqrt{\frac{\pi}{4 \log \Omega}} , \quad (\text{I32})$$

$$b_\Omega \simeq \sigma_\Omega^{-1} - \frac{2}{\pi} \sigma_\Omega \log(\sigma_\Omega^{-1}) + \frac{2}{\pi} (1 - \gamma_{\text{Euler}}) \sigma_\Omega , \quad (\text{I33})$$

Their dependence on Ω is given in the main text,

Eqs. (98),(97), where we should replace M with Ω .

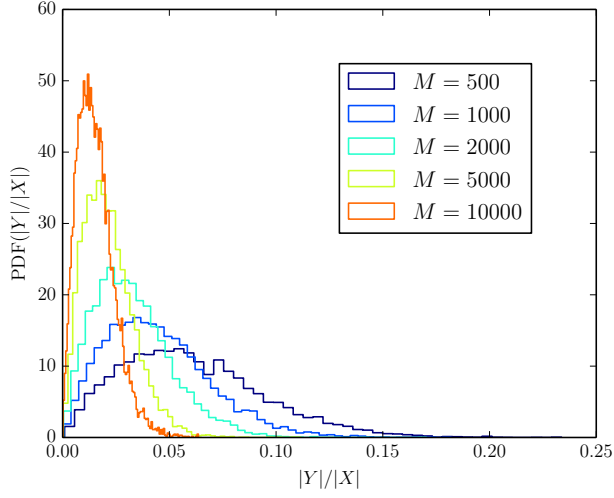


Figure 22. Probability distribution of the ratio $|Y/X|$ defined in Eqs. (J1),(J2) for $\gamma = 0.6$.

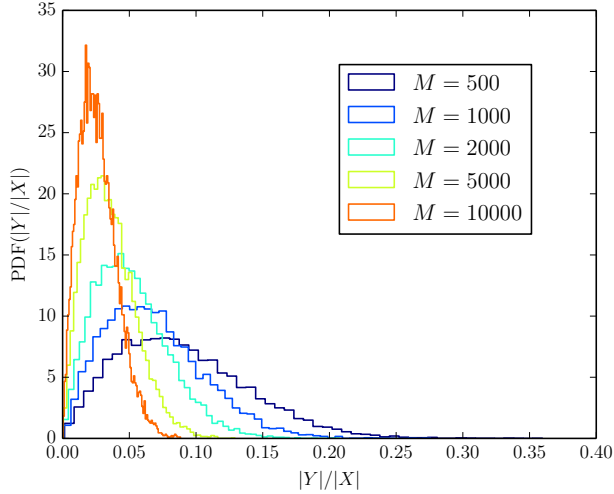


Figure 23. The same as in Fig. 22 but with $\gamma = 1.2$.

Appendix J: Numerical simulations

In this Section we provide details of the numerical analysis of the ensemble of Hamiltonians introduced in Sec. V in addition to the results in Sec. XI.

1. Numerical justification of cavity equations

Application of cavity method to the case of the ensemble of dense matrices considered in this paper, see

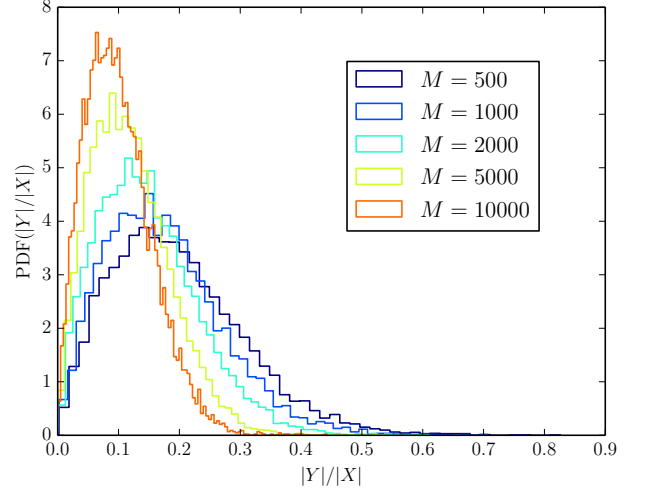


Figure 24. The same as in Fig. 22 but for $\gamma = 1.6$.

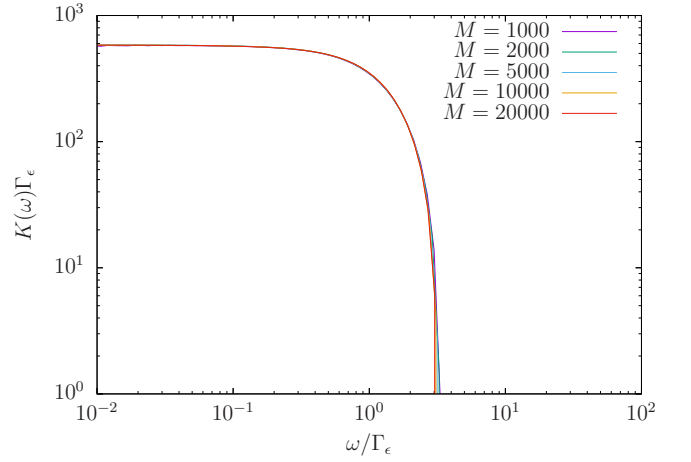


Figure 25. $K(\omega)$ rescaled with the characteristic energy $\Gamma_\epsilon = 2\Sigma''_{\text{typ}}M^\epsilon$ where the typical mini-band width is given by Eq. (130). Here $\gamma = 1$ with fitting exponent $\epsilon = -0.025$.

Sec. V, exploits the similarity between the local structure of the adjacency graph of the Hamiltonian \mathcal{H} and the Bethe lattice. The derivation of the cavity equations (104a),(104b) for the case of \mathcal{H} outlined in Sec. VII neglects off diagonal terms Y in comparison to diagonal X , which is justified for graphs with extensive number of neighbors [30], where,

$$X = \frac{1}{M} \sum_j \mathcal{H}_{1j}^2 G_{jj}(z), \quad (\text{J1})$$

$$Y = \frac{2}{M} \sum_{j \neq k} \mathcal{H}_{1j} \mathcal{H}_{1k} G_{jk}(z), \quad (\text{J2})$$

where G_{ij} is the single particle Green function corresponding to the Hamiltonian \mathcal{H} at energy near the center of the band, introduced in Sec. VII. It has been shown

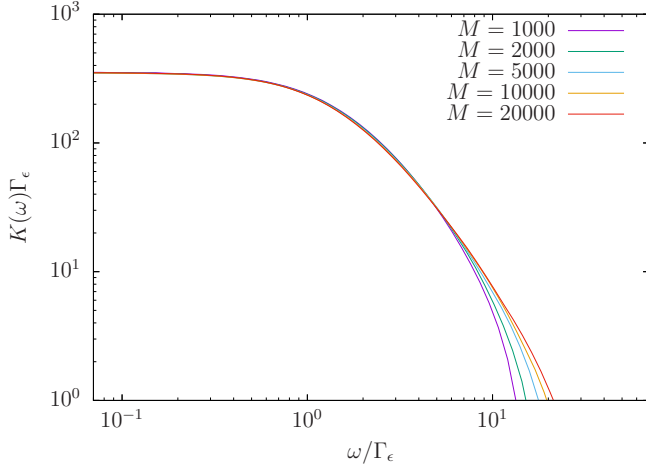


Figure 26. The same as in Fig. 25 but with $\gamma = 1.4$ and fitting exponent $\varepsilon = 0.04$.

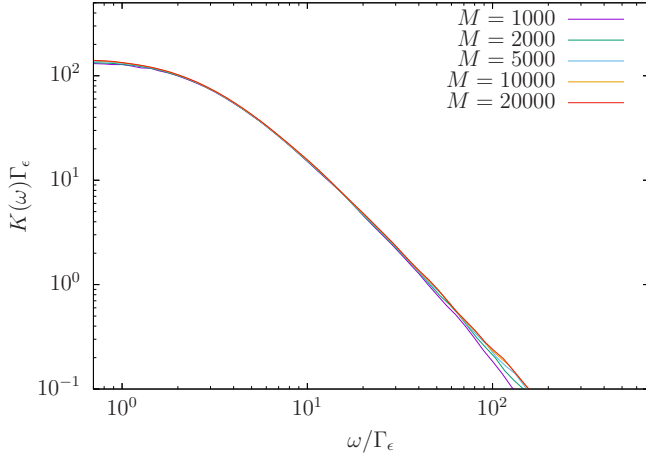


Figure 27. The same as in Fig. 25 but with $\gamma = 1.8$ and fitting exponent $\varepsilon = -0.05$.

for Levy matrices [30] that the ratio $|Y/X|$ scales to zero with growing matrix size M and therefore can be neglected. This argument could be extended to PBLMs considered in this paper. We confirm the validity of this approximation numerically by analyzing the probability distribution of the ratio $|Y/X|$ as a function of the matrix size M . In Figs. 22,23, 24 the distribution of $|Y/X|$ scales towards high weight at vanishing values of $|Y/X|$ with growing M .

2. Numerical analysis of population transfer time

a. Population transfer time from the dynamical correlator

In addition to Fig. 16 in Sec. XI of the main text, we perform a similar collapse of the dynamical correlator frequency dependence for different matrix sizes M for a range of different values of γ . In Figs. 25-28 the charac-

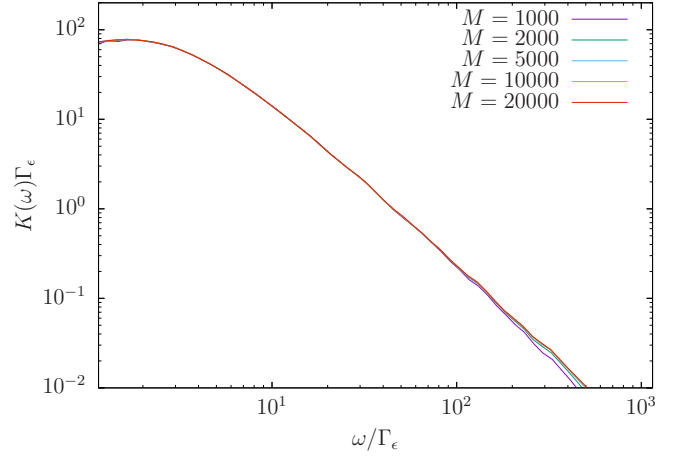


Figure 28. The same as in Fig. 25 but with $\gamma = 2$ and fitting exponent $\varepsilon = -0.055$.

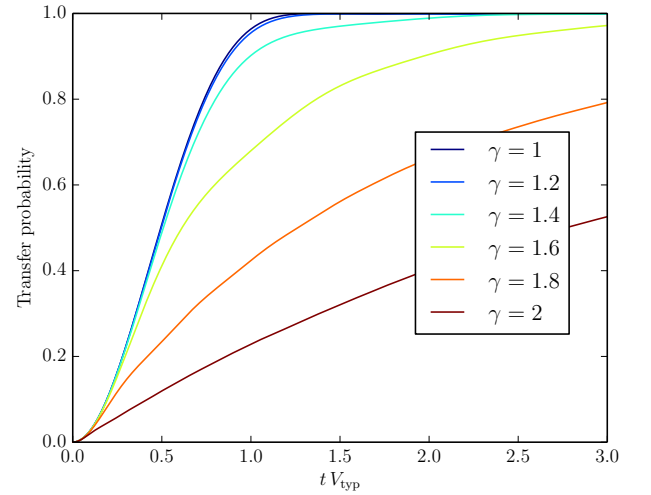


Figure 29. Population transfer probability as a function of time t in units of $1/V_{\text{typ}}$ for various values of parameter $\gamma = 2\alpha$.

teristic energy scale extracted from each set of plots using this procedure $\Gamma_\varepsilon = \Gamma_{\text{typ}} M^\varepsilon$ corresponds to the typical mini-band width with the respective value of the parameter γ . The fitting parameter in the scaling exponent ε is small for all γ we considered and is consistent with finite size effect.

b. Population transfer probability as a function of time

In the main text we analyzed the complexity of the PT protocol using the solution of the full non-linear cavity equations for the size of the typical mini-band and estimated the number of states in the mini-band using the classical value of the level spacing W/M . In this section we analyze the scaling of the population transfer time

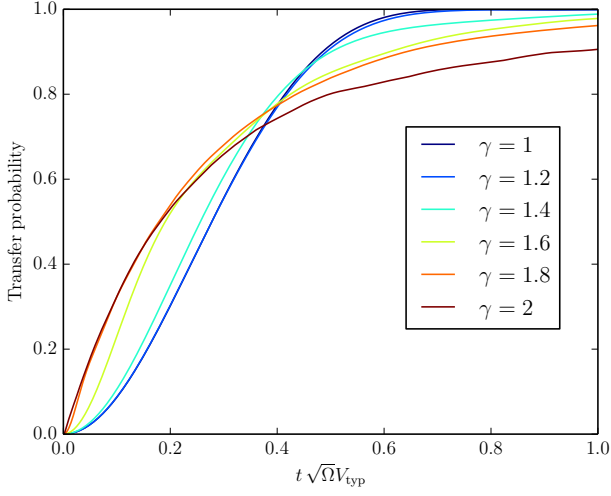


Figure 30. Population transfer probability as a function of time rescaled with the effective mini-band width $\sqrt{\Omega}$ where the number of states in the mini-band is estimated using Fermi's golden rule $\Omega = M^{2-\gamma}$, see Eq. (102) of the main text.

using exact numerical time evolution. We contrast the

population transfer time obtained from the characteristic energy scale of the frequency dependence of the dynamical correlator in Figs. 25-28 with the time dependence of the transfer probability,

$$p(t) = |\langle i | \psi(t) \rangle|^2, \quad (\text{J3})$$

where $|i\rangle$ is the initial bitstring and $|\psi(t)\rangle$ is the wave function resulting from the evolution with the impurity band Hamiltonian in transverse field \mathcal{H} , see Sec. V, for a time t , which is the quantity directly observed experimentally. Note that in Fig. 29 the time scale at which the transfer probability becomes of order one depends strongly on the parameter γ , reflecting the fact that the characteristic time is determined by the size of the many-body mini-band Γ rather than the typical off-diagonal matrix element V_{typ} . To verify this we rescaled the unit of time with the square root of the number of states in the mini-band $\sqrt{\Omega}$, a good approximation for the scaling of the mini-band, see Sec. VI for qualitative discussion and Sec. VIII for rigorous results. We observe approximate collapse of the curves for different values of γ corroborating the PT runtime scaling presented in the main text as well as the estimate of the number of states in the mini-band.